NATIONAL INSTITUTE FOR HIGHER EDUCATION, DUBLIN

School of Electronic Engineering.
Control Technology Research Unit.

Thesis Submitted for the Degree of
Master of Engineering.

Design of a Brushless A.C. Servo-motor using Neodymium Iron Boron Permanent Magnet Material.

by:

Ciaran P. Allen B.E.

for:

Dr. Frank Devitt.

September 1988.

I declare that the research herein was completed
by the undersigned.

Signed. Ciaran P. Allen Date. 11/9/88

Contents.

Acknowledgements.

I would like to thank Dr. Frank Devitt, my supervisor for his technical support while I was conducting this research. I would also like to thank the staff of Moog Ltd, especially Mr. Tony McEnroe for help in completing this project. Thanks also to the members of The Control Technology Research Unit at N.I.H.E. Dublin and to the staff of the School of Electronics Engineering. A special word of thanks to my wife Fidelma for her patience and understanding while I was working on this research.

ABSTRACT.

Design of a Brushless A.C. Servo-motor using Neodymium Iron Boron Permanent Magnet Material.

AUTHOR: Ciaran P. Allen.

The excellent performance characteristics of Brushless Servo-motors have led to their widespread use in areas such as Robotics, CNC Machines and in the Aero-space Industry. The development of Neodymium Iron Boron permanent magnet material with the highest available Energy Product levels promised improved motor performance coupled with reduced magnet costs. However this material exhibits large changes in magnetic properties with temperature when compared with Samarium Cobalt magnets, the permanent magnet material commonly used in these applications. This research examines the feasibility of substituting Samarium Cobalt magnets with Neodymium magnets in a redesigned Servo-motor.

Equations are developed which predict the motor performance based on design input data, machine physical dimensions and magnetic properties of the permanent magnet material. A winding analysis program is developed and is used to investigate the consequences of different winding configurations. The validity of this analysis is examined experimentally. Motor heating tests are performed to determine the maximum in-service magnet temperatures and these results are presented. Design studies are conducted and a prototype motor using Neodymium magnets was built and tested. The design predictions and the test results are used to determine the suitability of Neodymium Iron Boron material for high performance Servo-motor applications.

Chapter 1.

INTRODUCTION TO BRUSHLESS SERVO-MOTORS.

1.1 INTRODUCTION.

1.1.1 Permanent magnet brushless servo-motors.

In recent years, with the advent of relatively cheap power electronic components plus the demand for increased reliability, power and power to weight ratio, Permanent Magnet (P.M.) brushless motors have been employed in increasing numbers in servo-motor applications. The brushless configuration offers some distinct advantages over the traditional brush D.C. motors including higher continuous power output, higher peak torque, higher power to weight ratio, lower inertia, reduced maintenance requirements, lack of sparking at the commutator, the possibility of higher terminal voltages and reduced heat transfer from motor to load via the drive shaft. The major disadvantage of the brushless configuration is the requirement of a position sensor to indicate rotor angular position and increased control hardware over the brush type. However in many Industrial applications such as Robotics and Numerically Controlled Machines as well as the Aero-space and Military vehicle Industries where reliability and performance are crucial, the extra hardware costs do not prohibit the use of the brushless configuration.

Induction motors are also used in Servo-motor applications but because the rotor angular position is not indicative of rotor magnetic field position in this type of motor, field determining methods have to be used to determine the switching sequence in the Inverter thus increasing the required signal processing power of the Controller. A recent paper [Ref. 1] proposes a more economical method of flux sensing using the back emf induced in the stator windings and should help to lower the cost of Induction servo-motor packages in the future. However induction motors are inherently less efficient than synchronous motors due in part to higher rotor losses and also have lower power factors which will limit their use in areas where weight is a prime consideration.

1.1.2 Brushless motor configuration.

References [2] and [3] describes various brushless motor configurations suitable for servo-motor applications. These include both A.C. and D.C. brushless types which are distinguished by the way in which the stator currents and the rotor magnetic

field interact to produce constant motor torque. Figure (1.1) is a cross-section through a typical P.M. brushless motor. For simplicity only one pair of poles are shown, though in practice there may be a multiple number of pole pairs. In contrast to a standard D.C. motor the field magnets are located on the rotor, the armature being wound on the stator. The commutator and carbon brushes normally associated with the standard D.C. motor are therefore redundant and so a major cause of unreliability and performance limitation is eliminated. The task now is to produce a rotating magnetic field which is in synchronism with the rotor. This synchronism of rotor and stator fields is a condition for constant torque in a synchronous machine [Ref. 4] and is achieved with the aid of a position sensor. The position sensor provides feedback information with regard to the rotor angular position and this information is used to generate the correct sequence of stator currents to enable the motor produce constant torque.

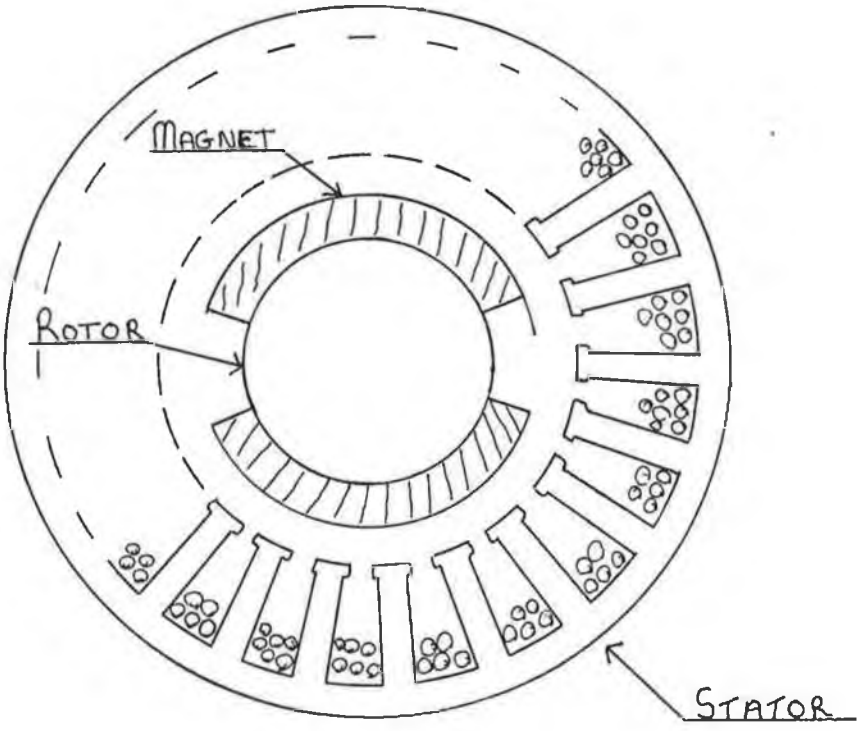

FIG. (1.1) Cross–section through a typical Brushless servo-motor.

1.1.3 Inverters and Power Supplies.

To enable a brushless motor to perform as a servo-motor requires a variable frequency, variable voltage or current source to supply the necessary stator currents to produce a rotating stator m.m.f. as required by the control algorithm. This source commonly takes the form of a voltage or current sourced inverter and associated power supply, illustrations of which are given in figures (1.2) and (1.3). The subject motor of this thesis uses a voltage source inverter which consists of the following basic parts,

(a) An uncontrolled three phase bridge rectifier
(b) A D.C. link with filtering .
(c) A controlled three phase inverter.

The major difference between the voltage supplied by a voltage source inverter and a sinusoidal voltage supply is the additional higher order voltage harmonics that are a consequence of the switching action of the inverter. These voltage harmonics tend to reduce the overall system efficiency, may cause overheating in the motor and can lead to significant harmonic torques. These effects will be dealt with in more detail at a later stage.

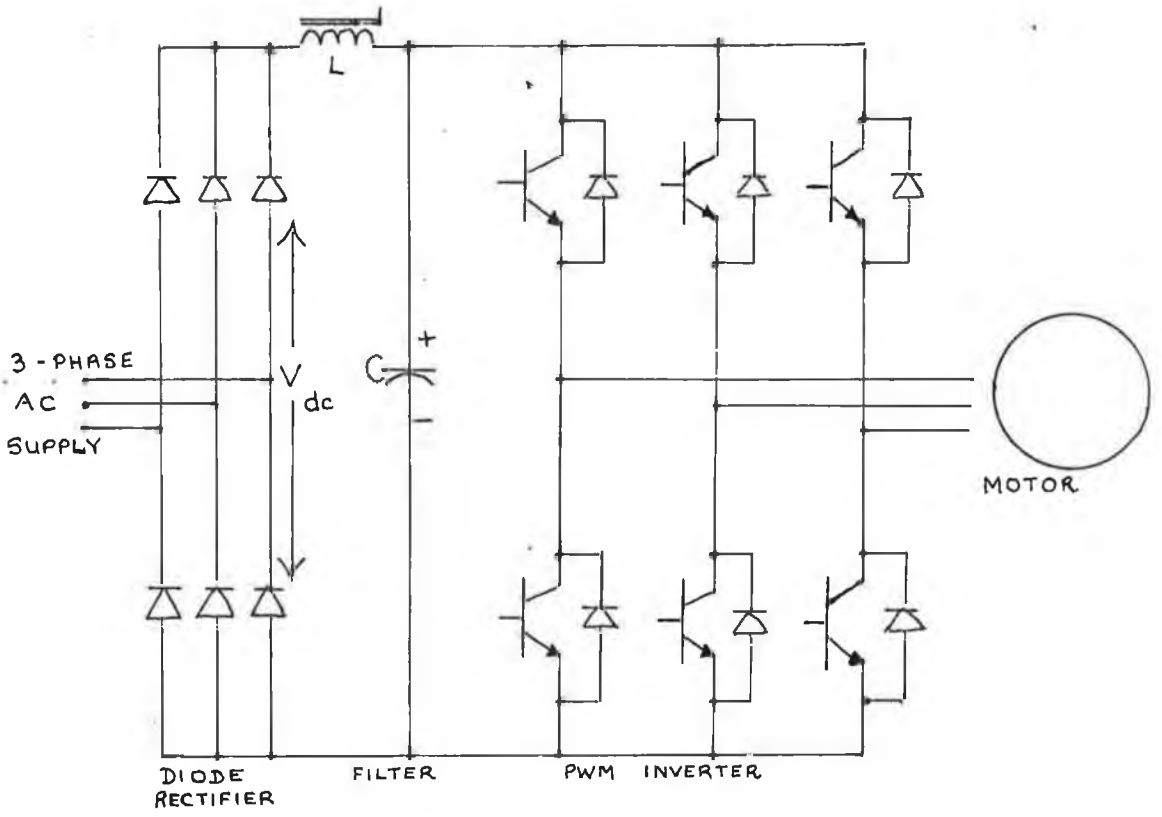

FIG. (1.2) Three Phase Voltage Source Inverter and Power Supply.

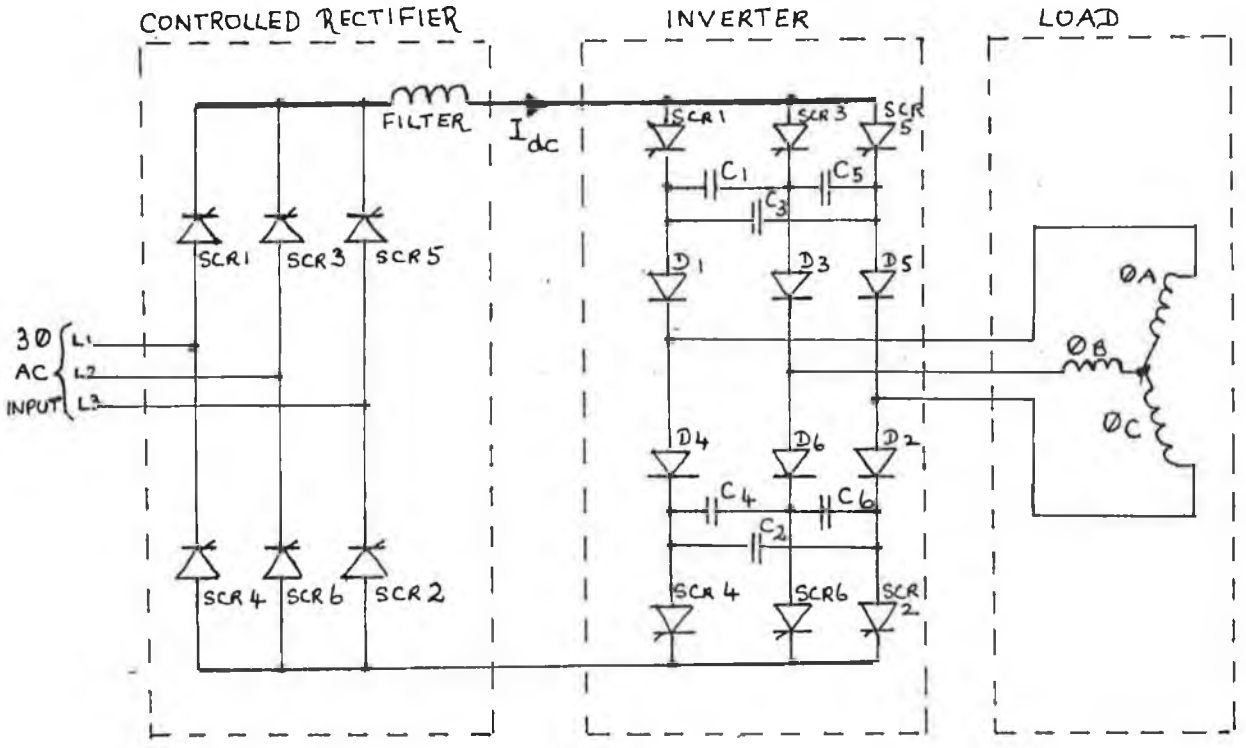

FIG. (1.3) Current Source Inverter and Power Supply.

1.2 NEODYMIUM IRON BORON MATERIAL.

As already mentioned the high power to weight ratio and reliability of brushless drive systems have been important reasons for their widespread use in critical applications. Nevertheless ways are constantly being sought to increase the power output and reduce the cost of these systems. Developments in the electronics industry in recent years have played a major role in the improvement of system reliability and reduction of system costs. On the other hand new motor developments do not appear to have happened as quickly, being dependent to a large extent on improvements in the magnetic and electrical properties of its constituent parts. One of the most important factors affecting the power output of a brushless motor is the air-gap flux produced by the rotor magnets. The use of rare earth permanent magnets such as Sa_2-Co_{17} (Samarium Cobalt) is practically universal in high performance motor drives as these materials combine the desirable properties of high magnetic induction levels coupled with the ability to withstand high demagnetising influences. These characteristics facilitate simple rotor geometries as illustrated in figure (1.1).

In 1984 considerable excitement was aroused with the announcement of Neodymium Iron Boron (Nd-Fe-B), a new permanent magnet material possessing higher induction levels than any Sa_2-Co_{17} magnet at room temperature. The material was composed of approximately 65% Iron, 30% Neodymium and 1% Boron by weight. The interest generated by this announcement can be understood by considering the following three points,

(1) Increased energy product and induction levels open up the possibility of higher power to weight ratios in motors thereby improving the performance of the overall drive system.

(2) Because of the relative abundance of Neodymium compared with Samarium and the low raw material cost of the other constituents the possibility existed for a significant reduction in the cost of high performance magnets.

(3) From a political point of view the development of a magnetic material that did not contain Cobalt was desirable since Cobalt is considered by the U.S.A. as a strategic material. This is due to the fact that Cobalt is an important constituent in the manufacture of high temperature super-alloys for aircraft and that the main supplier of Cobalt to that country is southern Africa which is a politically unstable region. In Europe a Nd-Fe-B workshop was initiated under the " Substitution and Material Technologies " subprogram of The Comission of European Communities. This workshop concentrated on the Economic and political implications of the new material as well as further improvements in the materials properties [Ref. 5].

Despite its advantages however the new material has some drawbacks as compared with Sa-Co material. These are a consequence of a relatively low Curie temperature of 312 °C as opposed to 800 °C in the case of Sa–Co. The reversible temperature coefficient of induction is much higher leading to reduced residual induction levels with increasing temperature. Similarly, the coercivity of Nd-Fe-B magnets is greatly reduced at elevated temperatures leading to the possibility of demagnetisation in some applications. Some improvement in the high temperature properties of the material have been achieved with the addition of a small amount of Cobalt but as yet the problems outlined have not been completely cured.

Some published results on the use of Nd–Fe-B in motors are available [Ref. 5] but

the steady state temperature of the magnets was of the order of 60 °C which is low as regards motor temperatures in general. This low steady state temperature was obtained by water cooling of the stator. Many of the articles outlining the use of Nd-Fe-B assumed that the temperature effects of the material would be cured but this has yet to happen.

1.3 CRITERIA FOR SERVO-MOTOR COMPARISON.

In order to make a comparison between different servo-motor designs various performance parameters need to be defined. The following list of parameters describe the performance characteristics of Brushless servo-motors. Reference [6] contains a detailed discussion of servo-motor parameters and definitions.

1.3.1 Nominal/Continuous ratings.

Maximum continuous rated current at stall I_{mc} (A).

The maximum continuous rated current I_{mc} is based on the allowable temperature rise of the motor above ambient temperature as determined by the insulation class of the motor. The insulation class to be used in this project is class F, i.e. the average temperature rise of the stator windings must not exceed 105 °C above an ambient temperature of 40 °C and the winding "hot spot" must not exceed 115 °C above ambient. The temperature rise of a motor is primarily determined by, the current flowing in the stator windings, the cross-sectional area of the stator copper conductors, the thermal conductance between the windings, the stator core, the rotor, the motor casing and the surrounding environment. Other heating effects such as high frequency current harmonics losses or iron losses also add to the temperature rise of the motor. An accurate value for I_{mc} can often only be determined experimentally although for a given range of motors an approximate value can be calculated based on the current density in the stator conductors. Since the Nd-Fe-B motor to be developed in this thesis is based on an existing range of motors the same levels of current density will be used when determining the maximum continuous rated current.

Maximum continuous torque rating at stall T_{mc} (Nm).

In the case of a brushless D.C. motor the developed motor torque is proportional to the stator current, ignoring the effects of Saturation. For a given motor design

therefore the maximum continuous torque rating of the motor at stall is determined primarily by the maximum continuous current as follows, where K_t is the torque constant of the motor,

$$\text{Max continuous torque } T_{mc} = K_t.I_{mc}$$

Nominal power output P_n (kW).

P_n is defined as the maximum continuously available output power of the motor with a winding temperature 100 °C above ambient. Moog Ltd. measure this parameter with the motor mounted on a 300 x 300 x 12 mm mild steel heat sink in free air.

Nominal Torque T_n (Nm).

T_n is the torque at which nominal power occurs.

Nominal speed N_n (s^{-1}).

N_n is the speed at which nominal power occurs.

1.3.2 Performance Characteristics.

Peak current I_p (A).

The peak current I_p is defined such that with the motor operating at a temperature of 100 °C, the application of a current pulse of magnitude I_p for one second will not cause the motor temperature to exceed the maximum temperature limit. This heating process takes place primarily in the stator windings and may be considered to be adiabatic since the time interval is very short. The following equation approximately accounts for the heating process [Ref. 1.5],

$$\frac{J^2.\ T}{\gamma} = c.(t_2 - t_1)$$

where J is the volume current density.
T is the time interval.
c is the specific heat of copper.
t_2, t_1 are the final and initial temperatures.

γ is the electrical conductivity of copper.

For example a current density of 65.8 A mm^{-2} will result in a temperature rise of the order of 30 °C in one second @ 100 °C
for copper conductors. The peak current I_p is therefore directly related to the cross-section of the stator conductors. In some cases however the peak current value may be limited by the ability of the rotor magnets to resist demagnetisation.

Peak torque T_p (Nm).

The Peak torque T_p is defined as the developed motor torque when a current equal to the peak current flows in the stator windings (assuming that the load angle is optimal).

Alternatively it may be defined as the maximum torque developed by the motor at stall for which the ratio, torque per unit stator current does not change by more than 10 %. The decrease in torque per unit current occurs due to saturation of the magnetic circuit of the motor with high stator currents.

Maximum continuous speed n_{max} (s^{-1}).

The maximum speed of the motor n_{max} corresponds to the operation of the motor in an unloaded state and with the speed limited by the motor back e.m.f. and the peak voltage output of the inverter assuming the load angle of the motor is fixed.

Maximum theoretical acceleration from stall α_{max} (rad/s^2).

The maximum theoretical acceleration from stall α_{max} is defined for an uncoupled motor as,

$$\alpha_{max} = T_p/J$$

where J is the inertia of the rotor and shaft.

Maximum power limit rate P_{lrm} (kW/s).

The maximum power limit rate P_{lrm} is the product of maximum angular acceleration and peak torque and is an index of the maximum dynamic output capacity of the servo-motor.

Torque Ripple M_r.

This is the output torque variation with rotor position at nominal output torque and witha fixed command value at the controller torque control input. This is a system parameter the value of which depends on motor and control electronics performance.

1.3.3 Motor specifications.

Voltage constant K_e (V.s/rad).

The voltage constant K_e is the open circuit terminal to terminal back e.m.f. per unit motor speed. This constant is temperature dependent since the magnetic induction of rare earth permanent magnets varies with temperature.

Torque constant K_t (Nm/A)

The torque constant K_t is the torque developed by the motor per unit current at stall. This constant also varies with temperature due to the magnetic properties of the rotor magnets and in addition can vary as a result of magnetic saturation in the motor arising from armature reaction.

Motor terminal resistance R_t (Ω).

This is the resistance measured between two motor terminals with the third terminal open circuited and with the motor disconnected from the controller.

Line to Line Inductance L (mH).

This is the self inductance of the stator winding measured between two of the motor terminals with the third terminal open circuited.

Winding electrical time constant T_m (ms).

The winding electrical time constant T_m is defined as the ratio L/R_t with L and R_t as previously defined.

Motor Constant K_m (Nm / sq root watt).

The motor constant K_m is defined as the ratio of the motor torque constant K_t to the square root of the motor terminal resistance. This parameter relates the torque

output of the motor at stall to the square root of the stator I^2R losses. The stator I^2R losses limit the maximum continuous torque at stall as a a result of winding temperature limitations. Hence this parameter is an index of the maximum continuous torque output of the motor based on thermal considerations.

1.4 BACKGROUND AND OBJECTIVE OF STUDY.

This project was carried out in association with Moog Ltd, the intention being to develop P.M. servo-motor design procedures and at the same time to investigate the possibility of using Nd-Fe-B magnets to improve servo-motor performance. Moog Ltd already had in production a range of A.C. servo-motors using Sa-Co magnets. Although a design program was available, the basis of a number of its formulae was unclear. Thus Moog Ltd were anxious to increase their knowledge and expertise in this area with particular emphasis on practically realisable designs. Because of the possibility of improved motor performance with the development of Nd-Fe-B it was decided that an investigation of the applicability of the material to servo-motors could be appropriately carried in parallel with an investigation of design procedures. It was envisaged that any Nd-Fe-B motor developed would be able to use the Controller and Power supply already in production. In the event that Nd-Fe-B magnets could not be used at the temperatures normally associated with high performance servo-motors a temperature limit on these motors was to be determined.

Dimensioned drawings of the motors tested are not included in this thesis since some of the information would be considered to be confidential by Moog Ltd. However these drawings may be obtained from the School of Electronic Engineering, N.I.H.E. Dublin with the consent of Moog Ltd.

Chapter 2.

PERMANENT MAGNET MATERIALS AND MAGNETIC CIRCUIT THEORY.

2.1 REVIEW OF PERMANENT MAGNETS AND MAGNETIC CIRCUIT THEORY.

2.1.1 Introduction

Since permanent magnets are the source of the rotor's magnetic field, a good understanding of their characteristics and behaviour in magnetic circuits is a prerequisite to undertaking any motor design. At present there are a wide variety of permanent magnet materials available many of which, from an applications viewpoint may be considered as outlined in this chapter.. However since this thesis is primarily concerned with the use of Neodymium Iron Boron (Nd Fe B) in servo motor applications the treatment will be specific to this material. For a more extensive treatment of permanent magnets and their applications reference [7] provides a good basis. The SI system of units is used throughout this thesis but since many permanent magnet manufacturers use the cgs system a conversion table is provided in appendix [A].

2.1.2 Magnetic Induction and the Magnetisation Curve.

The magnetic induction of a magnetic material $\underline{B}$ is the vector sum of two components, the magnetising field $\underline{H}$ and the intrinsic induction $\underline{B_i}$ as shown in equation (2.1).

$$\underline{B} = \underline{B_i} + \mu_0 . \underline{H} \qquad \ldots(2.1)$$

where $\underline{B}$ and $\underline{B_i}$ are measured in Tesla.
$\underline{H}$ is measured in Amps per metre.
μ_0 is the permeability of free space.

The intrinsic induction is the component of induction due to the presence of the magnetic material. In the case of a permanent magnet material it is a function of the initial magnetising field strength and of the physical properties of the material

itself. Reference [7] describes some aspects of these dependencies. Because $\underline{B_i}$ and $\underline{H}$ are vectors it is important to realise that $\underline{H}$ may have such an orientation as to be either magnetising or demagnetising with respect to $\underline{B_i}$. In Ferromagnetic materials the relationship between $\underline{B}$ and $\underline{H}$ is non-linear and this relationship is usually represented on a magnetisation curve. A typical curve is shown in figure (2.1). Usually the normal induction $\underline{B}$ is plotted against the magnetic field strength producing the major hysteris loop but occasionally the intrinsic induction is plotted also.

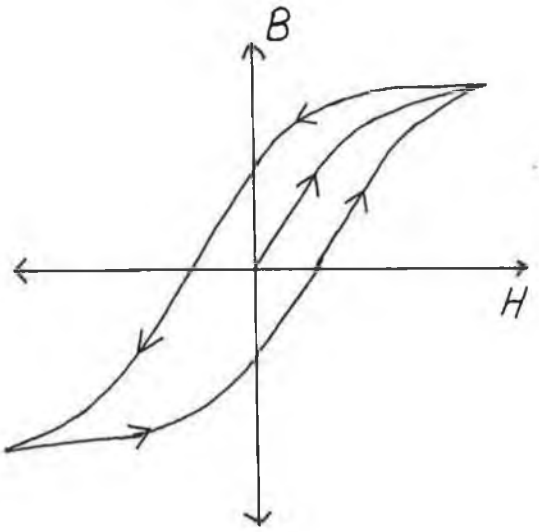

FIG. (2.1) Typical Magnetisation Curve of a Ferromagnetic Material.

When considering the use of permanent magnets in a particular application it is the second quadrant of the major hystersis loop or demagnetisation curve that needs to be considered. This is because for a permanent magnet, the field strength measured at the magnet surface has a direction opposite to that of the induction inside the magnet, i.e. with positive induction the field strength is negative. This may be appreciated better when the application of permanent magnets to magnetic circuits is considered later on. Figure (2.2) illustrates a typical demagnetisation curve for a rare earth permanent magnet such as Nd Fe B or Samarium Cobalt (Sa Co) at room temperature.

The intersection of the intrinsic induction curve and the normal induction curve with the $\underline{B}$ axis is called the residual induction B_r. The demagnetising force

required to reduce the normal induction B to zero is called the coercive force H_c and corresponds to the intersection of the normal induction curve with the H axis. The demagnetising force required to reduce the intrinsic induction to zero is termed the intrinsic coercive force H_{ci} and corresponds to the intersection of the intrinsic induction curve and the H axis and is always greater than H_c.

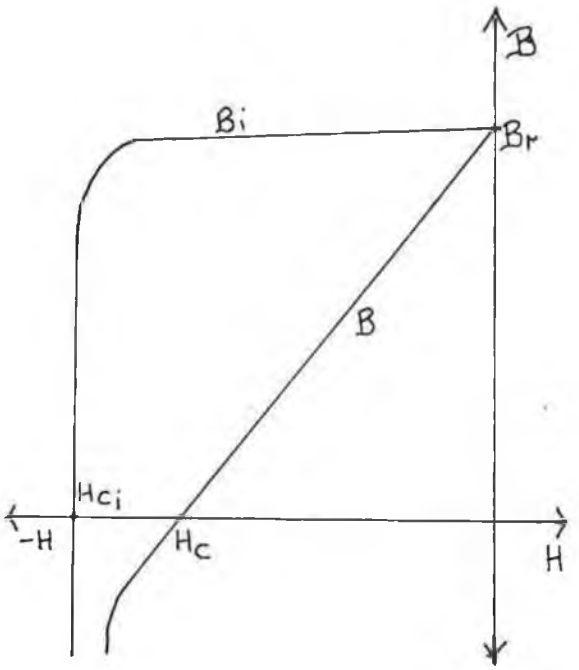

FIG. (2.2) Demagnetisation Curve of a Rare Earth Permanent Magnet.

2.1.3 Recoil Permeability.

The demagnetisation curve of a permanent magnet material is illustrated in figure (2.3) [Ref. 7]. Consider the application of a demagnetising field H_a causing the normal induction to decrease along the major hystersis loop to point A as shown. If the demagnetising field H_a is reduced, the induction will generally not retrace the major loop but instead will follow the path A – B. If H_a is again applied the induction will follow a path such as B - C. Alternatively varying the field at some intermediate strength between zero and H_a will cause the induction to trace small interior loops. These interior loops are termed minor loops and generally the area enclosed by them is small enough to allow a straight line drawn through the end points of the loop to represent the loop with little error in induction levels. The slope of this line is termed the recoil permeability μ_r of the material and is an important characteristic when considering the effects of a demagnetising field on

the induction of a permanent magnet. In this example when the applied field was reduced to zero, the induction did not return to its original value B_r and a net loss of intrinsic induction occurred due to the inelastic rotation of some of the magnetic domains in the magnet. Obviously this feature of permanent magnet behaviour needs to be taken into account by the designer when selecting a material for use in a device that will be subject to strong demagnetising fields.

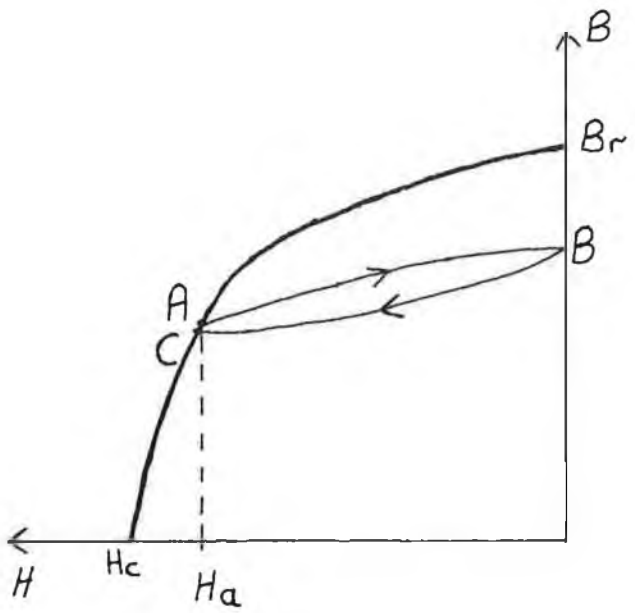

FIG. (2.3) Demagnetisation Curve of a Permanent Magnet.

2.1.4 The application of Permanent Magnets to Magnetic Circuits.

Figure (2.4) illustrates a magnetic circuit consisting of a permanent magnet, an air-gap and two iron pole pieces. The permeability of the pole pieces is considered infinite as compared to the air-gap. Applying Ampere's circuital law yields,

$$\underline{H}_m.L_m + \underline{H}_g L_g = 0 \qquad \ldots(2.3)$$

Rearranging EQN (2.3) gives,

$$\underline{H}_m = \frac{-\underline{H}_g.L_g}{L_m} \qquad \ldots(2.4)$$

From equation (2.4) it is seen that the existence of an air gap in a magnetic circuit is equivalent to the application of a negative field to the magnet. It can also be shown [Ref 7] that,

$$B_m = \frac{-K_{phi} \cdot A_g \cdot L_m \cdot H_m \cdot \mu_0}{A_m \cdot L_g} \quad \text{(tesla)} \qquad \ldots(2.5)$$

where A_g is the gap area.
A_m is the magnet area.
K_{phi} is the flux leakage factor.

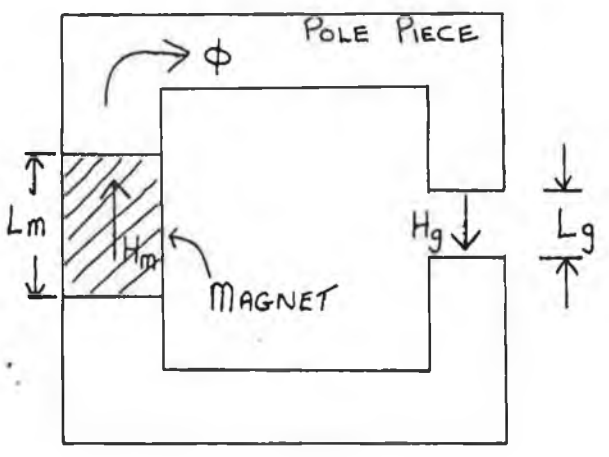

FIG. (2.4) Magnetic Circuit with an Air-Gap.

This is the equation of a straight line which intersects the demagnetisation curve of the magnet as shown in figure (2.5). The magnetic state of the permanent magnet is equal to that existing at point a with a flux density H_m existing in the magnet and $H_m.L_m$ representing the magnetomotive force required to produce the air gap field. Rearranging equation (2.5) yields,

$$\frac{B_m}{H_m} = K_{phi} \cdot \frac{L_m}{A_m} \cdot \mu_0 \cdot \frac{A_g}{L_g} = K_{phi} \cdot \frac{L_m}{A_m} \cdot P_g \qquad \ldots(2.6)$$

where P_g is the air gap permeance or $\mu_0 . A_g / L_g$.

Equation (2.6) gives the slope of the permeance line as a function of the air-gap

and magnet dimensions. It can also be shown [Refs. 4 and 7] that the volume of the magnet is given by,

$$V_m = \frac{K_{phi} \cdot V_g \cdot B_g^2}{\mu_0 \cdot B_m \cdot H_m} \qquad \ldots(2.7)$$

where V_g is the air-gap volume.

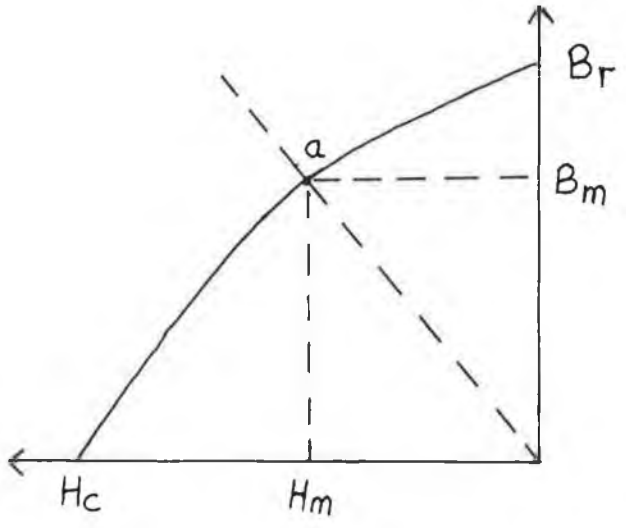

FIG. (2.5) Permanent Magnet with an Air-Gap in the Circuit.

It is evident on inspection of equation (2.7) that for a given air-gap volume and flux density, the volume of magnet required can be minimized by maximizing the $B_m H_m$ product. This product is known as the energy product of the magnet (in Joules per metre cubed) and is used as a criterion to compare different magnetic materials. It is desirable from the viewpoint of efficient material use to operate the magnetic material as near to its maximum energy point as possible. Frequently manufacturers curves have loci of constant energy product superimposed on the demagnetization curve to allow easy comparison of materials on this basis. Needless to say, the maximum energy product of a material is not the only consideration when choosing a magerial for a particular application and if the magnet is subject to demagnetizing fields the coercivity of the magnet is of major importance also.

2.1.5 Permanent Magnet subject to an External Demagnetising Field.

The magnet in figure (2.6) is subject to an external magnetic field as a result of current flowing in coil C in addition to a demagnetising field as a result of the air-gap in the circuit. The pole pieces are considered to be of infinite permeability in order to simplify the analysis.

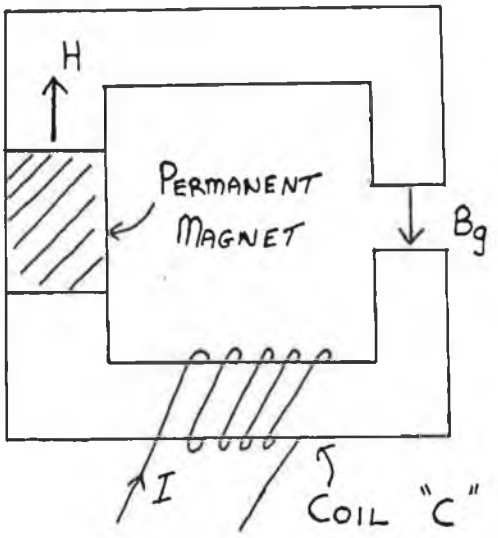

FIG. (2.6) Permanent Magnet in a Magnetic Circuit with an Air-Gap and Winding.

The major hystersis loop of the permanent magnet material is illustrated in figure (2.7). By referring to the major hysterisis loop we can determine the magnetising field necessary to produce a given flux density in the permanent magnet. Because the pole pieces are of infinite permeability, no m.m.f. drop occurs along them. In practice this is not true, however the assumption simplifies the discussion without invalidating the analysis.

To produce a flux density B_g in the air-gap requires the application of a magnetising field H_g given by the quotient B_g/μ_0 if the effects of fringing flux are ignored. The relationship between B_g and H_g is illustrated by the line o-a in figure (2.7). Thus in order to produce a given flux density B in the magnetic circuit the magnetising field components of the air-gap and the permanent magnet need to be added producing the dotted sheared hysteresis loop in figure (2.7) [Ref.7].

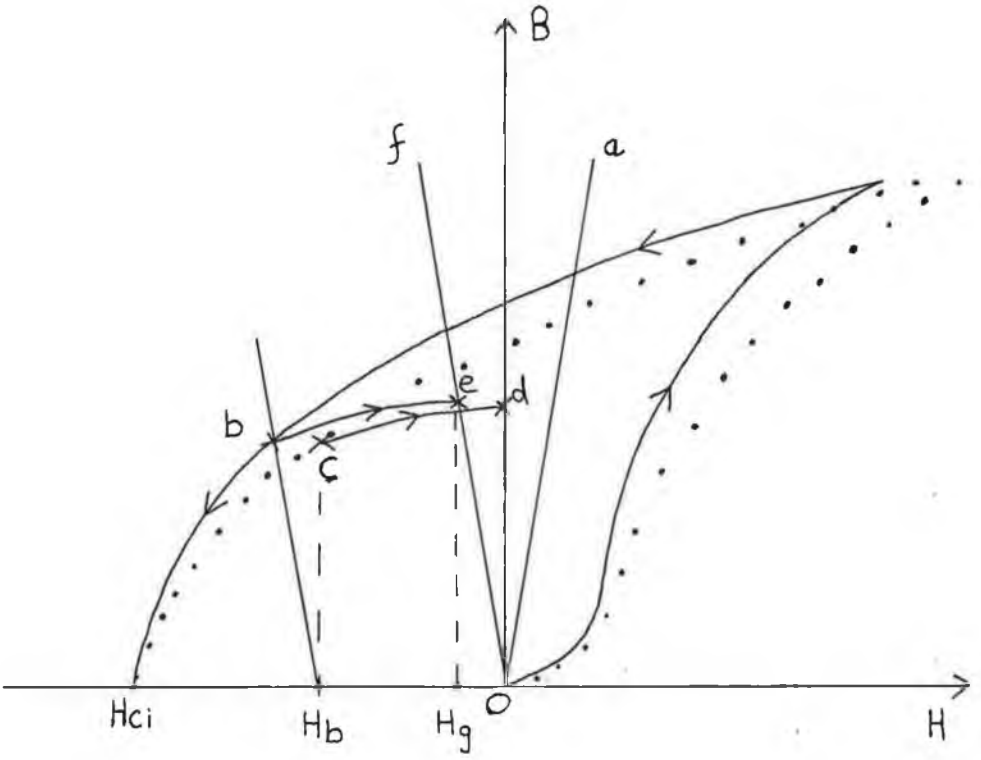

FIG. (2.7) Permanent Magnet Major Hysteresis and Sheared Hystersis Loops with load lines.

Consider that the permanent magnet has been magnetised and that a demagnetising field H_b is applied to the magnet such that the flux density in the magnet corresponds to point b on the major hysteresis loop or point c on the sheared hysterisis loop. If the demagnetising field is removed the flux density in the magnetic circuit recoils along the curve c-d as shown. However the operating point of the magnet moves along the curve b-e where e is a point on the air-gap line which has been drawn in the second quadrant. The presence of an air-gap in the magnetic circuit corresponds to the application of a demagnetising field H_g.

2.1.6 Graphical determination of the operating point of a magnet subject to an external demagnetising field.

If a straight line is drawn through the points H_b and b it will be parallel to the line o-f since the sheared hysteresis was produced by adding the major hysteresis

loop and air-gap components of H at a particular flux density. Therefore the operating flux density in a magnetic circuit containing a permanent magnet and an air-gap subjected to a demagnetising field H can be determined by constructing a line parallel to the air-gap permeance line through point H on the abscissa. This procedure can be used to graphically determine the demagnetising effect of armature reaction due to the stator currents on the magnet at the initial design stage.

2.2 COMPARISON OF THE SECOND QUADRANT CHARACTERISTICS OF PERMANENT MAGNET MATERIALS.

Figure (2.8) illustrates the second quadrant characteristics at room temperature of some permanent magnet materials available today. Alnico 5 has the highest residual magnetism but has very low coercivity indicating that while it can produce very high flux densities it is very prone to demagnetisation. On the other hand Ceramic 8 has much lower residual magnetism but has a considerably greater coercive force indicating that it can withstand greater demagnetising fields. The rare earth permanent magnet materials such as Nd-Fe-B and Sa-Co are characterised by straight lines in the second quadrant, combining relaticely high levels of residual induction with the highest values of coercivity. They are thus very suitable in applications where large demagnetising influences are likely to occur e.g. servo-motors. The rare earth materials also have the highest available energy products as high as 278 KJ/m^3 at room temperature in the case of some Nd Fe B grades as compared with an Alnico 5 energy product of approximately 40 KJ/m^3 and the use of such materials can contribute to an increase in the power to weight ratio of motors etc.

The recoil permeability of a rare earth permanent magnet is such that its recoil line lies along the major hysteresis loop and thus little or no permanent loss of induction occurs as a result of the repeated application and removal of demagnetising fields of moderate strengths. In figure (2.9) a typical demagnetising curve for a rare earth magnet is shown. If this material is subjected to a demagnetising field H_d the corresponding induction level in the material is B_d. If the demagnetising field is removed the induction will recoil along the major hysteresis loop to B_r which did not occur in the general case as illustrated in figure (2.4). Rare earth permanent magnets are thus inherently stabilised and are particularly suitable in dynamic applications subject to the application of magnetic fields of varying strengths.

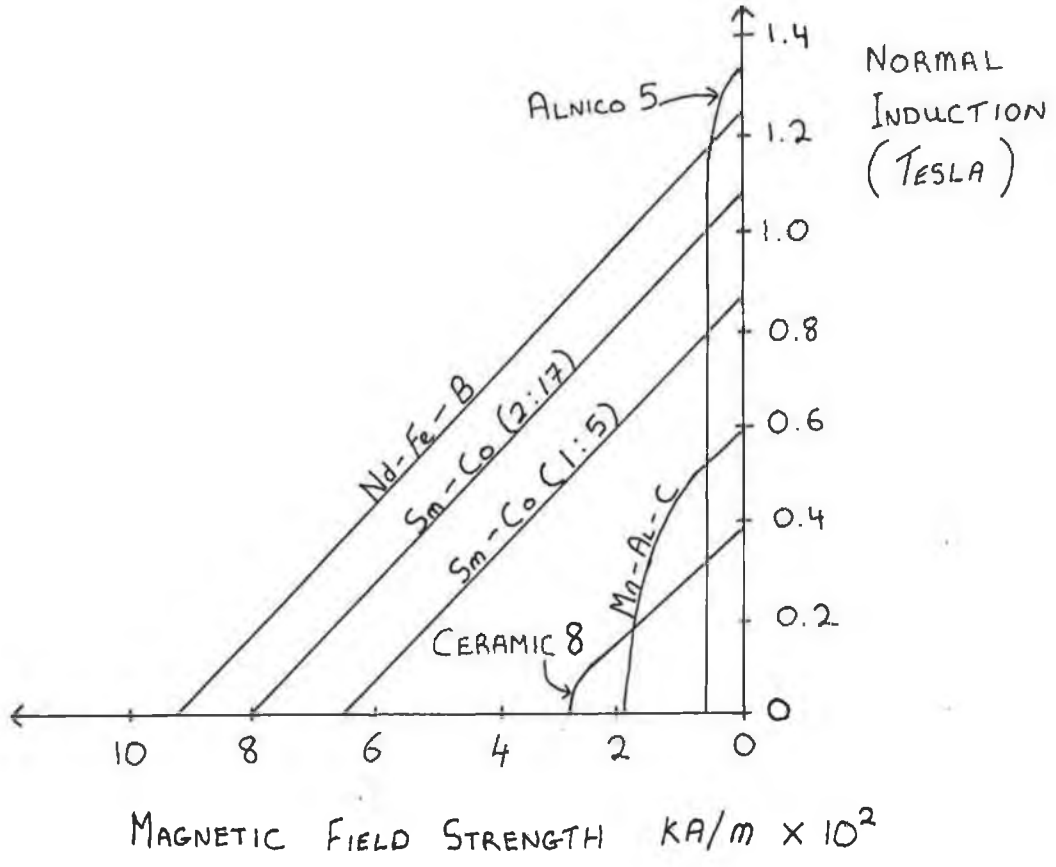

FIG. (2.8) Second Quadrant Characteristics of different Permanent Magnet materials.

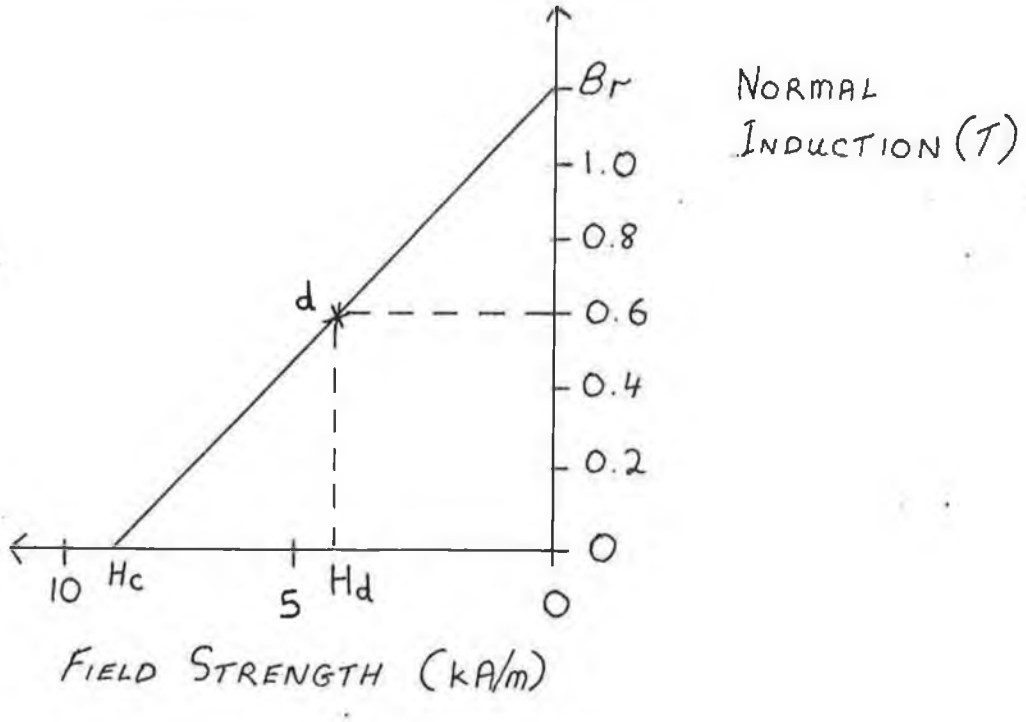

FIG. (2.9) Demagnetisation Curve of a Rare Earth Permanent Magnet material.

It is informative to examine the physical limit to the energy product BH_{max} for a given induction level in any permanent magnet. Figure (2.10) illustrates the normal and intrinsic induction curves B_i and B_n for an ideal permanent magnet (solid lines) and a rare earth permanent magnet (dotted lines). Equation (2.1) related the magnetic induction in a magnetic material to its intrinsic induction value and it can be shown [Ref. 7] for an ideal magnetic material whose intrinsic induction level does not decrease under the influence of a demagnetising field that,

$$H_{c\ max} = \frac{-B_i}{\mu_0} \qquad ...(2.10)$$

where $H_{c\ max}$ is the maximum coercivity.

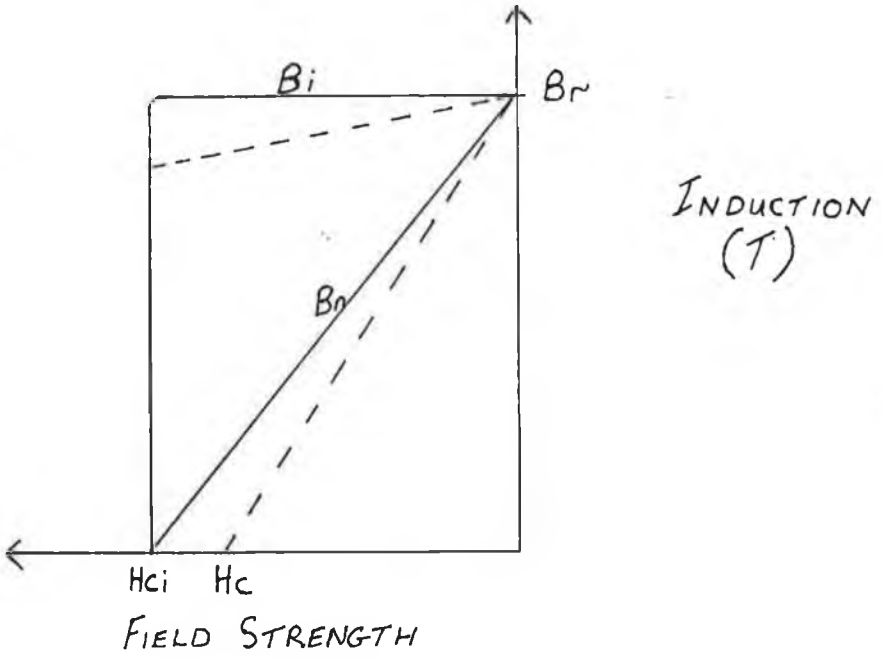

FIG. (2.10) Second Quadrant Characteristic for an Ideal Permanent Magnet and a Rare Earth Permanent Magnet.

The second quadrant curves of rare earth permanent magnet materials approach the ideal material charactistic quite closely at room temperature. However at elevated temperatures a reduction in the residual magnetism and coercivity is evident particularly in the case of some grades of Nd Fe B. Figure (2.11) shows the change in induction levels and coercivity for a comercial grade Nd Fe B with increasing temperature. It is seen that a "knee" appears in the second quadrant curve as the temperature increases and if the induction level in the material is

reduced below the knee of the curve a permanent loss of residual magnetism will be evident on the subsequent removal of the demagnetising influence. Developments leading to stabilised magnetic properties of Nd Fe B at elevated temperatures would be of great importance and currently a lot of research is been undertaken by magnet manufacturers worldwide.

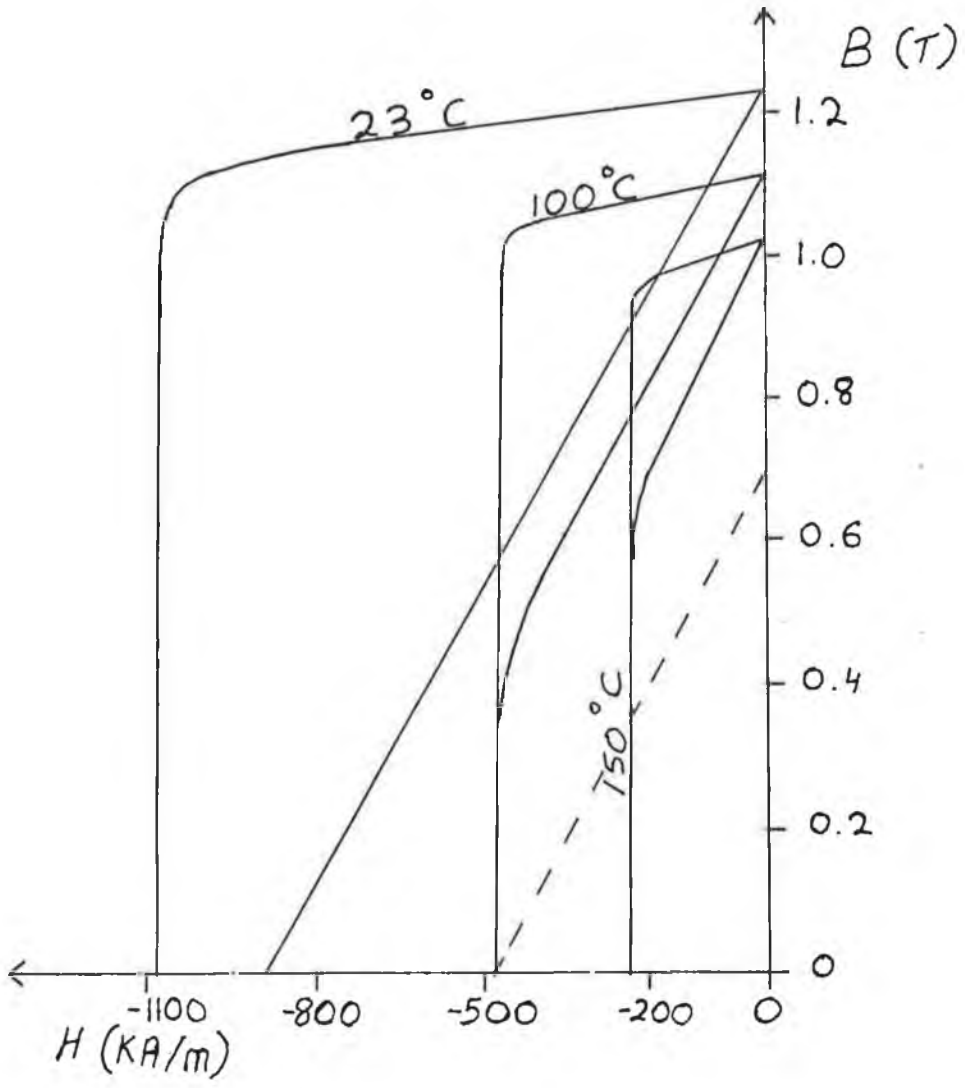

FIG. (2.11) Variation with Temperature of Second Quadrant Characteristic for a typical Nd-Fe-B material.

2.3 MODELLING OF RARE EARTH PERMANENT MAGNET SYSTEMS.

2.3.1 Introduction.

The linear relationship between the magnetic induction and the demagnetising force in the second quadrant of rare earth permanent magnet systems suggests the use of a linear model to solve magnetic problems. It can be shown [Ref. 8 and 9] for any rare earth permanent magnet in a magnetic circuit that,

$$\Phi_m = \frac{B_r/\mu_r . L_m \pm n.I}{R_m + R_t} \qquad \ldots(2.10)$$

where L_m is the magnet length

B_r/μ_r is the average magnetising field strength over the length of the magnet

$n.I$ are the ampere turns opposing or supporting the internal permanent magnet field

R_m equals $L_m/(\mu_r . A_m)$ the internal magnet reluctance

R_t is the total reluctance of the magnetic circuit exclusive of the magnet

The equivalent magnetic circuit of equation (2.10) is shown in figure (2.12). The second quadrant characteristic can also be rescaled as shown in figure (2.13) where $F_m = H_m.L_m$, the m.m.f. due to the magnet, $\Phi_m = B_m.A_m$ is the magnet flux and A_m is the magnet area. Φ_m can be considered to be the short circuit flux and F_m can be considered to be the open circuit magnet m.m.f. The quotient Φ_r/F_m is the slope of the demagnetising curve and can be regarded as the permeance of the magnet P_m since,

$$\frac{\Phi_m}{F_m} = \frac{B_r.A_m}{H_m.L_m} = \frac{A_m}{\mu_r.L_m} = \frac{1}{R_m} = P_m$$

To demonstrate the equivalence between the two representations of the magnetic circuit consider that I is zero in equation (2.10). In this instance the magnetic flux is given by,

$$\Phi_m = \frac{H_m.L_m}{R_m+R_T}$$

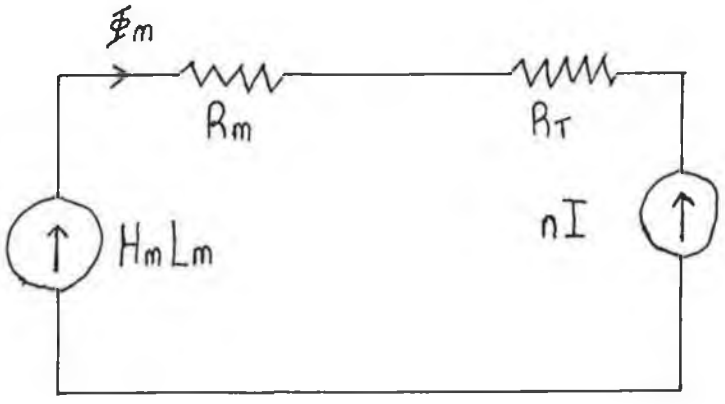

FIG. (2.12) Equivalent Magnetic Circuit of Permanent Magnet subject to a Demagnetising Field.

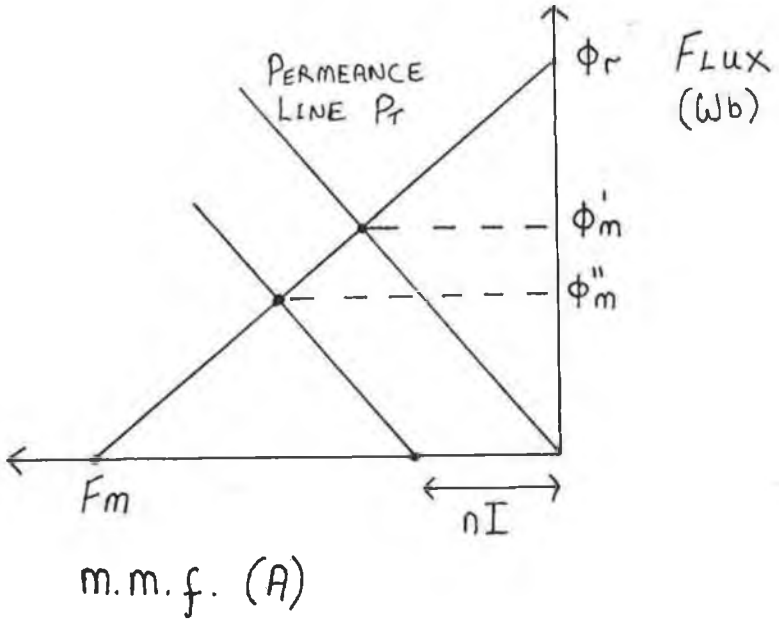

FIG. (2.13) Rescaled Second Quadrant Characteristic of a Permanent Magnet material.

If a line with slope P_t is drawn from the origin it will intersect the demagnetising curve at point F_n,Φ_m' in figure (2.13). Referring back to equation (2.7) with K_{phi} equal to one and P_t equal to the gap reluctance yields,

$$B_m'.A_m = \Phi_m' = F_n.P_t = \frac{F_m - \Phi_m'/P_m}{R_t}$$

Therefore $\Phi_m' = \frac{F_m}{R_t + R_m}$ as obtained from the equivalent circuit.

Similarly it can be shown that if an external magnetic field is applied to the circuit the graphical construction shown in figure (2.13) (with the load line shifted to the left by an amount corresponding to the applied m.m.f.) yields the same flux density as the equivalent circuit representation.

2.3.2 Modelling of the motor magnetic circuit.

Figure (2.14) represents the magnetic equivalent circuit of two adjacent poles in a permanent magnet motor with no current flowing in the stator windings. The following definitions apply in respect of figure (2.14),

R_t is the tooth reluctance per pole
R_m is the magnet reluctance
R_g is the air-gap reluctance
R_y is the stator yoke reluctance
R_r is the rotor yoke reluctance
F_m is the average magnet m.m.f.
Φ is the magnet flux in the circuit
R_l is the reluctance of the magnet leakage paths

This circuit can be reduced to that of figure (2.15) for the purpose of calculating the air-gap flux Φ_g. In this circuit R_{tot} is the equivalent reluctance of R_g,R_r,R_t and R_y. It can be shown, if the reluctance of the Iron paths is ignored that,

$$\Phi_g = \frac{A_m}{K_{phi}\left[\frac{1}{B_r} + \frac{A_m.L_g}{K_{phi}.\mu_0.A_g.H_c.L_m}\right]} \quad \ldots\ \text{EQN (2.11)}$$

where K_{phi} is the ratio of total flux to gap flux

A_g is the air–gap area

A_m is the magnet area

L_g is the air–gap length

L_m is the magnet length

This formula can be used to make an initial estimate of the air-gap flux. Using this estimate it is possible to calculate the flux density in the Iron parts of the motor and hence to estimate the m.m.f. drop along these parts. By an iterative process the actual air-gap flux can then be calculated taking account of Iron saturation.

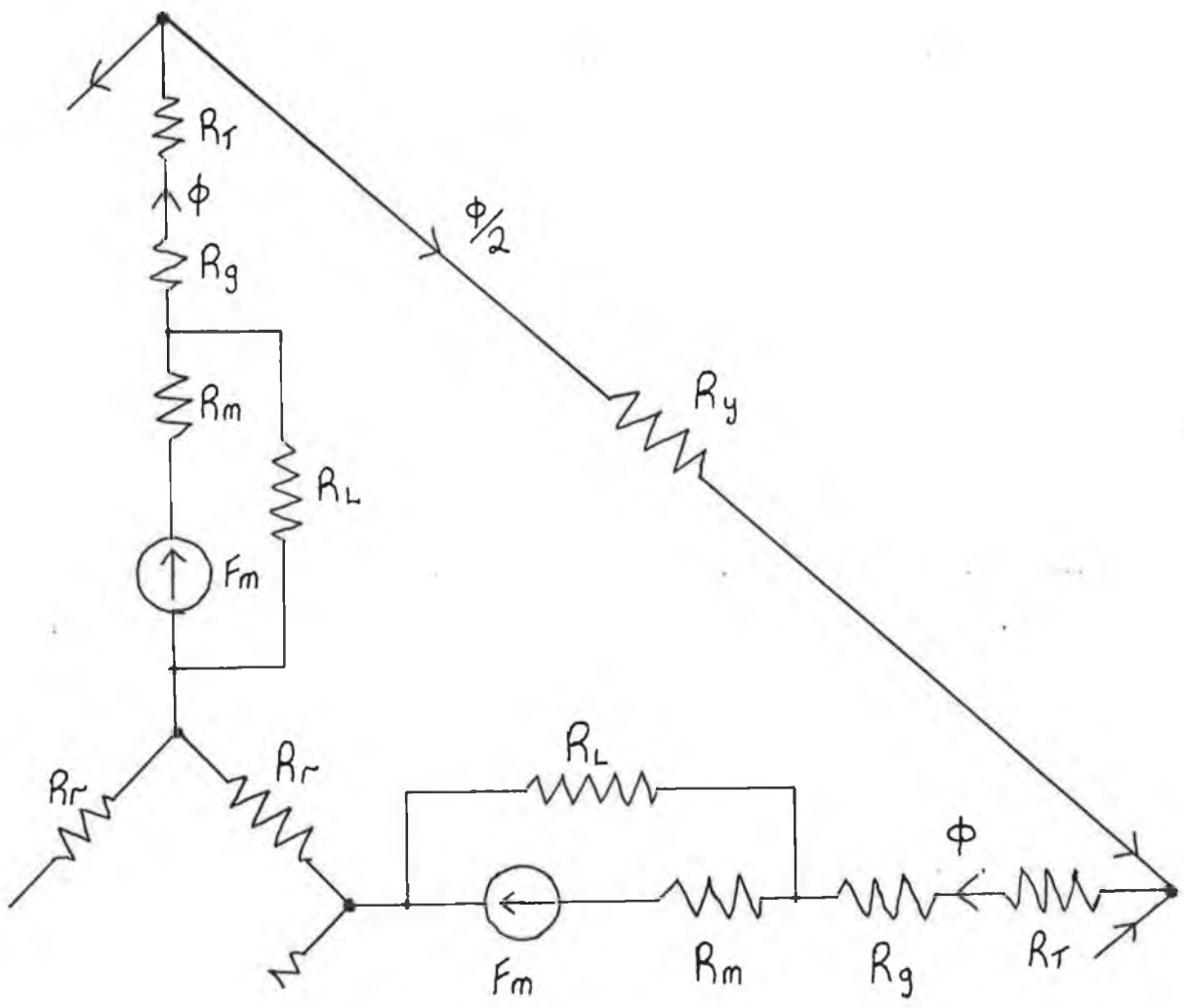

FIG. (2.14) Equivalent Magnetic Circuit of two poles of a permanent Magnet motor.

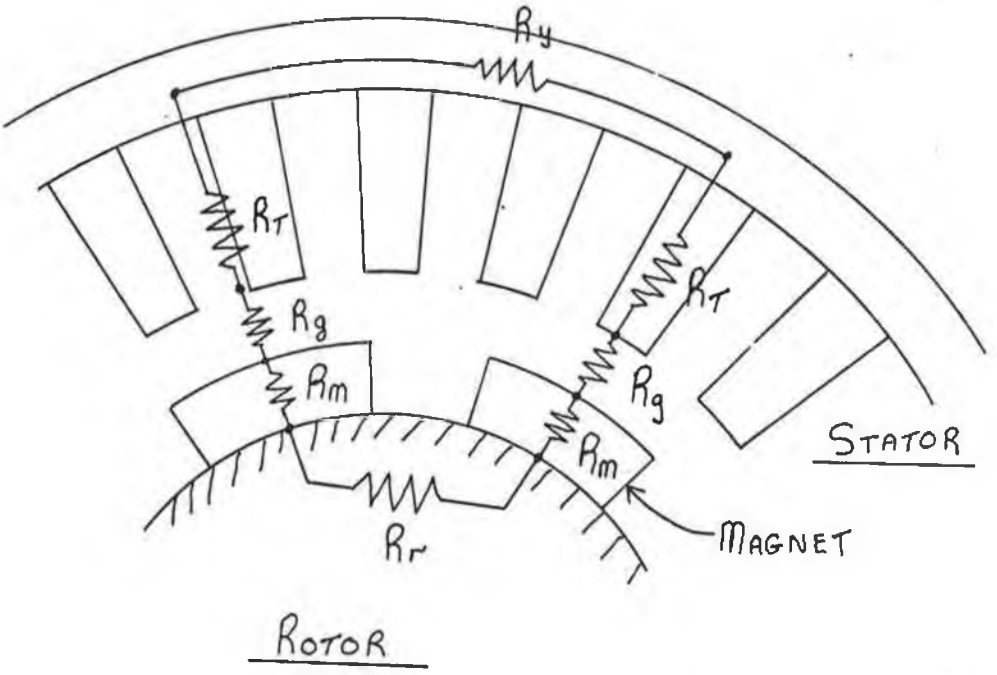

FIG. (2.14b) Equivalent Magnetic Circuit of two poles of a Permanent Magnet motor superimposed on physical motor arrangement.

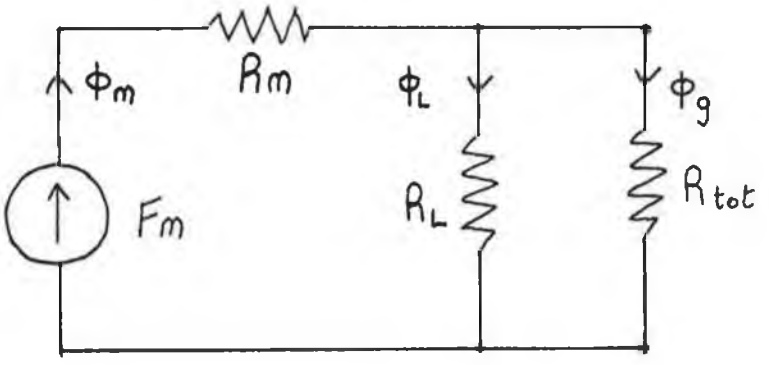

FIG. (2.15) Simplified equivalent Magnetic Circuit of a P.M. motor.

2.4 STABILITY OF RARE EARTH PERMANENT MAGNETS.

This discussion will use a comercially available grade of Nd Fe **B** as an illustrative example when considering the stability of rare earth permanent magnets although the stability criteria can be similarily applied to any other permanent magnet material. The stability of a permanent magnet is very important as many magnet applications are sensitive to changes in permanent magnet properties. Magnet stability may be considered under the following sub headings,

(1) Structural stability
(2) Magnetic field effects
(3) Temperature effects

2.4.1 Structural Stability.

Neodymium magnets tend to lack ductility, are brittle and require careful machining and assembly techniques. Neodymium magnets are a little less difficult to machine than Samarium Cobalt magnets but a grinding process is still required to shape the magnet face. Typical mechanical properties of the Nd-Fe-B and Sa-Co materials are presented below for comparison purposes.

	Nd-Fe-B		Sa-Co	
Tensile strength	8.3×10^7	($N\ m^{-2}$)	7.9×10^7	(Nm^{-2})
Compressive strength	7.6×10^8	($N\ m^{-2}$)	—	
Flexural strength	2.4×10^8	($N\ m^{-2}$)	—	
Density	7.4×10^3	($Kg\ m^{-3}$)	8.2×10^3	($Kg\ m^{-3}$)

One important feature of Nd Fe B magnets is the tendancy of the magnets to rapidly oxidize and the materials manufacturer recommends coating the exposed magnet faces with epoxy to prevent this.

2.4.2 Magnetic Field Effects.

Figure (2.11) shows the demagnetising curve of a typical Nd Fe B magnet at 23 degrees C and 100 degrees C. As was previously discussed, the recoil of the induction B is along the straight line portion of the curve and if the material is at a temperature of 23 degrees C it is possible to reduce the normal induction to zero with the application of a demagnetising field without causing permanent loss of

magnetism. At 100 degrees however if the normal induction of the magnet is reduced to zero a permanent loss of residual magnetism will occur as shown by the dotted recoil line in the figure. In order to avoid permanent loss of magnetism in an application the magnetic circuit should be designed so that the operating of the magnet is at all times to the right of the knee of the curve for the range of temperatures over which the magnet must operate. This guideline applies both in the case of applied demagnetising fields and of changing circuit reluctances.

2.4.3 Temperature Effects.

All magnetic materials exhibit flux changes and some irreversible losses with increasing temperature. These losses can be divided up as follows,

(a) Irreversible losses
(b) Reversible losses
(c) Long term losses

Irreversible Losses.

These losses occur when the magnet is initially subjected to high temperature cycles. These losses may be irrecoverable (as a result of metallurgical changes) or recoverable (losses can be regained through remagnetisation). Irreversible-irrecoverable losses in the case of Nd-Fe-B magnets exposed to temperatures of up to 175 degrees C are negligible. Irreversible-recoverable losses vary as a function of temperature as well as of the operating point of the magnet. This dependence is illustrated in figure (2.16) where the operating point of the magnet is determined by the permeance of the magnetic circuit and any additional demagnetising fields. In the case of Nd-Fe-B magnets these losses do not occur instantaneously but occur gradually over a period of two hours. This data is extracted from technical literature supplied by Crucible Materials Corporation concerning their range of Crumax Nd-Fe-B magnet materials.

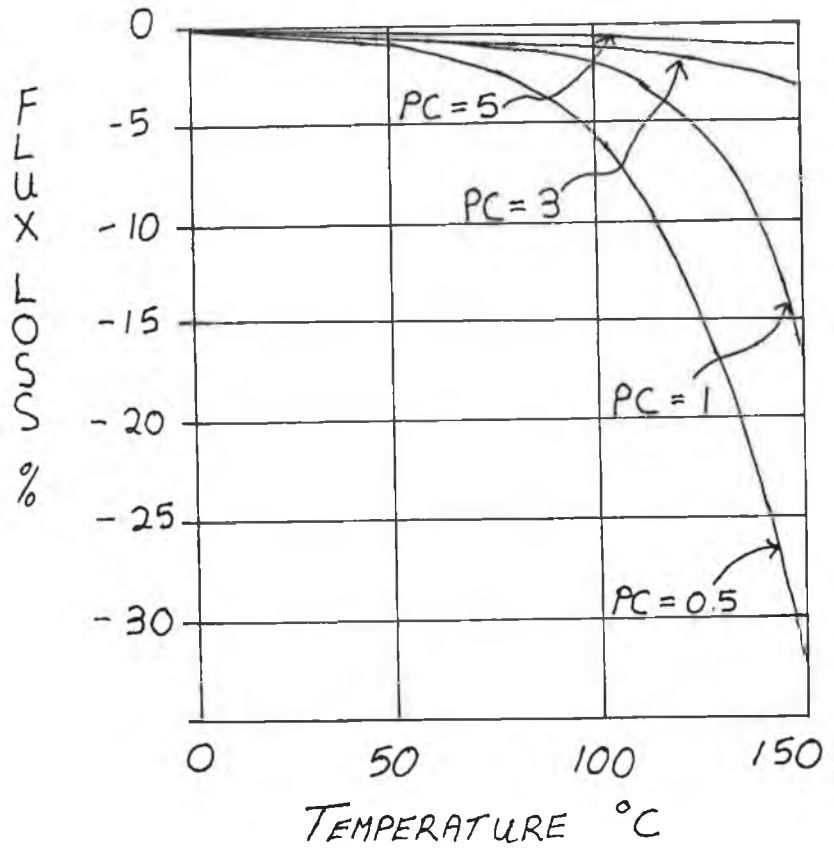

FIG. (2.16) Variation of Irreversible Losses with Magnet Temperature and with slope of Magnetic Circuit Permeance Line (PC).

Reversible Losses.

These are temporary losses that occur as a function of increasing temperature but are completely recovered when the material is returned to it's original temperature as shown in figure (2.11).

Long Term Losses.

These are permanent losses in magnets that occur only after exposure to elevated temperatures for an extended period of time. In the case of Nd-Fe-B magnets exposed to 150 °C an initial irreversible loss depending on the operating point of the magnet occurs as previously described. Further exposure to such temperatures and magnetic operating conditions do not lead to additional flux losses and thus the magnets have been stabilised for these conditions. This fact is illustrated in figure (2.17).

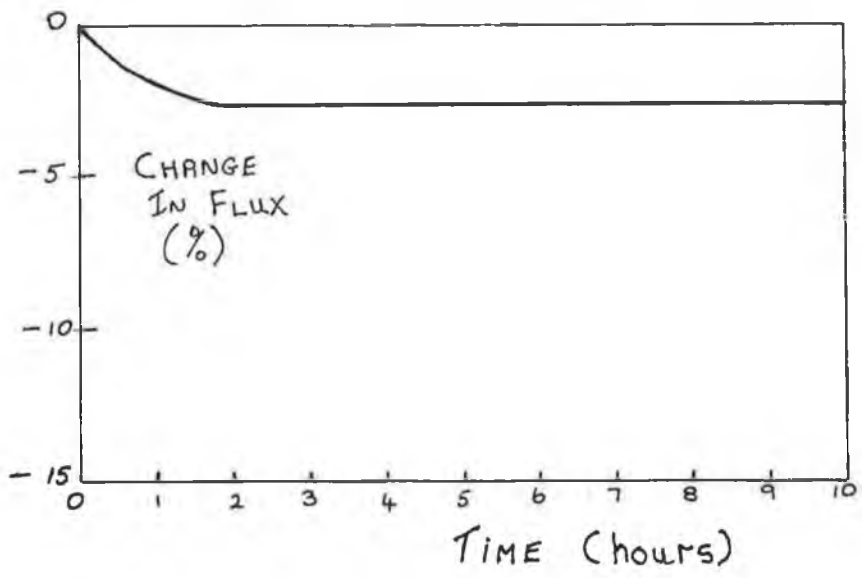

FIG. (2.17) Long Term Flux Losses for Nd-Fe-B material.

Dimensional Changes.

The magnet physical dimensions also vary slightly with temperature and typical values for Nd-Fe-B and Sa-Co magnets are given below,

Perpendicular to magnetic orientation	-5×10^{-6} °C^{-1}	(Nd-Fe)
	11×10^{-6} °C^{-1}	(Sa-Co)
Parallel to the magnetic orientation	3×10^{-6} °C^{-1}	(Nd-Fe)
	9×10^{-6} °C^{-1}	(Sa-Co)

Chapter 3.

STATOR WINDING ANALYSIS.

3.1 INTRODUCTION AND OUTLINE OF METHOD OF ANALYSIS.

In a polyphase a.c. induction or synchronous motor the stator windings are distributed in such a manner as to produce a rotating magnetic field when supplied by a balanced polyphase voltage source. Usually this magnetic field is approximately sinusoidal in nature, containing a relatively large fundamental wave along with smaller harmonic waves. It is the interaction of this fundamental wave with the rotor field that produces useful motor torque. On the other hand the harmonic waves rotate at different speeds to the fundamental and tend to produce pulsating torques. It is therefore important to determine the relative magnitudes of the fundamental and harmonic waves produced by the windings in order to be able to evaluate the effect of the winding distribution on motor performance. A method of analysis is outlined which is applicable to any a.c. winding including fractional slot windings (so called because the quotient slot number / (pole number x phase number) is not an integer). This method of analysis is described in references [10], [11] and [12]. Further information on the layout of fractional slot windings may be obtained in reference [13].

3.1.1 Outline of Method of Analysis.

Two basic assumptions are made in this analysis, namely,

(1) The magnetomotive force produced by a coil is concentrated at slot openings of negligible width.

(2) The reluctance of the Iron on both sides of the air gap is considered to be negligible.

Consider a single coil of M ampere turns carrying a d.c. current as shown in figure (3.1). This figure shows the developed air gap of two pole pitches and coil pitch p is less than one. The flux wave produced will consist of two dissimilar rectangles assuming the rotor to be of the cylindrical type.

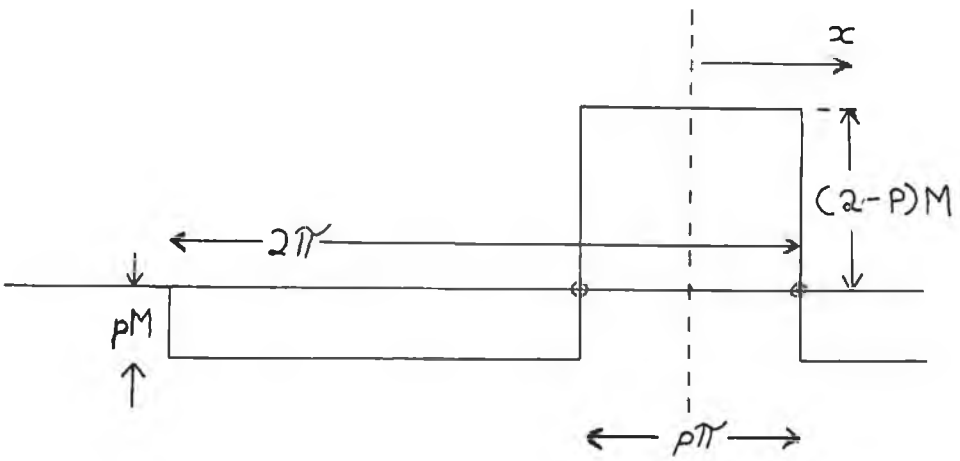

FIG. (3.1) Developed air-gap m.m.f. of a single coil over two pole pitches where p is the coil pitch and M is the ampere turns of the coil.

Applying the method of Fourier analysis to the air gap m.m.f. m, produced by the windings results in the following expression,

$$m = \frac{4.M}{\pi}\left[\sin(p\pi/2)\cos(x) + \frac{1}{2}.\sin(2p\pi/2)\cos(2x) + \text{-----} + \frac{1}{k}\sin(kp\pi/2)\cos(kx) + \text{--------}\right]$$

...(3.1)

In equation (3.1) x is the distance along the air gap periphery referenced to the centre of the coil as shown in figure (3.1). If alternating current flows in the coil instead of d.c. current the m.m.f. M in equation (3.1) takes the form M.coswt, an m.m.f. pulsating in time but stationary in space. In this case $w = 2\pi f$ where f is the alternating frequency of the current. Consider the k^{th} harmonic m_k of the pulsating m.m.f.,

$$m_k = \frac{4.M}{\pi.k}.\left[\sin(kp\pi/2)\cos(kx)\cos(2\pi ft)\right]$$

$$= \frac{2.M}{\pi.k}\sin(kp\pi/2).\left[\cos(kx-2\pi ft) + \cos(kx+2\pi ft)\right]$$

...(3.2)

It is seen that the stationary in space, pulsating in time m.m.f. can be resolved into two equal, constant-magnitude m.m.f.s revolving in opposite directions at the same speed of 2f pole pitches per second (f in Hz). Since the k^{th} harmonic has k times as many poles as the fundamental per unit length of air gap periphery, it's component m.m.f.s will move at 1/k times the speed of the fundamental component m.m.f.s.

Each identical coil in a phase will produce a similar set of forward and backward moving m.m.f.s, displaced in space by an angle corresponding to the distribution of the coils around the air gap periphery. The resultant m.m.f. m_r, produced by a single phase belt is obtained by the vector addition of the m.m.f.s produced by the n individual coils of the phase belt.

$$m_r = \frac{2.M.n}{\pi}.\left[\begin{array}{l} kp_1kd_1.\cos(x-wt) + \frac{1}{2}\,kp_2kd_2.\cos(2x-wt) + \text{----} \\ \quad + \frac{1}{k}\,kp_kkd_k.\cos(kx-wt) + \text{----------} \\ \\ + kp_1kd_1.\cos(x+wt) + \frac{1}{2}\,kp_2kd_2.\cos(2x-wt) + \\ \quad \text{-----} + \frac{1}{2}\,kp_kkd_k.\cos(kx-wt) + \text{---------} \end{array}\right]$$

where kp_k = k^{th} pitch factor

kd_k = k^{th} distribution factor

...(3.3)

Consider the case of a symmetrical polyphase winding having an integral number (q, say) phase belts per pole. All phase belts are identical but are spaced 360/2q electrical degrees apart and carry currents 360/2q degrees apart in time, if fed from a balanced q phase voltage supply. Figure (3.2) represents two poles of such a winding with q = 3, i.e a symmetrical three phase winding.

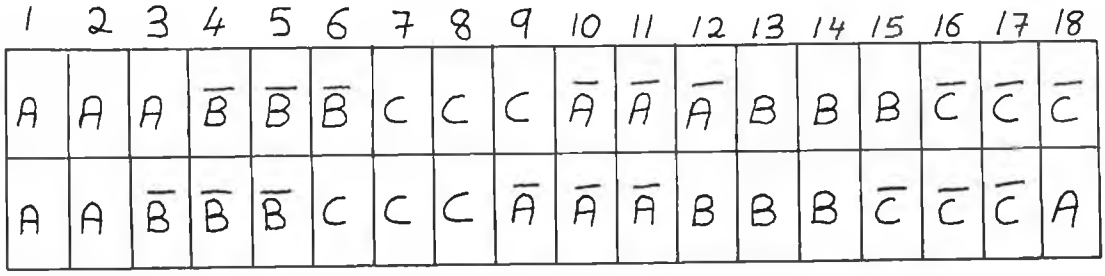

FIG. (3.2) Layout of Phase Conductors in a typical three phase symmetrical winding.

The letters A, B, C, in figure (3.2) represent the location of the phase conductors in the slots numbered one to eighteen and the bar sign (-) indicates current flow in the opposite direction to the reference direction of current flow. It is evident from fig (3.2) that consecutive phase belts in the same phase winding are spaced 180 electrical degrees apart and carry currents that are opposite in time phase. The m.m.f. m_{ph} of the complete phase winding expressed in ampere turn/pole will be obtained by adding two series of the form in equation (3.3), one of which has x replaced by $x + \pi$ and the sign of each term reversed and dividing the result by two since the m.m.f.s of both poles act on the same flux path across two air gaps in series. Performing this operation gives rise to the following expression,

$$m_{ph} = \frac{2.M.n}{\pi} \left| \begin{array}{l} kp_1kd_1.\cos(x-wt) + \frac{1}{3} kp_3kd_3.\cos(3x-wt) \\ \qquad + \frac{1}{5} kp_5kd_5.\cos(5x-wt) + \text{---------} \\ + kp_1kd_1.\cos(x+wt) + \frac{1}{3} kp_3kd_3.\cos(3x+wt) \\ \qquad + \frac{1}{5} kp_5kd_5.\cos(5x+wt) + \text{-------} \end{array} \right| \quad \ldots(3.4)$$

It will be observed that a symmetrical polyphase winding contains no even harmonics of m.m.f. since $\cos(2k(x+\pi)) = \cos(2kx)$ and consists of two waves, one,

forward revolving, the other, backward revolving. All that remains to be done now, is to combine the m.m.f.s for each of the q phases to obtain the total m.m.f. of the polyphase winding. If this is done for a three phase winding with sixty degree phase belts the m.m.f. m_t of the winding is given by,

$$m_t = \frac{6.M.n}{\pi} \left[kpkd.\cos(x-wt) + \frac{1}{5} kp_5kd_5.\cos(5x+wt) + \frac{1}{7} kp_7kd_7.\cos(7x-wt) + \text{-------} \right] \quad ...(3.5)$$

where, m_t is the total winding m.m.f.
M is the peak ampere turns per coil,
n is the number of coils per pole per phase.

Thus the m.m.f. m_t can be considered to be composed of a number of constant magnitude, sinusoidal revolving fields some of which rotate in the forward direction, (fields of order 1, 7, 13, etc) and the others which rotate in the backward direction (fields of order 5, 11, 17, etc). As mentioned previously the k^{th} harmonic will move at a speed of 1/k times the speed of the fundamental field.

3.1.2 Fractional Slot Windings.

The method of winding analysis just outlined applies to symmetrical windings in that kp and kd are relatively easy to calculate. However in the case of fractional slot windings this is not the case because the windings are not symmetrical. Alger [Ref 10] described a method using space phasors to calculate kpkd for each harmonic as follows,

(1) Each coil side in a slot is given a magnitude depending on the number of turns in the coil and an angle, depending on the slot location in relation to a reference slot and the order of harmonic under consideration.

(2) In addition, each coil side is given a plus or minus sign depending on the direction of current flow in the slot.

(3) The phasors so defined of one phase are added vectorially to give kp.kd.s of that phase, (where s is the number of coil sides per phase).

(4) Processes 1, 2, and 3 are repeated for each of the phases in turn.

(5) The forward and backward fields of the complete winding are then calculated from the vector sum of the individual phase components taking into account the time - phase angle of the phase currents multiplied by $\sqrt{2}$ times I_{rms} divided by π.

Stepina [Ref. 12], in a recent article describes a method of stator winding analysis similar to Alger's but suggests the use of matrix multiplication as a more flexible and efficient calculating method. A computer program to calculate the winding harmonics utilising Alger's method was written (Appendix B). This program was used to calculate the winding harmonics of a twelve pole winding using 36, 39 and 45 slots. A twelve pole winding was investigated as this corresponds to the winding used in the Moog 304 series motors one of which was used as an experimental basis for this project.

3.1.3 Winding Layout.

The first step in the analysis of the different windings was to specify the physical arrangement of the conductors in the slots. This necessitated the design of the 36 and 45 slot windings and the determination of the 39 slot winding. The latter was not a problem since production drawings were available. The 36 and 45 slot windings were designed using the methods described in reference [13] which lead to the largest fundamental m.m.f. possible for a given number of slots, poles and phases. The three different winding arrangements are shown in figures (3.3), (3.4) and (3.5), where A,B and C represent the phase conductors and the bar sign represents negative current flow. The slot numbers serve as references only while the descriptions slot top and slot bottom are arbitrary.

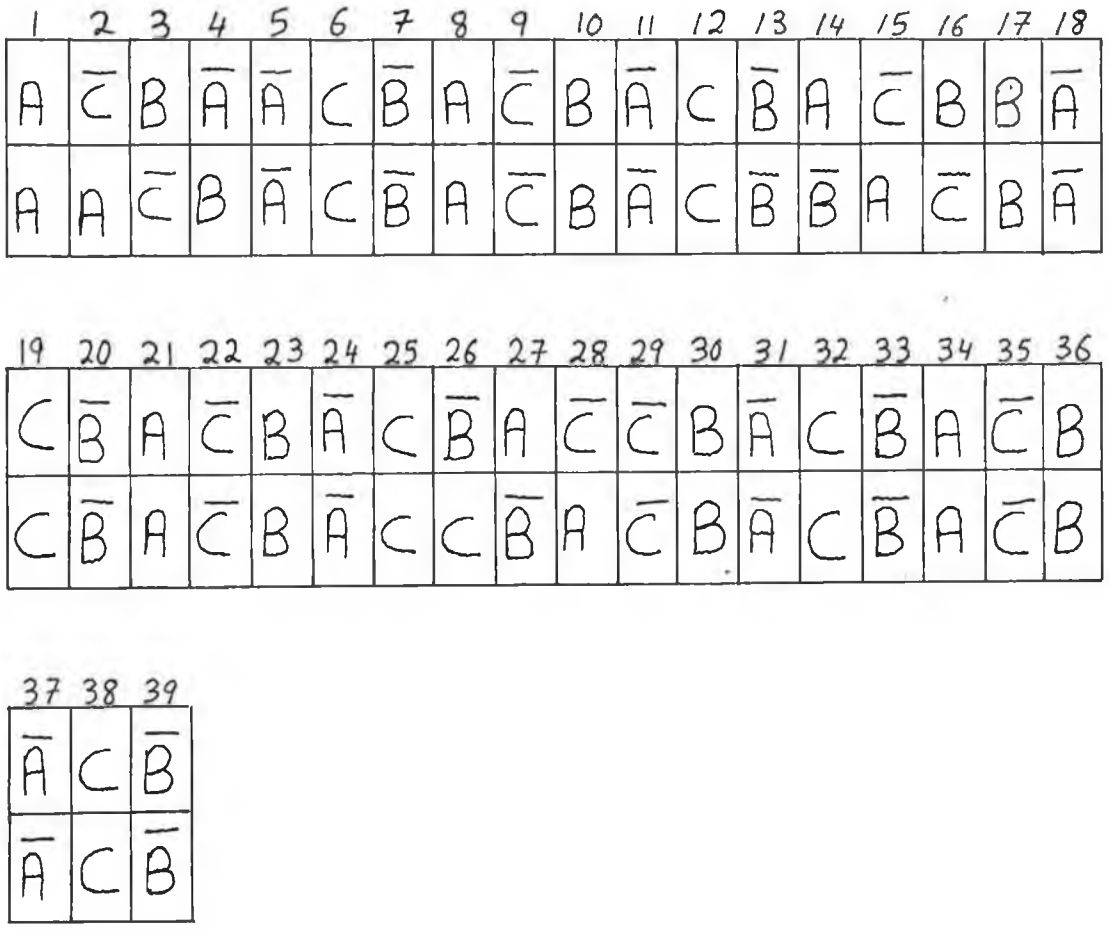

FIG. (3.3) Winding layout of a 12 Pole, 39 Slot, 3 Phase motor. The symbols A, B, C represent the three sets of phase conductors and the Bar sign (–) indicates current flow in the negative Reference direction.

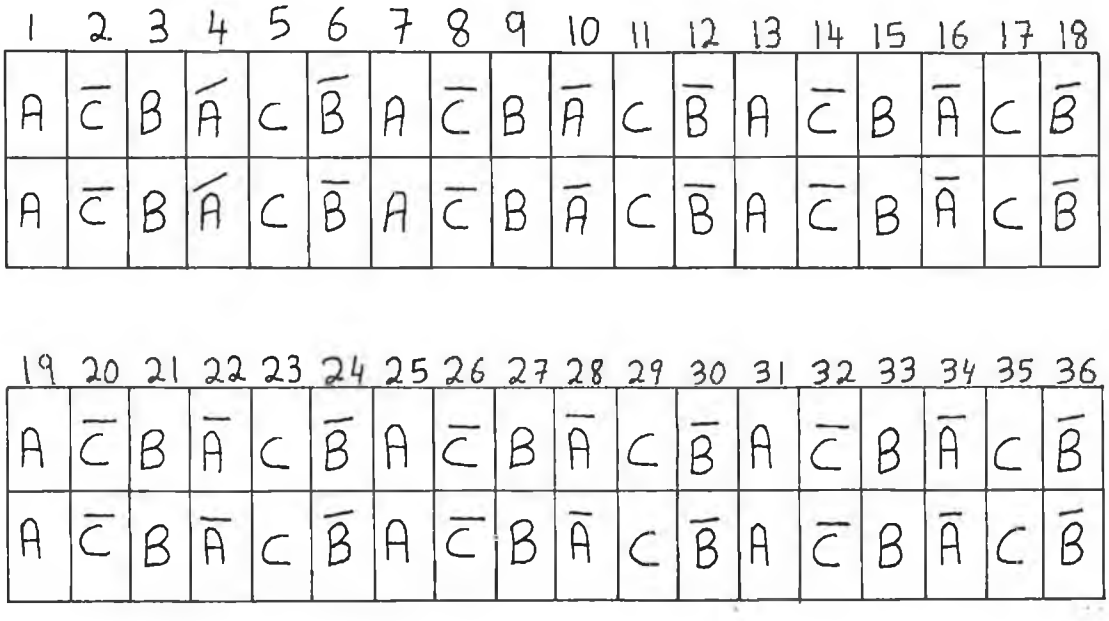

FIG. (3.4) Winding layout of a 12 Pole, 36 Slot, 3 Phase motor. The symbols A, B, C represent the three sets of phase conductors and the Bar sign (–) indicates current flow in the negative Reference direction.

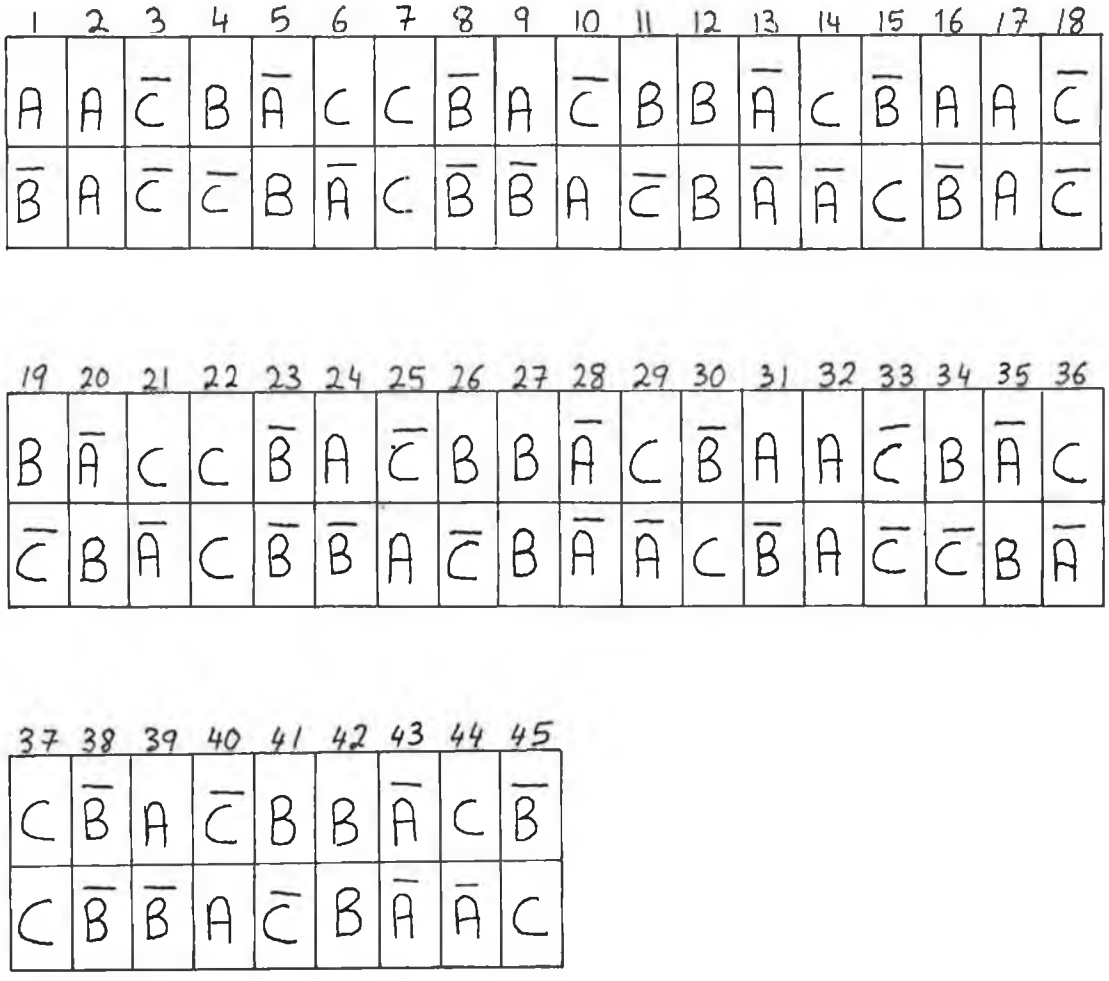

FIG. (3.5) Winding layout of a 12 Pole, 45 Slot, 3 Phase motor. The symbols A, B, C represent the three sets of phase conductors and the Bar sign (–) indicates current flow in the negative Reference direction.

3.1.4 Calculated Harmonic m.m.f.s.

Tables (1), (2) and (3) are a summary of the calculated harmonics for the three winding configurations. All the harmonics are given as percentages of the 6^{th} harmonic since for a twelve pole arrangement this corresponds to the primary field in the air-gap of the motor. It is seen that significant m.m.f. sub-harmonics (relative to the primary field) are present in the case of the 39 and 45 slot configurations as a result of the lack of winding symmetry. On the other hand, in the 36 slot configuration no sub-harmonics are present due to the symmetrical nature of the winding. However the 36 slot windings, being full pitch have significant higher order harmonics as can be seen in Table (3).

TABLE (1) WINDING M.M.F. HARMONIC ANALYSIS

39 SLOTS, 3 PHASES, 12 POLES.

Harmonic Order	Winding Factor ($K_p.K_d$)	Forward Field Magnitude	Backward Field Magnitude
1	0.0184	4.40	7.80
2	0.0358	7.50	2.7
3	0.0855	17.4	2.80
4	0.0633	5.00	6.30
5	0.0719	5.60	-
6	0.9471	100.0	-
7	0.0764	4.10	3.90
8	0.0719	3.0	-
9	0.1590	10.6	-
10	0.0510	2.1	1.5
16	0.0510	1.3	-
17	0.0633	-	1.2
19	0.0764	1.5	-
20	0.0764	-	1.4
30	0.1590	-	3.2
33	0.9471	-	18.15
36	0.0855	-	1.45
42	0.0855	1.2	-
45	0.9471	13.3	-
48	0.1590	1.98	-
69	0.1590	-	1.4
72	0.9471	-	8.3
84	0.9471	7.1	-
87	0.1590	1.1	-
111	0.9471	-	5.4
123	0.9471	4.9	-
150	0.9471	-	4.02
162	0.9471	3.7	-

TABLE (2) WINDING M.M.F. HARMONIC ANALYSIS

45 SLOTS, 3 PHASES, 12 POLES.

Harmonic Order	Winding Factor ($K_p.K_d$)	Forward Field Magnitude	Backward Field Magnitude
3	0.0878	-	19.3
6	0.9099	100.0	-
12	0.0601	-	3.30
21	0.1041	-	3.30
24	0.1041	24.0	-
33	0.0601	1.20	-
39	0.9099	-	15.4
42	0.0878	1.3	-
48	0.0878	-	1.30
51	0.9099	11.8	-
66	0.1041	-	1.00
84	0.9099	-	7.16
96	0.9099	6.24	-
129	0.9099	-	4.65
141	0.9099	4.26	-
174	0.9099	-	3.45

TABLE (3) WINDING M.M.F. HARMONIC ANALYSIS

36 SLOTS, 3 PHASES, 12 POLES.

Harmonic Order	Winding Factor ($K_p.K_d$)	Forward Field Magnitude	Backward Field Magnitude
6	1.00	100.0	-
30	1.00	-	20.0
42	1.00	14.3	-
66	1.00	-	9.1
78	1.00	7.7	-
102	1.00	-	5.89
114	1.00	5.28	-
138	1.00	-	4.35
150	1.00	4.00	-
174	1.00	-	3.45

3.2 EXPERIMENTAL VERIFICATION OF ANALYSIS.

If the analysis described in this chapter was to be used to evaluate the merits and demerits of different winding arrangements, it was important to validate the analysis experimentally. Two different experimental methods were considered as follows,

3.2.1 Experimental Method (1).

This consisted of a pick–up coil placed in an air gap between the wound stator and a concentric cylindrical Iron rotor as illustrated in Fig. (3.6)

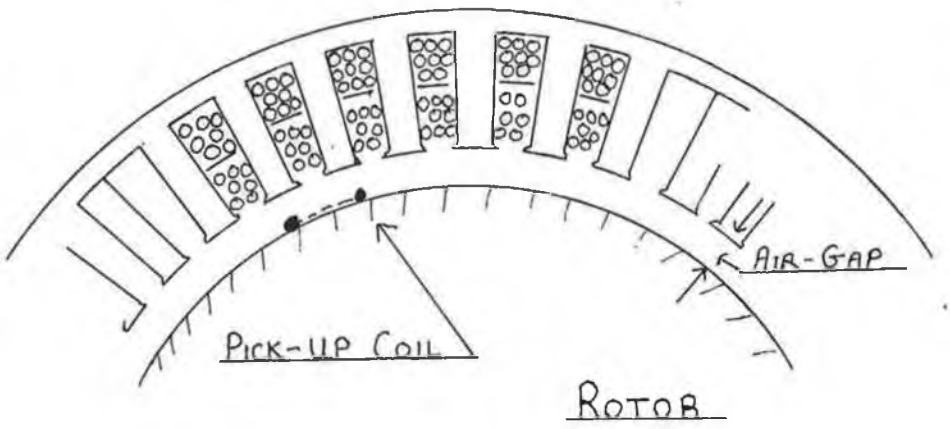

FIG. (3.6) Location of the Voltage Pick-Up coil in the motor Air-gap.

If the stator phases are energised from a balanced polyphase current source then the air gap m.m.f. should consist of a series of forward and backward rotating fields as previously outlined. These can be represented by a series as follows,

$$Mgap = F.\left[kw_1.\cos(x-\omega t) + \frac{1}{k} kp_k.\cos(k.x\pm\omega t) + \text{-----} \right]$$

where $F = 6Mn/\pi$ as before

and $kw_1 = k^{th}$ winding factor

...(3.6)

Assume that the stator, rotor and pick-up coil are stationary with respect to each other and consider the voltage induced in the coil as a result of the stator m.m.f.'s. If it is assumed that each of the rotating m.m.f. fields produce a flux

wave in proportion to its magnitude i.e. neglecting saturation and slotting effects then in general the individual induced voltages in the pick-up coil can be represented as,

$$v_k = \frac{d}{dt}(\varphi_k) \qquad ...(3.7)$$

where φ_k is the net k^{th} harmonic flux linked by the pick-up coil and in general can be represented by

$$\varphi_k = \frac{F}{R_g} \cdot \frac{1}{k} \cdot kp_k \cdot \cos(\pm \omega t) \cdot k_c \qquad ...(3.8)$$

where k_c is the pitch factor of the pick-up coil.

R_g is the air-gap reluctance.

Differentiating with respect to t and substituting into Eqn (3.7) yields,

$$v_k = \frac{F}{R_g} \cdot \frac{-1}{k} \cdot k_c kp_k \cdot \sin(\pm \omega t) \cdot (\pm \omega) \qquad ...(3.9)$$

Examining Eqn (3.9) reveals that for any harmonic k in the air-gap produced as a result of the winding distribution, the voltage it induces in a conductor will alternate with a frequency of ω or $2\pi f$ where f is the supply frequency of the exciting current. Since all harmonic induced voltages would be of the same frequency a spectral analysis of the voltage generated in the pick-up coil would not reveal the individual harmonic field effects. It may be possible to vary the pitch of the pick-up coil in an attempt to reduce the effects of all but one of the harmonics but even then most of the harmonics to some extent contribute to the generated voltage.

If the pick-up coil was rotated in synchronism with the main field no voltage would be induced by this field and the frequency of a forward rotating field with respect to the pick-up coil is reduced as illustrated in Fig. (3.7a). However the frequency of a backward rotating field with respect to the pick-up coil is increased, Fig (3.7b). Thus a forward rotating field of order k + 1 and a backward rotating field of order k - 1 have a frequency of k relative to the pick-up coil and so

induce a voltage of frequency k. Therefore it would still not be possible to separate the effects of individual harmonics.

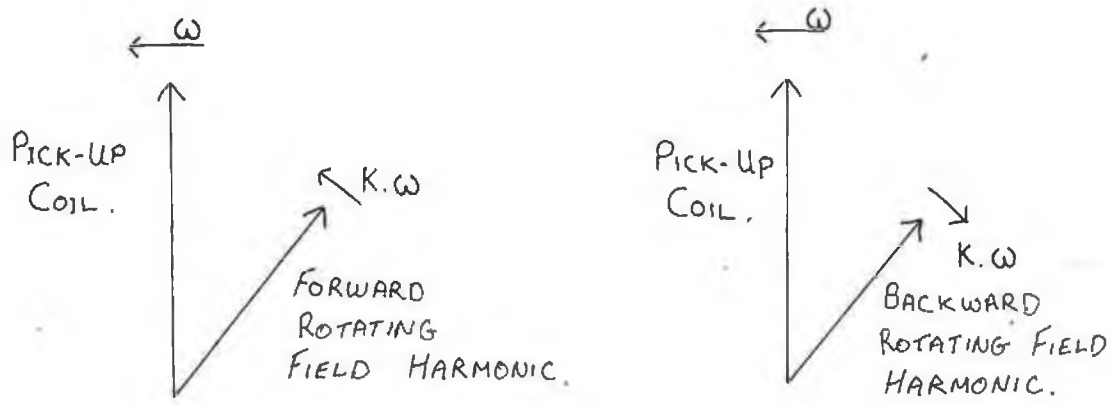

FIGS. (3.7a and 3.7b) Relative rotation of Pick-Up coil to Forward and Backward rotating Field Harmonics.

3.2.2 Experimental Method (2).

This consists of driving the motor as a generator and measuring the harmonic voltages induced in the stator windings. In this case the air-gap m.m.f. is produced by magnets mounted on the surface of the rotor. To use this method it is necessary to estimate the relative magnitudes of the fundamental and harmonic air-gap m.m.f.s produced by the rotor magnets. This analysis is outlined in Appendix (C). In Appendix (C) the rotor magnet m.m.f. is considered to be an approximately rectangular function as shown in Fig 3.8. The curved portion of the function is an attempt to cater for the grinding process on the surface of the magnets. The analysis also assumes that the m.m.f. produced by the magnets is directly proportional to magnet length across the magnet surface and that the direction of magnetic induction is everywhere parallel to the sides of the magnet.

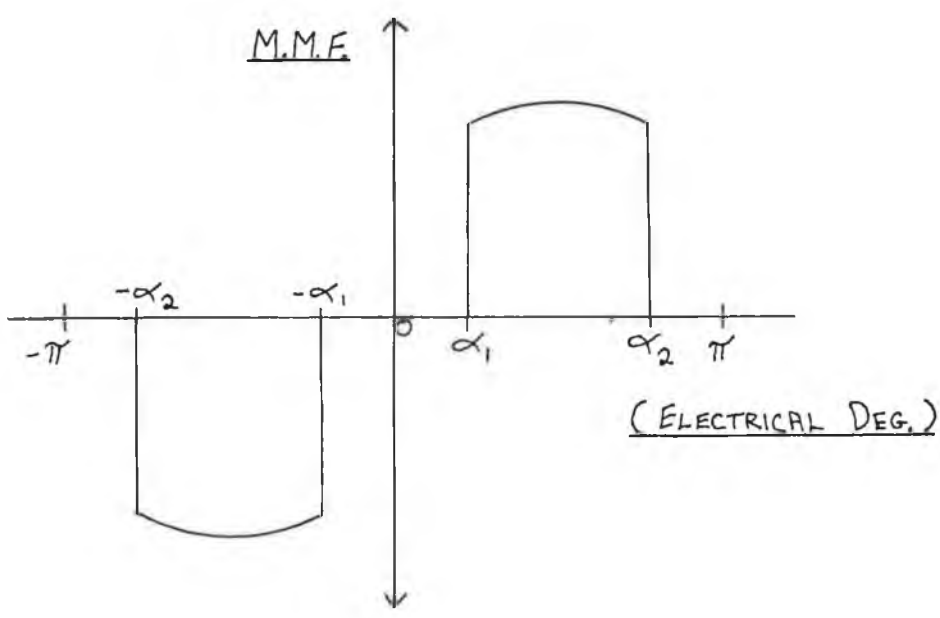

FIG. (3.8) Rotor Magnet m.m.f distribution over two Pole pitches.

In calculating the induced voltage due to the various harmonics a number of other assumptions were also made as follows,

1 The effects of slotting on air-gap reluctance could be ignored as the air-gap is large (Nd - Fe - B material has approximately the same magnetic permeability as air). The sum of the magnet length at the centre and the air-gap length is 4.34×10^{-3} m as opposed to a slot opening of 1.5×10^{-3} m.

2 The effect of leakage flux paths on the induced voltage is ignored.

3 The reluctance of the Iron on both sides of the air-gap is zero. From a simple consideration of the magnetic circuit, the flux density in the stator teeth is of the order of 1.5 to 1.6 Tesla and at this flux level the Iron reluctance might have some effect on " uniformity of the air-gap ".

3.2.3 Induced E.m.f. due to Rotor Field.

Because of the assumptions outlined the harmonic flux is directly proportional to it's causative m.m.f. at every point around the air-gap of the machine. In general the generated e.m.f. e_n due to a sinusoidally changing flux harmonic φ_n linking a single coil is given by,

$$e_n = [\ \sqrt{2} \cdot \pi \cdot f \cdot n \cdot \varphi_n \cdot kw_n\ ] \qquad ...(3.10)$$

where f is the frequency of the fundamental wave in Hz
n is the relative frequency of the harmonic wave
φ_n is the flux /pole due to the n^{th} harmonic

Consider two harmonics of flux of different orders as shown in Fig. (3.9), both harmonics having the same peak flux Φ_m. To calculate the flux /pole it is necessary to integrate the flux variation over one pole pitch for each of the harmonics,

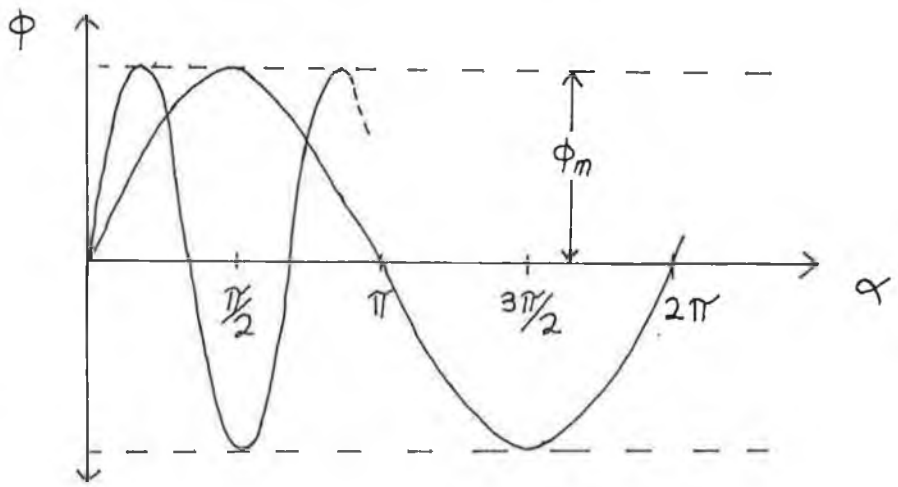

FIG. (3.9) Flux Harmonics of Different orders and the same peak value.

$$\int_0^{\pi} \Phi_m \sin(\theta).d\theta = 2\,\Phi_m \quad (\text{Wb})$$

$$\int_0^{\pi/3} \Phi_m.\sin(3\theta).d\theta = \frac{2}{3}\Phi_m \quad (\text{Wb})$$

In general therefore, the ratio of the harmonic generated e.m.f. to the fundamental e.m.f. when the harmonic flux frequency is n times the fundamental frequency is given by,

$$\frac{e_n}{e_1} = \frac{\Phi_n \text{ max } . \text{ kw}_n}{\Phi_1 \text{ max } . \text{ kw}_1} \qquad ...(3.11)$$

If the winding factors and flux maxima of the various harmonics are known the ratio of the generated voltages can be calculated. The various harmonic phase voltages generated by driving the Moog motor as a generator were calculated and are presented in Table (4). The generated voltages are expressed in dBv for ease of comparison with the test results presented later on. In addition to the winding factor, a slot factor K_{sn} [Refs. 14 & 15] is calculated for each harmonic to account for the fact that the slot openings are not negligible. This has the effect of reducing some of the higher harmonic induced voltages which is reasonable when it is considered that the phase difference between conductors in the same slot is not negligible in the case of the higher harmonics. K_{sn} is defined as follows,

$$K_{sn} = \frac{\sin(n.\Delta/2)}{n.\Delta/2} \qquad ...(3.12)$$

where Δ is the slot opening in radians

This factor may also be used to calculate the reduction in the m.m.f. harmonics produced by a distributed winding as a result of the slot openings. A factor similar to this is often used to account for the mechanical skewing of slots, usually by one slot pitch, to reduce slot harmonics. In that case Δ is the slot pitch in radians and the factor is called the skew factor [Ref. 15].

TABLE (4)

Generated Harmonic Phase Voltages (calculated)

Harmonic Order	Field Harmonic Magnitude	Winding Factor $K_p.K_d$	Induced Voltage dBv
1	100.0	0.9471	0.00
2	-	-	-
3	0.597	0.5910	-48.92
4	-	-	-
5	-16.83	0.1590	-32.03
6	-	-	-
7	-14.05	0.0855	-40.08
8	-	-	-
9	-2.99	0.0935	-54.32
10	-	-	-
11	6.19	0.0303	-59.97
12	-	-	-
13	7.91	0.0000	-
14	-	-	-
15	3.10	0.0303	-73.59
16	-	-	-
17	-3.01	0.0935	-72.73
18	-	-	-
19	-5.95	0.0855	-74.37
20	-	-	-
21	-3.04	0.1590	-64.00
22	-	-	-
23	1.41	0.5910	-55.85
24	-	-	-
25	3.99	0.9471	-41.90
26	-	-	-
27	2.90	0.9471	-44.05
28	-	-	-
29	-0.44	0.5910	-65.41

3.2.4 Test Set-Up.

The physical arrangement used to carry out actual measurements on the motor is illustrated in Fig. (3.10). The generator was used to feed a balanced three phase resistive load connected in Star as shown. This was necessary to gain access to an individual phase voltage as the standard Moog motor does not have a "neutral lead from the internal star point connection. Unfortunately this arrangement is not ideal since the motor windings are not perfectly balanced and this may lead to some discrepancy between the actual phase generated harmonics and the measured harmonics across the load resistors. This may be appreciated by referring to Appendix (D).

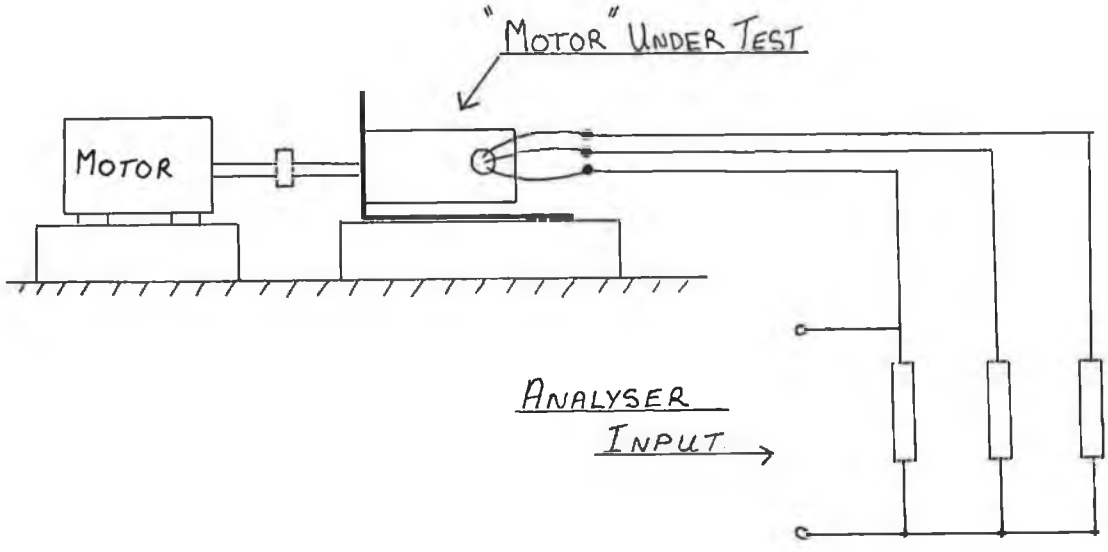

FIG. (3.10] Experimental Test Set-up to verify Winding analysis.

The probes of a spectrum analyiser were connected across one of the load resistors and the individual harmonic voltages were measured and are presented in Plot (3.1). This plot compares measured and calculated harmonic voltage values and a reference voltage level of 0 dBv is assigned to the fundamental voltage magnitude. The measured harmonic values are connected by lines to facilitate easy distinction between the two data sets.

On inspection of this plot it is seen that some discrepancies arise between calculated and measured data particularly in the case of the third harmonic which at -34 dBv is significantly larger than had been predicted, -49 dBv. In the case of the 13^{th} voltage harmonic, the predicted magnitude was zero. However the measured 13^{th} harmonic voltage is of the order of -68.0 dBv or approximately 0.04% of the fundamental induced voltage.

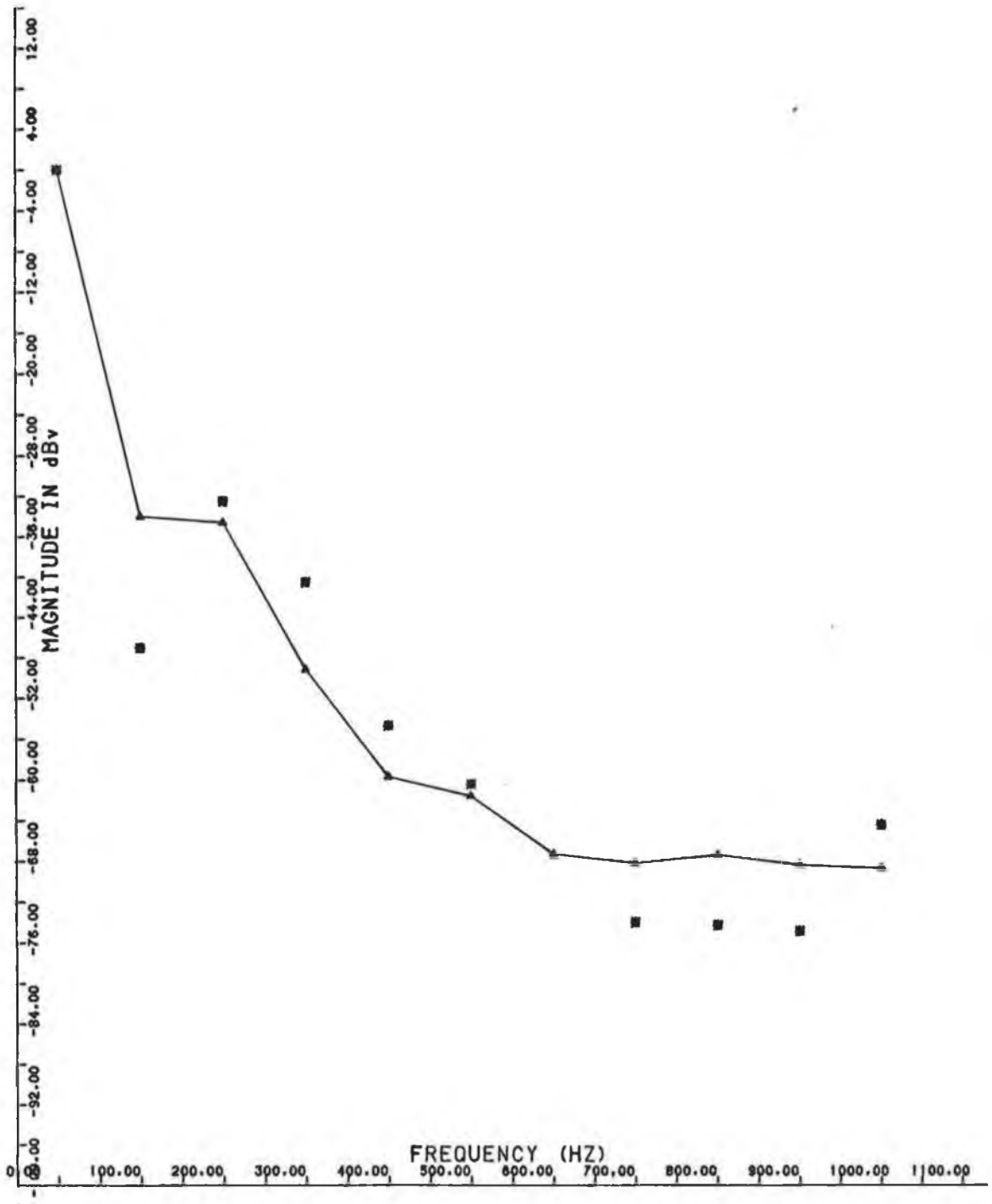

Plot (3.1) Comparison of Calculated and Measured Induced Harmonic Voltages for a 39 slot, 12 Pole, 3 phase P.M. motor driven as a Generator.

After considering the assumptions made in this analysis, an attempt to take account of the air-gap permeance variation seemed a logical step. This consisted of obtaining a Fourier series representation of the inverse of the motor air-gap since the permeance of a flux path is proportional to the inverse of the path length. Refer to Appendix (E) for details of this analysis applied both to the rotor and stator slot effects.

3.3 CALCULATION OF THE INDUCED VOLTAGE HARMONICS TAKING ACCOUNT OF AIR-GAP NON-UNIFORMITY.

3.3.1 Rotor slot effects.

From the analysis carried out in Appendix (E) it is clear that the assumption of uniform air-gap permeance is not correct and harmonic variations of up to 11.6% of the constant permeance term were calculated. Since the rotor has twelve periods of air-gap variation in total the order of the permeance harmonics are doubled with respect to the fundamental magnet m.m.f. harmonic. Table (5) presents the magnet m.m.f and rotor permeance harmonics in terms of the magnet fundamental order.

Table (5)

Magnitude of Magnet Harmonic M.m.f.s
and Rotor Permeance Harmonics

Harmonic Order	Magnet Harmonics	Rotor Permeance Harmonics
0	-	100.0
1	100.0	-
2	-	11.6
3	0.79	-
4	-	8.6
5	-16.87	-
6	-	4.54
7	-14.13	-
8	-	-
9	-3.0	-
10	-	-1.84
11	6.21	-
12	-	-2.76
13	7.96	-
14	-	-2.20
15	3.10	-
16	-	-
17	-3.00	-
18	-	-
19	-5.50	-
20	-	1.55
21	-3.06	-

Previously the air-gap permeance was considered to be uniform and the flux was directly proportional to the m.m.f. acting across the air gap at all points. Taking account of the rotor slots leads to the following general expression for the air-gap permeance,

$$P_{air\text{-}gap} = P_0 + \Sigma P_n.\cos(n\theta_e) \qquad \ldots(3.13)$$

where P_0 is the constant permeance term.

P_n are various permeance harmonic terms as shown in Table (5).

θ_e is the electrical angle which by virtue of the machine having twelve poles is six times the mechanical angle taken around the air-gap periphery.

Consider the interaction of the magnet m.m.f. fundamental and the air-gap permeance as defined in equation (3.13),

$$\Phi_g = F_1\cos\theta_e.[\ P_0 + \Sigma\ P_n.\cos(n\theta_e)\ ]$$

$$= F_1P_0\cos\theta_e + \Sigma\ (\ F_1P_n.\cos\theta_e.\cos(n\theta_e)\ )$$

$$= F_1P_0\cos\theta_e + \Sigma\ (\ \frac{F_1P_0}{2}.[\cos(n\theta_e + \theta_e) + \cos(n\theta_e - \theta_e)]\ )$$

... (3.14)

On inspection of equation (3.14) it is seen that in addition to the fundamental flux term, two additional harmonic terms of order $n\theta_e + \theta_e$ and $n\theta_e - \theta_e$ occur for each permeance harmonic term. These harmonic fluxes rotate in synchronism with the rotor and induce additional harmonic voltages in the stator windings when the motor is driven as a generator. As an example consider the third harmonic induced voltage which has the following main flux components,

M.m.f. Harmonic Order	Permeance Harmonic Order	Induced voltage Component magnitude
3	0	7.9×10^{-3}
1	2	5.8×10^{-2}
1	4	4.3×10^{-2}
5	2	-9.8×10^{-3}
7	4	-6.1×10^{-3}

The magnitudes of the components are normalised to a base where the interaction of the fundamental m.m.f. and the constant permeance term P_0 produces the unit flux term. If the induced voltage components arising from the interaction of the major rotor permeance and m.m.f. harmonics are considered, and the results compared with measured data, better agreement between the two sets of results is evident Plot (3.2).

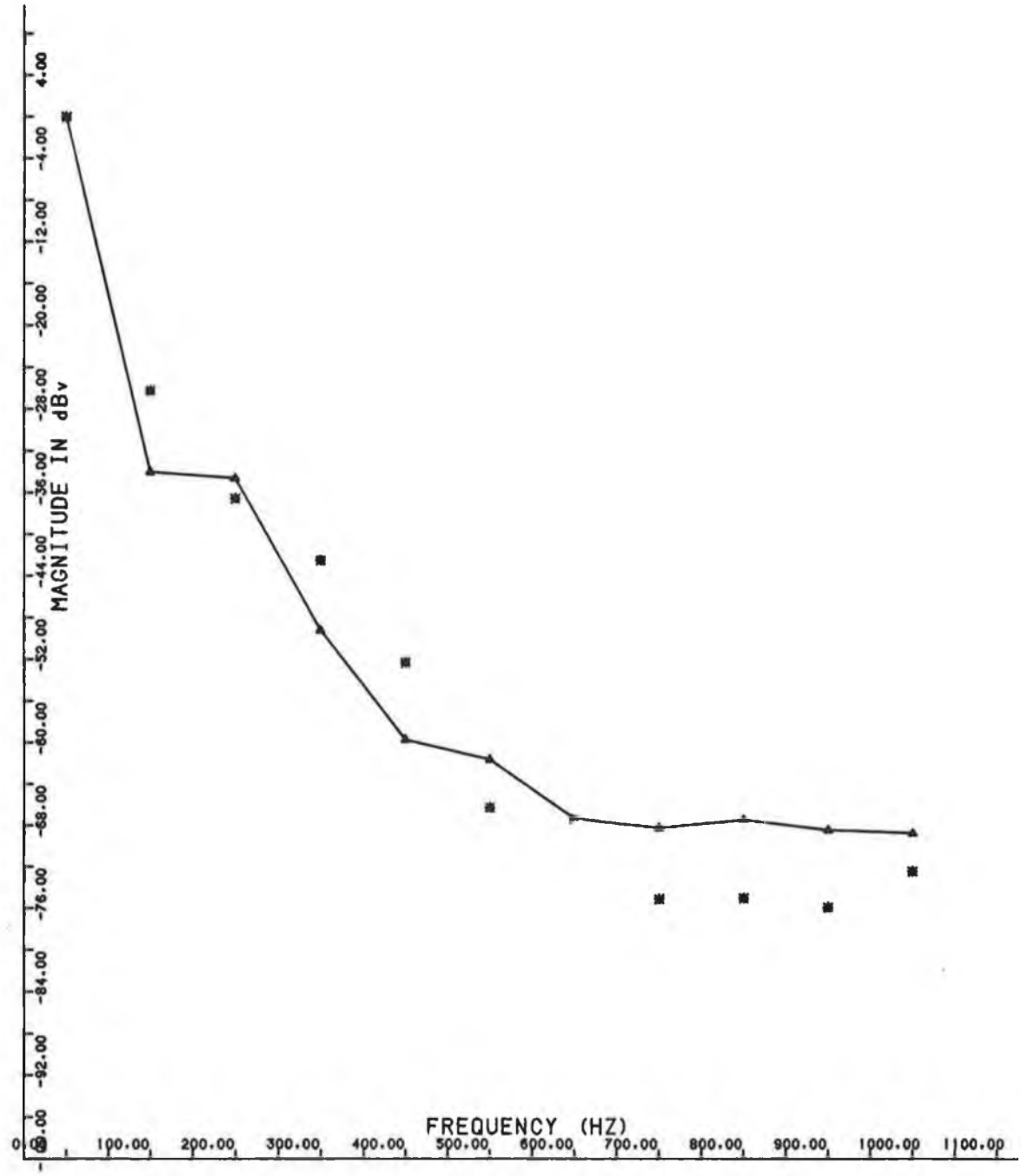

Plot (3.2) Comparison of Calculated and Measured Induced Harmonic Voltages for a 39 slot, 12 Pole, 3 phase P.M. motor driven as a Generator.

3.3.2 Stator slot effects.

The air-gap permeance harmonics arising as a result of the stator slotting are shown in Table (2) of Appendix (E). Because of the arbitary manner in which the air-gap permeance was approximated it is probable that the actual magnitudes of the harmonics are quite different to those presented in the table. However, the order of the harmonics are correct and as such the additional flux harmonics present in the air-gap as a result of the stator slots can be predicted. The use of finite element analysis or flux plotting plotting techniques would be required to determine the stator slot permeance variation more accurately. Combining the two sets of permeance harmonics results in the following expression for the complete air-gap permeance [Ref. 10],

$$P_{air\text{-}gap} = [\ P_0 + \Sigma\ P_n \cos(n\theta_e)\ ]\ .\ [\ 1 + \Sigma\ P_m \cos.ms(\theta_e+wt)\ ]$$

$$= P_0 + \Sigma\ P_n \cos(n\theta_e) + \Sigma\ P_m \cos.ms(\theta_e+wt)$$

$$+ \Sigma\Sigma\ P_nP_m \cos(n\theta_e).\cos.ms(\theta_e+wt)$$

...(3.15)

where P_m are the harmonic permeance terms due to the presence of the stator slots, the order of which are given in terms of the primary twelve pole field.

s = 39/6 since the stator has 39 slots and the fundamental magnet m.m.f. has six cycles of variation around the air-gap.

Example

As an example of the effect of the stator and rotor slot permeance harmonics consider the Moog series 304 motor with 39 stator slots. The interaction of a rotating m.m.f. wave of order n with an air-gap permeance function similar to that given in equation (3.15) except that the number of stator slots is 39 gives,

$$\Phi_g = A_n\cos\ n(6\theta - wt).P_0.\ \left[\begin{array}{l} 1 + P_{rm}.P_{sp}.\cos(39p\theta).\cos(12m(\theta-wt/6)) \\ + P_{sp}\cos(39p\theta) + P_{rm}\cos(12m(\theta-wt/6)) \end{array}\right]$$

$$
\begin{aligned}
= \quad & P_0.A_n \cos(6n\theta - nwt) \\
& + A_n/4.P_0.P_{rm}.P_{sp} \left[\begin{array}{l} \cos(6n\theta + 39p\theta + 12m\theta - nwt - 2mwt) \\ + \cos(6n\theta - 39p\theta - 12m\theta - nwt + 2mwt) \\ + \cos(6n\theta + 39p\theta - 12m\theta - nwt + 2mwt) \\ + \cos(6n\theta - 39p\theta + 12m\theta - nwt - 2mwt) \end{array} \right] \\
& + A_n/2.P_0.P_{sp} \left[\cos((6n + 39p)\theta - nwt) + \cos((6n - 39p)\theta - nwt) \right] \\
& + A_n/2.P_0.P_{rm} \left[\cos((6n + 12m)\theta - (n + 2m)wt) + \cos((6n - 12m)\theta - (n - 2m)wt) \right]
\end{aligned}
$$

...(3.16)

where θ is the angle measured in mechanical degrees.

A_n is a coefficient representing the relative magnitude of the m.m.f. wave.

P_{sp}, P_{rm} are the stator and rotor permeance harmonics of order p and m respectively. In each case the order of the harmonics are given in terms of the fundamental slot permeance variation.

From equation (3.16) it is evident that the resultant flux is made up of four different components namely,

(1) A constant rotating flux term of order n rotating at the same speed as the m.m.f. wave, due to the P_0 permeance term.

(2) Multiple flux terms of different harmonic orders rotating at different speeds to the m.m.f. wave due to the interaction of all three permeance terms.

(3) Stator permeance flux terms of different harmonic orders to the m.m.f. wave rotating in opposite directions around the air-gap.

(4) Rotor permeance flux terms of different harmonic orders to the m.m.f. wave rotating in opposite directions around the air-gap.

Each of these rotating flux waves will induce an alternating voltage in the stationary coils of the stator winding. The magnitude of the voltage will depend on the corresponding harmonic winding factor of the winding, the magnitude of the flux per pole and the rate of change of the flux per pole as before. The frequency of the induced voltage on the other hand depends on the rate of change of the flux per pole only, which is a function of the harmonic order and speed of the flux wave.

All the induced voltage terms including those due to the stator slotting could be considered when predicting the induced voltage in the stator windings. However the actual stator permeance terms are likely to be inaccurate due to the arbitary way in which the stator slot permeances were approximated. Therefore calculation of the induced voltage terms due to the stator slots was not carried out.

3.4 DISCUSSION.

In this chapter a method of winding m.m.f. analysis was described and was applied to three different winding configurations with 36, 39 and 45 slots. The 39 slot winding arrangements is presently used in Moog servo-motors and the other two were considered as possible alternatives to it. From the results it is seen that both the 39 and 45 slot configurations produce significant m.m.f. sub-harmonics whereas the 36 slot layout gives rise to large higher order harmonics. The choice of winding arrangement depends to a large extent on its interaction with the rotor field to produce motor torque. This will be dealt with in the next chapter.

In order to validate this method of analysis an experimental procedure was carried out which allowed the individual induced harmonic voltages to be measured. Initially the effect of slotting was ignored and there was reasonable correlation between calculated and measured data. When account was taken of the rotor lugs using the idea of permeance harmonics better correlation was obtained particularly in the case of the third harmonic.

Because the 13^{th} harmonic winding factor is zero, no 13^{th} harmonic induced voltage was expected. However it is possible that this harmonic is present due to slight asymmetry in the location of the Stator conductors resulting in a non-zero winding factor. Alternatively the interaction of Stator slot permeances with the Rotor field could produce Air-gap flux harmonics which are not of order 13 but which induce harmonic voltages of this order by virtue of their rotation velocity. This can be appreciated by referring to equation (3.16).

No attempt to take account of the stator slot effects was made because of the difficulty of determining the tooth and slot permeances. If the method of finite element analysis was used to estimate the air-gap permeance variations it is likely that better agreement between measured and calculated data could be achieved. In any event quite good correlation between the two sets of data was obtained indicating that this method of winding analysis is of practical use for motor design.

Chapter 4.

ESTIMATION OF MOTOR REACTANCES AND DERIVATION OF MOTOR TORQUE EQUATION.

4.1 ESTIMATION OF MOTOR REACTANCES.

4.1.1 Magnetising Reactance of Uniform Air-gap Motor.

In general, the magnetising reactance X_m for a round rotor polyphase motor is given by [Ref. 10],

$$X_m = \frac{\mu_0.q.(N.kp.kd)^2.D.L.2.\pi.f}{\pi.P^2.g} \quad \text{(Ohms)} \qquad \ldots (4.1)$$

where, μ_0 is the permeability of free space. $(4.\pi.10^{-7})$.
q is the number of phases.
N is the number of turns per phase.
kp is the pitch factor of the winding.
kd is the distribution factor of the winding.
D is the average diameter of the air-gap.
L is the stack length of the motor.
P is the number of pole pairs in the motor.
g is the air-gap length.

In the case of the motor being studied however, the air-gap is not uniform due to the presence of surface mounted magnets of low permeability in the direct axis of the machine and steel lugs of relatively high permeability in the quadrature axis, as shown in Fig. (4.1). This non-uniformity gives rise to a reluctance torque by virtue of the fact that the direct and quadrature axis magnetising reactances X_d and X_q, are not equal in Equation (4.2) [Refs. 13 and 17].

$$T = \frac{m.V.E_f.\sin\delta}{\omega.(X_d + X_a)} + \frac{(X_d - X_q).m.V^2.\sin 2\delta}{(X_d + Xa).(Xq + Xa).2\omega} \quad (Nm)$$

...(4.2)

where, T is the motor torque.

m is the number of phases.

ω is the frequency of the applied voltage.

V is the magnitude of the applied voltage.

E_f is the back e.m.f. of the machine.

δ is the load angle of the machine.

X_d is the direct axis magnetising reactance.

X_q is the quadrature axis magnetising reactance.

Xa is the leakage reactance.

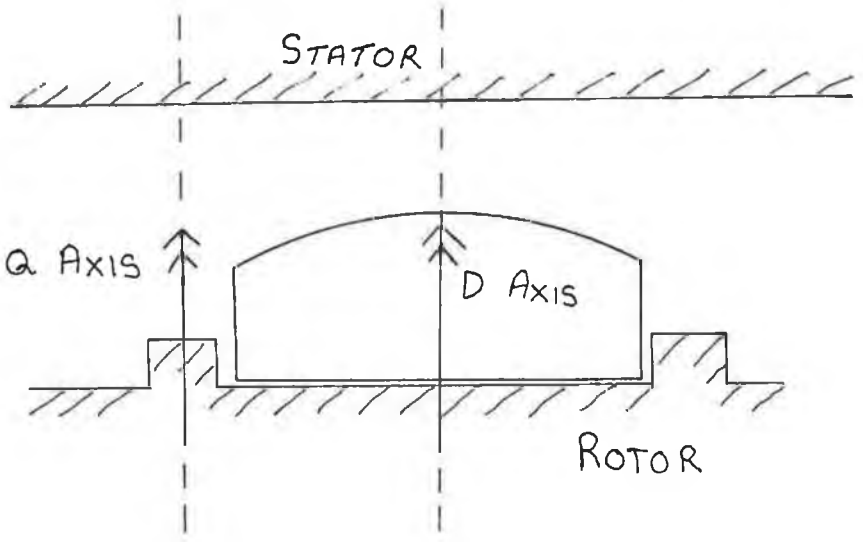

Fig. (4.1) Air-Gap Profile of a P.M. motor with surface mounted magnets.

It is only the second term of equation (4.2) which is dependent on the relative magnitudes of X_d and X_q and this term is called the reluctance torque component. Since the motor controller is intended to produce the maximum output torque per amp supplied, it is necessary to estimate the relative magnitudes of the two torque components. This necessitates the calculation of the direct and quadrature reactances.

4.1.2 Calculation of Direct Axis Magnetising Reeactance.

Consider the air-gap profile of the motor in the direct axis as shown in Fig. (4.2). The permeability of the magnet is approximately equal to that of air while that of the steel lugs is assumed to be infinite resulting in the step function g(θ), with two values, g' and g" as shown.

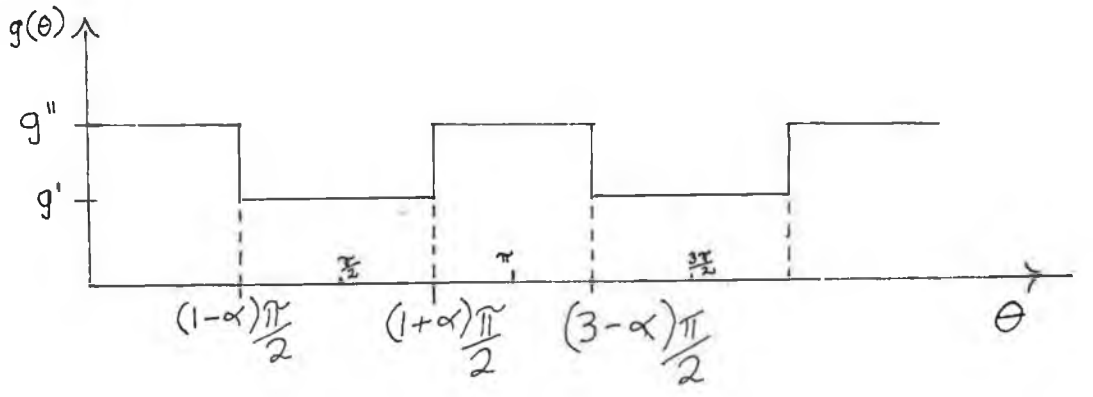

Fig. (4.2) Air-Gap Profile in Direct Axis of P.M. motor with surface mounted magnets.

The peak value of the fundamental m.m.f. wave of a 2P pole, m phase winding is given by, [Ref. 10],

$$A = \frac{\sqrt{2}.m.N.I.kp.kd}{\pi.P} \quad \text{(Amp/pole)} \qquad ...(4.3)$$

where A is the peak ampere turns per pole.
m is the number of phases.
I is the r.m.s. current.

Consider a moment in time such that the peak m.m.f. occurs at $\theta = \pi$ electrical radians in Fig. (4.2) and let $A(\theta)$ represent the variation with θ, of the m.m.f.

acting across the air-gap. The air-gap flux density Bg(θ) corresponding to this instance in time is,

$$Bg(\theta) = \frac{-\mu_0 \sqrt{2}.m.N.I.kp.kd.\cos\theta}{\pi.P.g(\theta)}$$

$$= \frac{-K.\cos\theta}{g(\theta)}$$

...(4.4)

Bg(θ) is illustrated in Fig. (4.3) for the range π/2 to 3π/2.

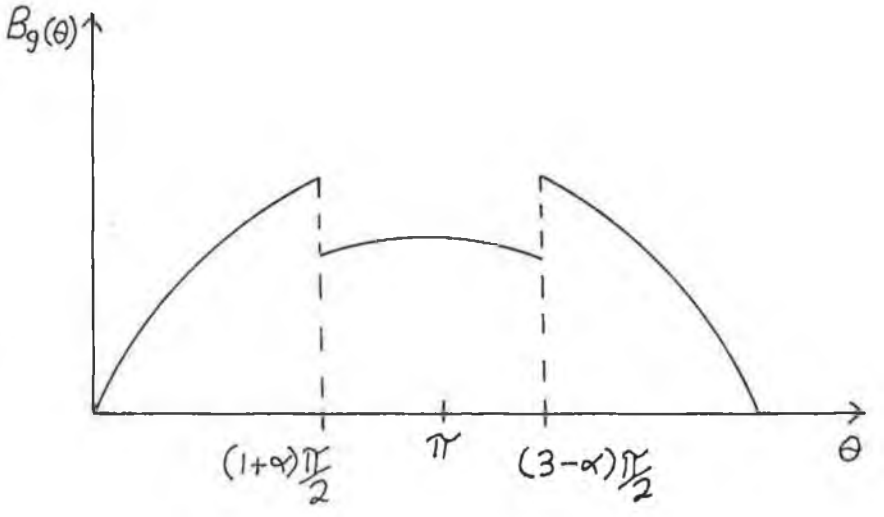

Fig. (4.3) Air-Gap Flux Density in the direct axis of a P.M. motor with surface mounted magnets.

The function Bg(θ) is an even function and is also symmetric about the θ axis. Applying Fourier Series to the function, the fundamental component $Bg_1(\theta)$ is given by,

$$Bg_1(\theta) = \frac{2}{\pi}\int_{\pi/2}^{3\pi/2} Bg(\theta).\cos\theta.d\theta$$

$$= \frac{-K.4}{\pi} \int_{\pi/2}^{(1+\alpha)\pi/2} \frac{\cos^2\theta.d\theta}{g(\theta)}$$

...(4.5)

It can be shown that,

$$\int_{\pi/2}^{(1+\alpha)\pi/2} \frac{\cos^2\theta.d\theta}{g(\theta)} = \frac{\pi}{4g'} \left[\left[\alpha - \frac{\sin\alpha\pi}{\pi}\right] + \frac{g'}{g''} \left[1 - \alpha + \frac{\sin\alpha\pi}{\pi}\right] \right]$$

...(4.6)

Thus equation (4.5) can be rewritten as,

$$Bg_1(\theta) = \frac{-K}{g'} \left[\left[\alpha - \frac{\sin\alpha\pi}{\pi}\right] + \frac{g'}{g''} \left[1 - \alpha + \frac{\sin\alpha\pi}{\pi}\right] \right]$$

$$= \frac{-K}{g'}.A_0$$

...(4.7)

The term A_0 in equation (4.7) represents the effect of the air-gap variations on the fundamental flux density $Bg_1(\theta)$. The total fundamental flux per pole φ_1 due to the fundamental exciting m.m.f. is given by,

$$\varphi_1 = \frac{2}{\pi} Bg_1 \left[\frac{\pi DL}{2P}\right] = Bg_1 \frac{DL}{P}$$

...(4.8)

Substituting equation (4.8) into equation (4.7) and solving for I (rms current) yields,

$$I = \frac{-\varphi_1.P^2.g'}{\mu_0.\sqrt{2}.q.N.kp.kd.A_0.D.L}$$

...(4.9)

I is the rms magnetising current required to produce the desired fundamental flux φ_1 per pole. Now, the fundamental induced voltage per phase E_1, is given by [Ref. 13],

$$E_1 = \sqrt{2}.\pi.kp.kd.N.\varphi_1.f \qquad \ldots(4.10)$$

The direct axis magnetising reactance per phase is thus given by,

$$X_d = \frac{E_1}{I\,rms} = \frac{\mu_0.2.q.f.(N.kp.kd)^2.DL.A_0}{P^2.g'} \qquad \ldots(4.11)$$

Equation (4.11) is identical to equation (4.1) except for the factor A_0 as would be expected since A_0 is equal to unity if g' and g" are equal, i.e. a uniform air-gap motor.

4.1.3 Calculation of Quadrature Axis Magnetising Reactance.

The calculation of the quadrature axis magnetising reactance is similar to that carried out for the Direct axis magnetising reactance except that the gap function $g(\theta)$ is changed as illustrated in figure (4.4).

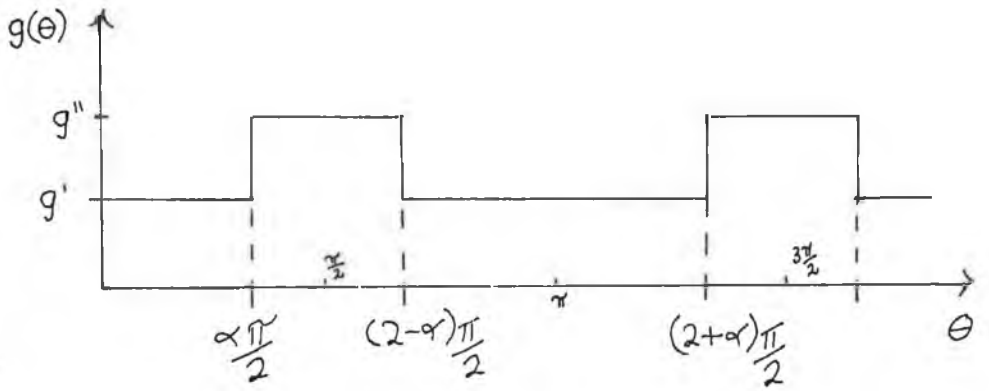

Fig (4.4) Air-Gap Profile in the Quadrature Axis of a P.M. motor with surface mounted magnets.

The fundamental air-gap flux density in this case is given by,

$$Bg_1 = \frac{-K}{g'}\left[\left[\alpha + \frac{\sin\alpha\pi}{\pi}\right] + \frac{g'}{g''}\left[1 - \alpha - \frac{\sin\alpha\pi}{\pi}\right]\right]$$

$$= \frac{-K}{g'}.B_0$$

...(4.13)

The quadrature magnetising reactance X_q can now be derived in a similar fashion to X_d yielding,

$$X_q = \frac{\mu_0.2.q.f.(N.kp.kd)^2.D.L.B_0}{P^2.g'}$$

...(4.14)

4.1.4 Slot Leakage Reactance of a Single Coil.

Consider a slot containing a current carrying coil as illustrated in figure (4.5).

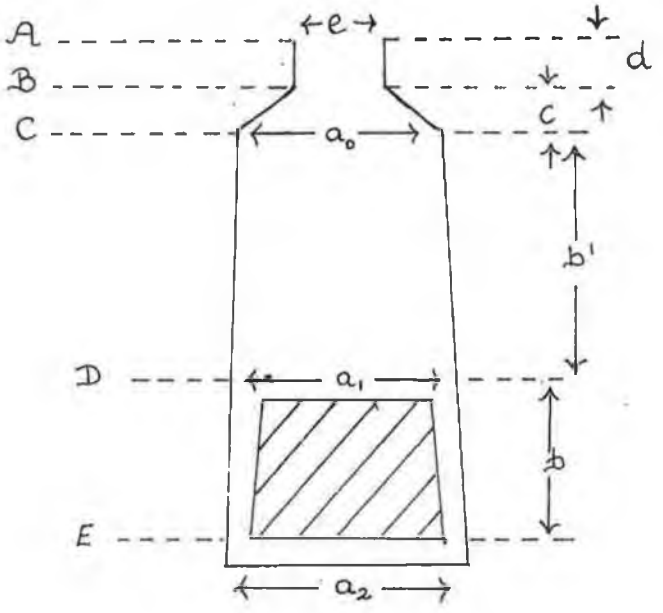

Fig. (4.5) Stator slot with current carrying Coil.

The method used to calculate the slot leakage reactance is based on the methods outlined in references [10] and [16]. These methods assume that the leakage flux flows in straight lines across the slot and that the permeability of the iron is infinite. The reactance of any portion of the slot is given by the following equation,

$$X = \frac{2.\pi.f.N.\varphi_p}{I} \qquad \ldots(4.15)$$

where N is the number of turns in the slot.
φ_p is the flux linking the N turns in the portion of the slot under consideration.
I is the current flowing in each turn.

Consider the portion A-B of the slot in figure (4.5). The flux density B_{A-B} in this portion is given by,

$$B_{A-B} = \frac{\mu_0.N.}{e} \quad \text{Tesla.} \qquad \ldots(4.16)$$

Consequently, the flux in the slot portion A-B is,

$$\varphi_{A-B} = B_{A-B}.d.l \quad \text{webers.} \qquad \ldots(4.17)$$

where e is the slot opening
l is the length of the slot.
d is the depth of the slot portion.

Substituting into equation 4.15 yields,

$$X_{A-B} = 2.\pi.f.N^2.\mu_0.l.\left[\frac{d}{e}\right] \qquad \ldots(4.18)$$

The factor (d/e) is known as the slot constant for that portion of the slot and is the specific permeance per unit length of slot for the slot portion A-B. The reactances of portions B-C and C-D are calculated in a similar manner to portion A-B and are found to be,

$$X_{B-C} = 2.\pi.f.N^2.\mu_0.l.\left[\frac{2.c}{e+a_0}\right] \qquad \ldots(4.19)$$

$$X_{C-D} = 2.\pi.f.N^2.\mu_0.l.\left[\frac{2.b'}{a_0+a_1}\right] \qquad \ldots(4.20)$$

The calculation of the reactance of the slot portion D-E is a little more involved [Ref. 16], as the flux in that portion of the slot does not link all of the conductors. However it is shown in Ref. [16] that,

$$X_{D-E} = 2.\pi.f.N^2.\mu_0.l.K_s \qquad \ldots(4.21)$$

where the slot constant K_s is given by,

$$K_s = \frac{b}{a_2}\,\frac{1}{(y+1)^2}\left[\frac{y+3}{4} + \frac{1}{2(y-1)} - \frac{1}{(y-1)^2} + \frac{\log y}{(y-1)^3}\right]$$

$$\text{where } y = \frac{a_1}{a_2}$$

4.1.5 Slot Leakage Reactance of a Complete Winding.

Previously the reactance of a single slot was derived for the case where all the current in a slot was in time phase. However, on inspection of the winding in the Moog motor , it is seen that nine of the 39 slots are shared between two phases. Thus it is important to consider how this affects the overall winding reactance. This situation arises due to the fact that the winding is not full pitched. Consider

a slot as illustrated in figure 4.6 containing two distinct bundles of conductors separated by a negligible gap d_2.

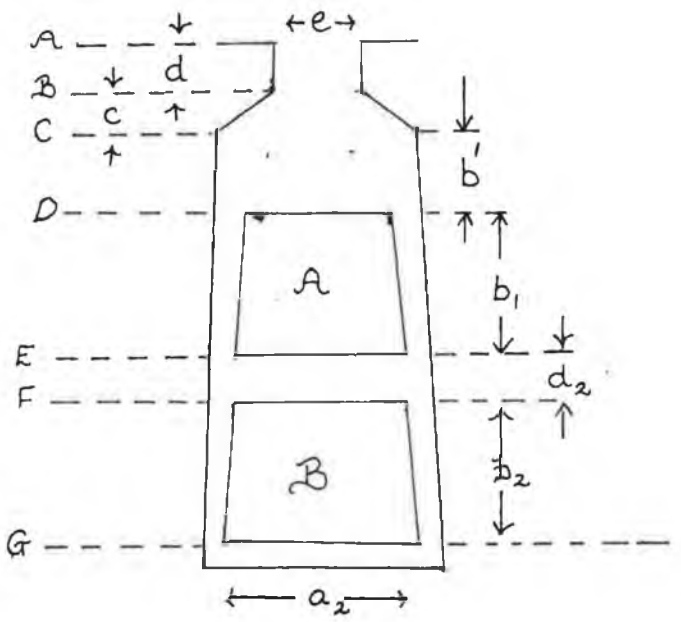

Fig. (4.6) Stator slot with two Coils carrying out of phase currents.

Let N be equal to the number of conductors in windings A and B.
In this case the total slot reactance is made up of three parts namely,

(1) X_A, the self leakage reactance of A.
(2) X_B, the self leakage reactance of B.
(3) X_C, the mutual reactance of A and B.

If the currents in A and B differ by an electrical time angle of θ, then the mutual coupling between the two conductor bundles will give rise to an in-phase induced voltage component and an out-of-phase induced voltage component in one bundle as a result of current flowing in the other bundle. If the whole winding is taken however, the out of phase voltage components cancel and it is only the in-phase components that need to be considered. The total slot reactance is therefore given by [Ref. 10],

$$X_{tot} = X_A + X_B + 2.X_{AB}.\cos\theta \qquad \ldots(4.22)$$

where for a paralell sided slot,

$$X_{AB} = \frac{d}{e} + \frac{2.c}{e+a_0} + \frac{2.b'}{a_0+a_1} + \frac{b - d_2}{.4.w}$$

4.1.6 Peripheral Air-gap Leakage Reactance.

When calculating the magnetising reactance it was assumed that the flux path in the air-gap was radial. However a certain component of flux exists in a peripheral direction entirely within the air-gap, due to the m.m.f. between adjacent poles. It is shown in reference [10] that this leakage flux gives rise to a leakage reactance X_p given by,

$$X_p = X_m . \frac{2.P^2.g^2}{D^2} \qquad \ldots(4.23)$$

where X_m is the magnetising reactance.
P is the number of pole pairs.
g is the air-gap.
D is the internal stator diameter.

In normal induction machines, this reactance is negligible because of the small air-gap and number of pole pairs. However in the case of the servo-motor being studied, X_p is not insignificant (approximately 0.5 times X_m) and cannot be ignored.

4.1.6 End Turn Leakage Reactance.

This reactance component is particularly difficult to determine accurately since the flux due to the coil current is three dimensional in nature and is dependent on the geometry and compactness of the end coils. Many of the formulas used to determine this reactance are empirical in nature [Refs. 13, 16, 11 and 17]. In reference [10], the author assumes diamond shaped end windings and that all the flux paths are entirely in air. The current is then divided up into two components, an axially directed current component and a peripherally directed current component and the flux linkage and reactance associated with the two current components are

estimated, refer to Figure (4.7).

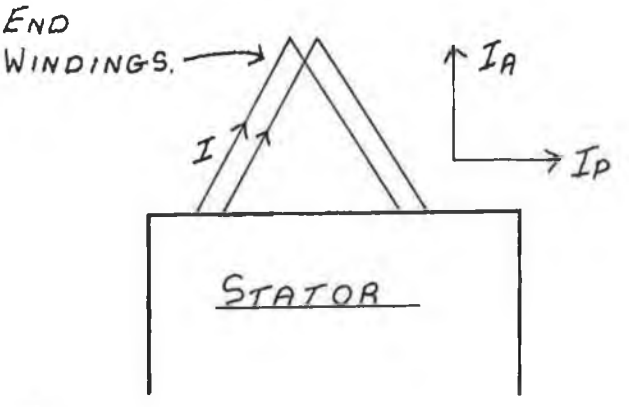

I_a is the axial component of current.
I_p is the peripheral component of current.

Fig. (4.7) End Turn Windings of a Stator with Axial and Peripheral current components.

The axial end turn reactance component X_{ea} is added to the peripheral end turn reactance component to give the total end turn reactance X_e as,

$$X_e = K.\left[19.72 \tan\alpha \left[\frac{p\pi - \sin p\pi}{\pi} \right] + 7.99\ kp^2 \left[\ln \frac{4D_1}{r_1} - 1.75 \right] \right]$$

$$\text{with } K = \frac{D_1 . f . q . N^2 . kd^2}{p^2 . 10^{-7}}$$

... (4.24)

where D_1 is the mean diameter of the end coils,
f is the supply frequency,
q is the number of phases,
p is the winding pitch,
r_1 is half the slot depth.

This formula is unlikely to give accurate values for the end turn reactance but in the absence of a finite element analysis package a more accurate analysis is unlikely to be found.

4.1.8 Discussion.

The foregoing are the various elements of reactance considered when evaluating the winding reactance of the motor being studied. The neglect of saturation and harmonic effects affect the overall accuracy of the equations. However saturation would have the effect of reducing the reactance of the windings whereas the air-gap harmonics would tend to increase the reactance of the windings by an amount equal to the so called differential leakage reactance and these effects will tend to oppose each other. Four separate measurements of the line to line inductance of the motor were taken as follows,

(1) Inductance of the motor with a cylindrical iron rotor in the air-gap was found to be 4.84 mH.

(2) Inductance of the motor with the production rotor and no magnets in the air-gap was 4.86 mH

(3) Inductance of the motor with standard rotor and magnets in the air-gap varied between 3.0 mH and 4.0 mH. This variation with rotor position is most likely a function of saturation in the magnetic circuits of the motor due to the magnet flux.

(4) Inductance of the stator with no rotor in the air-gap was approximately 4.54 mH.

It is is interesting to note that the Inductance of the stator without any rotor in the air-gap is greater than the Inductance of the stator and rotor complete with magnets. This would suggest that the saturation level in the magnetic circuit has a significant effect on the stator Inductance. If the Reactance of the motor is calculated using the formulae outlined it is found to be approximately 4:3 mH. While the accuracy of the calculated value is not good nevertheless all important dimensions are catered for in these formulae. Improved correlation between measured and estimated data would be obtained if a finite element analysis package were used in the estimation of flux linkages of the motor coils since this would account for saturation in the motor [Refs. 18 and 19].

4.2 Derivation of P.M. Motor Torque Equation.

4.2.1 Synchronous Motor Torque Equation.

The steady state torque produced in a synchronous motor is given by [Refs. 13 and 17],

$$T = \frac{-m.V^2}{\omega(X_d + X_a)} \left[\frac{E_f}{V} \sin\delta + \frac{X_d - X_q}{Xa + Xq} \sin 2\delta \right]$$

...(4.25)

where V is the applied e.m.f.

E_f is the open circuit back e.m.f.

This expression is given in terms of the motor's terminal characteristics neglecting stator resistance and air-gap harmonics due to the distribution of the windings and the shape of the surface mounted magnets. The corresponding phasor diagram of the motor is shown in figure 4.8, operating with a leading power factor.

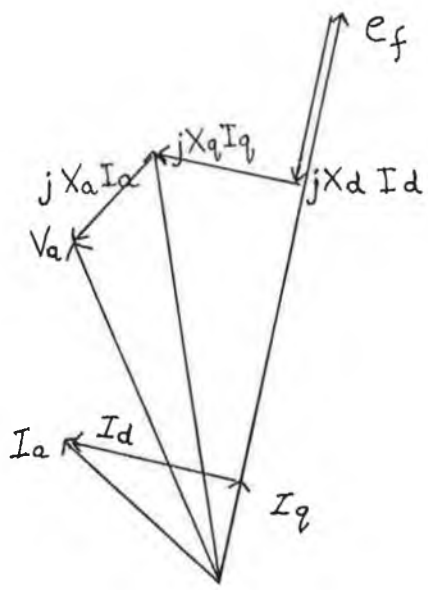

Fig. (4.8) Phasor diagram of a Synchronous motor operating with a leading Power Factor.

As previously mentioned, the torque consists of two components, a field and a reluctance component varying with the functions sinδ and sin2δ respectively. Figure (4.9) is a plot of these components and their resultant for various values of δ, assuming $X_d < X_q$ as is the case for the motor under consideration.

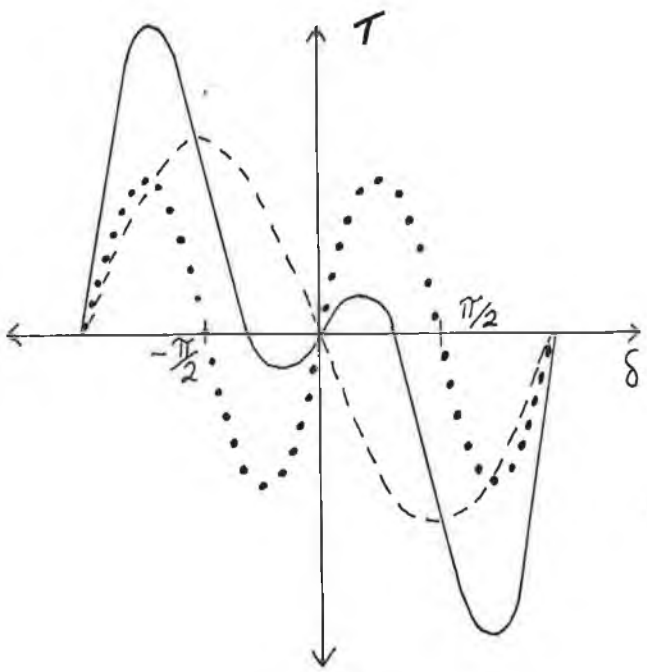

Fig. (4.9) Reluctance and Field Torque components of a P.M. motor with X_d less than X_q.

There is a value of δ other than 0 or -π for which the resultant motor torque is zero as shown in fig. 4.9 and this value is given by [Ref. 17],

$$\delta = \cos^{-1}\left[-\frac{Xa + Xq}{Xd - X_q}\left[\frac{E_f}{V}\right]\right] \qquad \ldots(4.26)$$

To examine the significance of the reluctance torque component, the motor reactances have to be calculated and using the Moog motor as an example yields,

$$X_d = 0.194 \text{ ohms @ } 50 \text{ Hz}$$
$$X_q = 0.236 \text{ ohms @ } 50 \text{ Hz}$$
$$X_a + X_q = 0.628 \text{ ohms @ } 50 \text{ Hz}$$
$$E_f/V = 0.95 \text{ typically}$$

Hence the total torque is given by,

$$T = k \left[0.95 \sin\delta - \frac{0.067}{2} \sin 2\delta \right] \quad \ldots(4.27)$$

The peak reluctance torque component is approximately 3.5% that of the peak field component. Further, the Moog motor controller is adjusted so as to maximise the output torque per unit current input corresponding to a motor torque angle δ of approximately 90 degrees. Since the reluctance torque varies with $\sin 2\delta$ it is apparent that the reluctance torque component can be ignored in this case with little loss in accuracy.

4.2.2 Alternative Derivation of Motor Constant Torque.

The previous equation for synchronous motor torque assumed the rotor field and the stator m.m.f. to be sinusoidal. In the case of a motor with surface mounted magnets, the rotor field distribution is not sinusoidal. As shown in chapter three the rotor field could be considered to be composed of a large fundamental field and a number of harmonics. It is the interaction of the rotor air-gap fields with the stator current that produces the rotational torque of the motor, neglecting the reluctance component. It was shown in chapter three that when the three phase windings of the stator are energised with a balanced three phase voltage, a series of rotating m.m.f. waves were set up in the motor air-gap. When operating as a motor the rotor field produced by the magnets rotates synchronously with the fundamental stator m.m.f. wave and asynchronously with all harmonic m.m.f. waves. It is the interaction of the stator fundamental m.m.f. and the rotor magnetic field which produces the useful motor torque and an expression for this torque can be derived as follows:-

The fundamental m.m.f. wave may be considered to have been produced by a sinusoidally distributed current wave rotating in a similar manner to the m.m.f. but displaced by ninety electrical degrees as shown in figure (4.10).

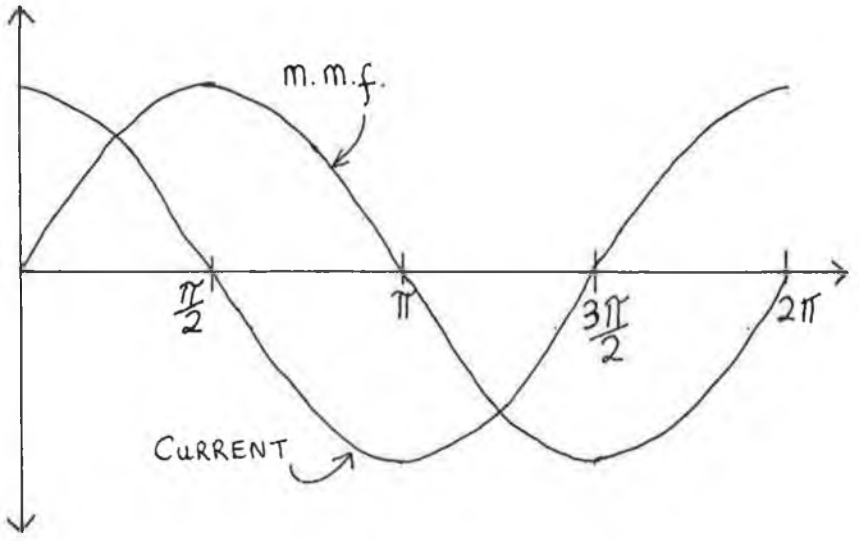

Fig. (4.10) Fundamental Current and M.m.f waves in Air-gap of the motor due to stator current.

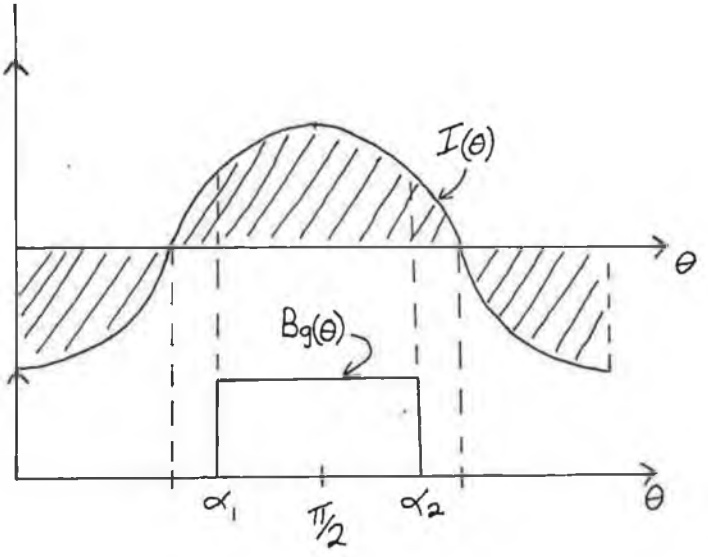

Fig.(4.11) Relative spacial position of Rotor Magnetic Field and Stator Fundamental Current wave for maximum Torque in a P.M. motor.

The average flux density in the air-gap B_g produced by the rotor magnets is calculated using the magnetic circuit concepts outlined in chapter two. Use is made of Carter's coefficient to account for the presence of the stator slots. The peak of the stator current wave is aligned with the centre of a rotor pole as illustrated in figure (4.11). This represents the synchronous motor with a load angle δ of ninety degrees and should yield the maximum motor torque per unit current as previously explained. The reluctance torque component is ignored in this calculation as $\sin 2\delta$ is zero.

The force $\triangle f$ on a current element $\triangle i$ of length 1 is given by,

$$\triangle f = \triangle i.l \times B_g \qquad \ldots(4.28)$$

Numerically, the force F on a pole of the motor is given by the integral of the elemental forces $\triangle f$ over the the electrical angle α_1 to α_2, i.e. over the width of the magnet face neglecting fringing effects. The direction of the force is given by the cross product of the vectors 1 and B_g. In this analysis it is assumed that the flux lines travel radially across the air-gap and no force is generated by the current distributed between 0 and α_1 and α_2 and π degrees. It is shown in reference [10] that the peak m.m.f. in a three phase winding is given by,

$$\text{Peak m.m.f.} = \frac{6.M.n.(kp.kd)}{\pi} \qquad \ldots(4.29)$$

M is the peak ampere turns per coil.
n is the number of turns per pole per phase.

The m.m.f. distribution is of the form, $\frac{-6.M.n.(kp.kd)}{\pi}.\cos\theta$

The current distribution is given by the derivative of the m.m.f. distribution with respect to θ [Ref. 10], as shown in figure (4.10).

$$I_{dist} = \frac{6.M.n.(kp.kd).\sin\theta}{\pi} \qquad \ldots. \text{EQN (4.30)}$$

If the mechanical force produced per pole is given by F_p and r is the radius of the rotor, then the torque per pole T_p is given by,

$$T_p = B_g.r.l.\int_{\alpha 1}^{\alpha 2} \frac{6.M.n.(kp.kd).\sin\theta.d\theta}{\pi}$$

$$= B_g.r.l.2.\int_{\alpha 1}^{\pi/2} \frac{6.M.n.(kp.kd).\sin\theta.d\theta}{\pi}$$

$$= \frac{B_g.r.l.2.6.M.n.kp.kd}{\pi}.(\cos\alpha_1)$$

...(4.31)

Total motor torque is given by the product T_p times pole number

$$T_{total} = \frac{B_g.r.l.\theta_p.12.M.n.kp.kd.\cos\alpha_1.poles}{\theta_p.\pi}$$

$$= \frac{\Phi_p.poles.I_{pp}.N_{eff}.\cos\alpha_1}{poles} \cdot \frac{12}{\theta_p.\pi}$$

...(4.32)

where Φ_p is the total flux per pole (webers).
poles is the number of poles.
I_{pp} is the peak current per phase.
N_{eff} is the effective number of turns per phase.
θ_p is the pole arc angle (radians).

Equation (4.32) is in a similar form to that commonly used in D.C. motor analysis and in terms of the Imperial system of units is given by,

$$\text{Torque} = 1.328\text{x}10^{-5}.\Phi_p.poles.kp.kd.Co.\frac{\sqrt{3}}{2}.I_{pp} \quad ...(4.33)$$

where Co is the total number of series conductors per phase.

Φ_p is measured in kilolines.

θ_p = 0.360 for the Moog motor.

4.3 Derivation of Motor Back E.m.f.

An expression for the generated e.m.f. in an a.c. distributed winding subjected to an alternating magnetic field is [Ref. 10],

$$E_{1rms} = (4.443).(f).(N_{eff}).(\Phi_1) \quad \text{(volts)} \qquad \ldots(4.34)$$

where E_{1rms} is the fundamental r.m.s. generated voltage.

N_{eff} is the effective number of series turns per phase.

Φ_1 is the maximum fundamental flux per pole.

f is the frequency of alteration of the magnetic field.

Considering a rectangular pole flux distribution as before (fig. (4.11)),

$$\Phi_1 = \left| B_g.\frac{4}{\pi}.\cos\alpha_1 \right| \left| \frac{2}{\pi} \right| \left\{ \frac{l.r.2\pi}{\text{poles}} \right| \quad \text{(webers)}$$

$$\ldots(4.35)$$

The first expression in brackets in equation (4.35) is the fundamental gap flux density. Rewriting equation (4.34) gives,

$$E_{1rms} = (4.443).(\text{pole pairs}).(f\ \text{mech}).(N_{eff}).(\Phi_1)$$

Therefore,

$$E_{peak/rad.s^{-1}} = 2.5465.(\text{poles}).(N_{eff}).(B_g\cos\alpha_1).\left|\frac{l.r}{\text{poles}}\right| \qquad \ldots(4.36)$$

Equation (4.36) is an expression for the peak generated fundamental voltage per phase per mechanical radian per second. The peak line to line generated voltage per mechanical radian per second is thus given by,

$$E_p/\text{rad/sec} = 4.4107.(N_{eff}).(B_g\cos\alpha_1).(l.r) \quad \text{(volts)}$$

...(4.37)

E_p/rad/sec may be termed the back e.m.f. constant of the motor, K_e. If the torque constant K_t is defined as the torque developed per $\sqrt{3}/2$ times I_{pp} then it is found to be numerically equal to K_e, i.e.,

$$\frac{T}{\sqrt{3}/2.I_{pp}} = \frac{2.12}{\sqrt{3}.\pi}.(N_{eff}).(B_g\cos\alpha_1).(l.r)$$

$$= 4.411(N_{eff}).(B_g\cos\alpha_1).(l.r) \quad \text{(Nm A}^{-1}\text{)}$$

...(4.39)

This definition of K_t is presently used by Moog Ltd. The numerical equivalence between K_t and K_e only holds for the S.I. system of units.

4.4 Harmonic and Pulsating Torques.

In addition to the constant steady state torque arising from the interaction of the rotor magnetic field and the stator primary current wave, harmonic torques may arise due to the presence of harmonic current waves [Refs. 20,21,22]. These current waves may rotate synchronously or asynchronously with respect to the rotor magnetic field and will produce two different torque components, harmonic constant torques or harmonic pulsating torques. It is convenient in this case to represent the current wave produced by the stator windings and the magnetic field produced by the rotor magnets by their equivalent Fourier series as was done in the previous chapter. In general therefore an expression for the torque produced by the interaction of a current harmonic and a magnetic field harmonic neglecting saturation and high frequency skin effects is given by,

$$T = \int_0^{2\pi} A_n \cos(n\theta + wt) . B_m \cos(m\theta) . d\theta$$

where A_n is the current harmonic wave magnitude
B_m is the magnetic field harmonic magnitude
θ is the mechanical angle around the air-gap. ... (4.40).

It can be shown that the integral in equation (4.40) is zero if the harmonic orders m and n are not the same and is equal to $A_n.B_m.\pi\cos(-wt)$ if m and n are equal. Thus it is evident that the order of the current wave and the magnetic field must be equal in order to produce any torque. If the harmonic orders are the same, two distinct cases arise, on the one hand a field and a wave rotating in synchronism producing a harmonic constant torque and on the other hand a field and a wave rotating asynchronously producing a pulsating torque of frequency ω.

In the case of a synchronous motor supplied by a PWM inverter harmonic torques may occur as a result of current time harmonics in the stator windings. These torques are mostly pulsating in nature but it is possible to produce a harmonic constant torque as follows. If a current time harmonic of order n is present in the supply and if the winding produces a forward rotating current wave of order n, the current wave will rotate in synchronism with the rotor. This synchronously rotating current wave will interact with a rotor magnetic field of the same order, if it is present, and will produce a constant torque component. The magnitude of these components are neglible in the case of the Moog motor when compared with the torque component due to the fundamental supply current.

To evaluate the torque ripple in a synchronous motor therefore requires a knowledge of the rotor magnet harmonics, the stator winding harmonics and the modulating effect of the stator and rotor slots on the air-gap permeance. The effect of current time harmonics are dealt with in the next chapter under the heading of supply harmonic effects. Since the subject of rotor magnet harmonics and stator winding harmonics have been dealt with in some detail in the previous chapter a brief discussion of the torque ripple in the motor being studied will serve to illustrate a method of torque-ripple determination.

In chapter three a method of analysing the winding m.m.f. of the stator was presented and computer simulated results were presented in tabular form for the motor being studied. The actual harmonic current waves are easily obtained from these computer results since the m.m.f. acting across the air-gap is the integral of the stator current distribution [Ref. 10]. In the method used to verify the winding analysis it was explained how to estimate the harmonic flux magnitudes and frequency taking account of the magnet harmonic m.m.f.'s and the air-gap permeance variations. These are the two sets of data required to estimate the harmonic torques produced in a synchronous motor supplied by a sinusoidal voltage supply. Table (4.1) presents the estimated harmonic torques produced in the motor under consideration in this project expressed as percentages of the constant torque up to the 19th harmonic of the primary 12 pole field. An examination of this table reveals that the maximum predicted torque harmonic occurs for a harmonic order of 5 with a peak to peak magnitude of 3.6% that of the constant torque.

TABLE (4.1) HARMONIC TORQUES

Harmonic Order	Current Magnitude	Flux Magnitude	Torque Magnitude (pk to pk)	Pulsating ?
1	100	100	100	NO
3	1.23	8.68	0.22	YES
5	15.8	10.62	3.36	"
7	8.4	11.27	1.90	"
9	2.0	4.0	0.16	"
11	1.76	3.15	0.11	"
13	-	-	-	
15	1.77	2.77	0.10	"
17	1.40	2.45	0.07	"
19	8.74	3.75	0.66	"

Chapter 5.

NONSINUSOIDAL VOLTAGE SUPPLY EFFECTS AND MOTOR LOSSES.

5.1 EFFECT OF NONSINUSOIDAL VOLTAGE SUPPLY

Since the voltage supply to the brushless motor is not perfectly sinusoidal the influence of supply voltage harmonics need to be taken into account when estimating motor torque ripple and motor losses. These voltage harmonics arise as a result of the rapid on/off switching of the transistors in the inverter and will produce time harmonic currents in the stator windings. A series of tests were performed in order to evaluate the magnitudes of these harmonic currents using a spectrum analysiser and a current probe.

Table (5.1) presents harmonic current magnitudes expressed as a percentage of the fundamental phase current for various motor loads. In this case the speed of the motor was 560 r.p.m. which is equivalent to a fundamental supply frequency of 112 Hz. The triangular wave Carrier frequency (C_f) was 5.2 kHz, therefore the ratio of Carrier to Modulating frequency was approximately 46 to 1. The magnitude of the Carrier wave was 2.04 volts peak and the magnitude of the Modulation signal varied from 0.65 peak volts at the lightest load to 1.05 volts peak at maximum load. Table (5.2) presents the harmonic current magnitudes measured at various motor speeds with the motor unloaded. It is seen that the magnitudes of the harmonic current relative to the fundamental current are a function of motor load and that in general reduce as the motor load increases.

Since the inverter used in this project is a voltage source inverter the magnitudes of the harmonic currents are dependent on the voltage supply harmonics and the impedence presented by the motor to the supply. A number of Papers dealing with voltage harmonics produced by inverters have been written [refs. 23 and 24] which predict the magnitudes of the harmonics based on the switching action of the transistors. Reference [24] takes account of the dead time required to allow proper turn-off of the transistors and is thus a more complete model. Some papers [Refs. 20, 21 and Refs. 25 to 29] have also been written which consider the effects of non-sinusoidal voltage supplies on motor performance although these tend to concentrate on induction motors.

TABLE (5.1) CURRENT HARMONICS

Measured Current Harmonics of a Permanent Magnet Brushless A.C. motor fed by a PWM voltage Source Inverter.

Harmonic Order	Fundamental r.m.s. phase current (amps) 1.69	2.28	3.55	4.64	5.83	6.60
Mod. Index	32 %	37 %	40 %	42 %	49 %	52 %
1	100.0	100.0	100.0	100.0	100.0	100.0
3	1.7	1.8	0.9	0.7	0.2	—
5	10.1	7.8	6.2	4.7	4.0	3.5
7	3.5	4.4	3.1	2.8	2.4	2.1
13	8.4	5.8	3.0	3.2	2.3	2.2
15	8.4	5.6	2.9	2.8	2.0	1.9
C_f	7.8	6.3	5.2	4.4	4.7	4.3
$C_f x2$	11.0	6.7	5.0	3.6	2.7	3.1
$C_f x3$	3.0	2.5	1.9	1.6	1.5	1.4
$C_f x4$	5.0	3.0	2.2	1.5	1.1	1.2

TABLE (5.2) CURRENT HARMONICS

Harmonic Order	Motor Speed r.p.m. (Unloaded) 560	1178	2407	4316
1	100.0	100.0	100.0	100.0
3	5.1	4.9	10.2	13.6
5	2.3	12.4	—	17.0
7	5.1	2.6	—	—
C_f	41.7	38.0	51.8	60.9
$C_f x2$	59.6	58.2	48.4	9.3
$C_f x3$	15.3	13.6	15.3	5.1
$C_f x4$	25.4	18.8	5.9	—

5.2 HARMONIC TORQUES.

From the viewpoint of torque production each current harmonic in the supply could be considered as independently producing a series of rotating current waves in a manner similar to the fundamental current harmonic. The interaction of these current waves with the rotor magnetic field could be considered as was done previously. From a practical point of view only the main current wave produced by each current harmonic needs to be considered. Furthermore it is likely that the effect of harmonic currents at multiples of the PWM carrier frequency on the torque ripple can be neglected due to magnetic skin effects and mechanical damping. Therefore consideration of the low frequency harmonic currents is sufficient to estimate the torque ripple effects due to the Inverter supply. Since the torque produced as a result of the interaction of the rotor field and the stator current wave is proportional to the magnitude of the stator current wave, the relative torque magnitudes are readily calculated. It is evident from the results in Table (5.1) that the predominant low frequency torque occurs at the fifth harmonic frequency.

5.3 LOSSES AND HEATING EFFECTS.

Because of the temperature characteristics of Nd-Fe-B, a series of tests was carried out to determine the maximum temperature which the rotor magnets would be subjected to. These tests were also expected to identify the relative losses in the stator and rotor and to determine if heat conduction across the air-gap was significant. The tests were carried out using a standard stator and two rotors, one of which was of solid construction, the other being made up of laminations. The stator I.D. was 53.3 mm and the O.D. of the two rotors was 45.7 mm leaving an air-gap of approximately 3.8 mm. The stator was energised using a standard Moog inverter and power supply in such a way that a stationary-in-space, pulsating-in-time, magnetic field was set up in the air-gap. A brief discussion of these tests and the results obtained follows,

5.3.1 D.C. Current Tests.

The rotor was placed in the stator air-gap with paper filling the air-gap space in an effort to reduce any heat conduction across the gap. The stator was energised with a pseudo D.C. current for a period of ten minutes and was then allowed to cool down. The temperature of the windings and of the rotor were monitored using thermocouples and their temperature profiles with time are shown in Plot (5.1) and (5.2). It is seen that the temperature rise in the stator far exceeds that of the rotor and that the rotor temperature continues to rise after the supply current has been interrupted. This suggests that heat transfer is taking place across the air-gap particularly since the rotor temperature decreases only after the winding temperature falls below it.

Comparative data for the two rotors is presented below. Included in this data are calculated values for the stator and rotor losses in Watts. These are calculated based on the temperature rise of the stator and rotor and on estimated values for their respective heat capacities. The heat capacity of the stator is calculated using the mass of Copper and Iron it contains, along with the appropriate specific heat constants. The heat capacity of the rotor is estimated in a similar fashion. Heat loss to the surrounding air is ignored in these calculations and therefore the calculated stator loss is likely to be underestimated.
The value for stator I^2R losses is based on the average winding temperature during the energisation stage and on the average D.C. current in the windings. The D.C. current contained a 5 % ripple at a frequency of approximatelty 6 kHz and this is likely to have increased the I^2R losses due to the skin effect [Ref. 25]. From the calculated values for losses it appears that I^2R losses are the main cause of stator heating. There is little difference in the heating rates of the two rotors in this case.

	Solid Rotor	Laminated Rotor
Max D.C. Phase Current (A).	7.5	7.6
Maximum Winding Temp. (°C)	98.0	105.0
Maximum Rotor Temp.	46.3	49.5
Rotor Temp after I → zero.	31.2	31.8
Average Stator Temp. rise (°C/min)	7.5	7.86
Average Rotor Temp. rise	1.16	1.20
Calculated Rotor Loss (Watts)	5.0	5.1
Calculated Stator Loss (Watts)	72.0	75.0
Average I^2R Loss (Watts)	72.0	74.0

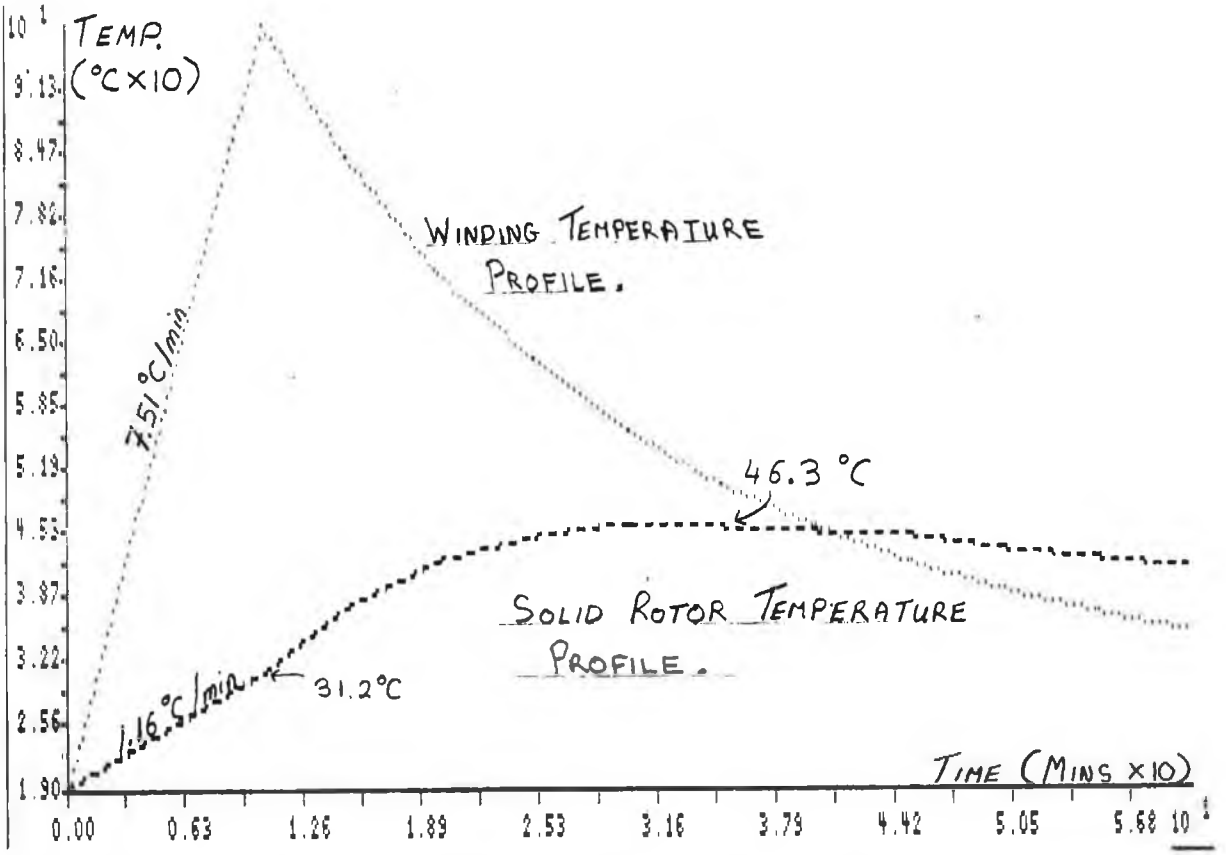

Plot (5.1) Temperature Profile of Stator winding & Solid Rotor subject to pseudo D.C. heating current.

Plot (5.2) Temperature Profile of Stator winding & Laminated Rotor subject to pseudo D.C. heating current.

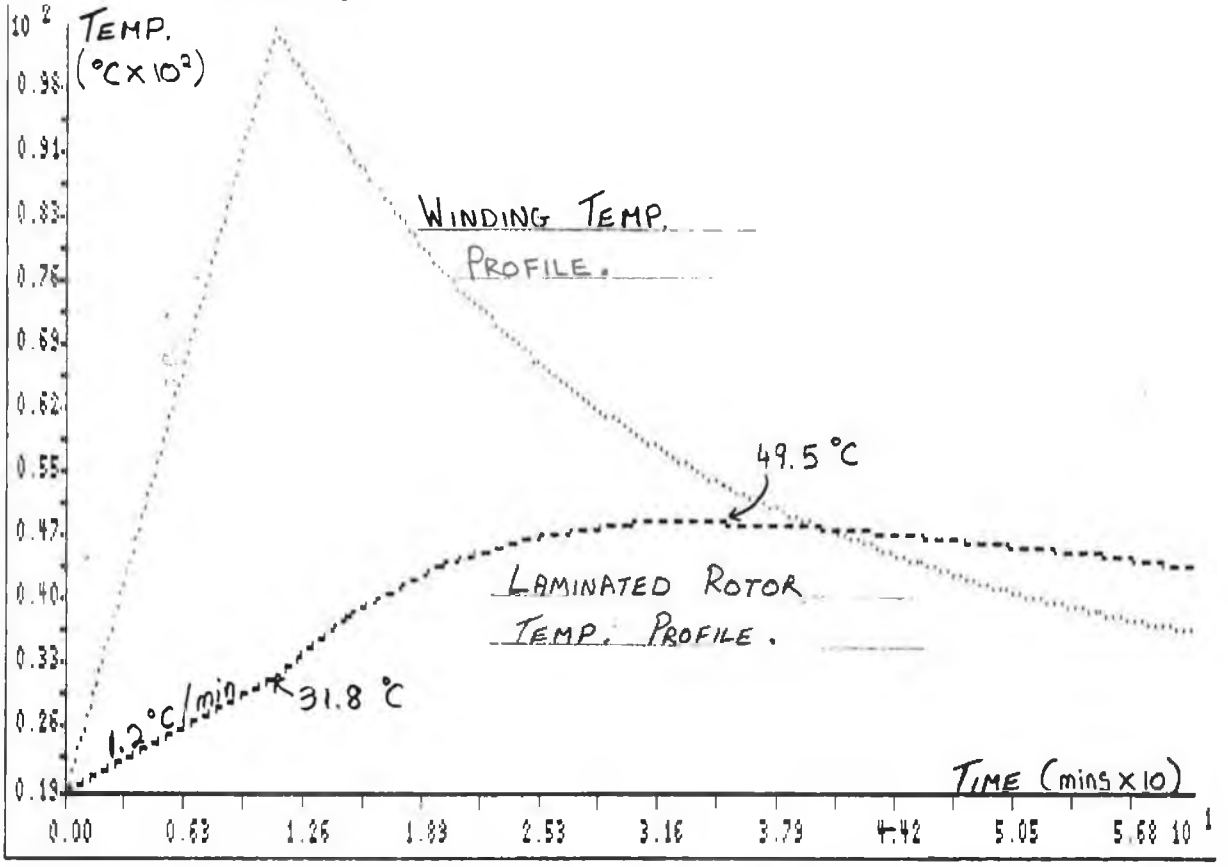

5.3.2. A.C. Current Tests.

In this case A.C. current at a frequency of 250 Hz was used to energise the windings with the basic test set-up unchanged. The results were similar to those achieved with D.C. current except that the heating rate of the solid rotor was 29 % greater than the laminated rotor whereas the stator heating rate was only 2 % higher. This suggests that the losses in the solid rotor were greater than those in the laminated rotor. The temperature profiles are presented in plots (5.3) and (5.4) and comparative data is given below.

In the case of the calculated stator I^2R losses only the fundamental current harmonic was accounted for although high frequency current harmonics may increase the heating effect considerably due to the skin effect. The calculated stator I^2R losses again appear to account for most of the stator losses in this case.

	Solid Rotor	Laminated Rotor
Phase r.m.s. Current (A).	8.0	7.9
Maximum Winding Temp. (°C)	109.3	106.3
Maximum Rotor Temp.	49.3	47.9
Rotor Temp after I → zero.	32.6	28.6
Average Stator Temp. rise (°C/min)	9.28	9.10
Average Rotor Temp. rise	1.61	1.25
Calculated Rotor Loss (watts)	6.9	5.3
Calculated Stator Loss (watts)	89.0	87.0
Average I^2R loss (watts)	82.0	80.0

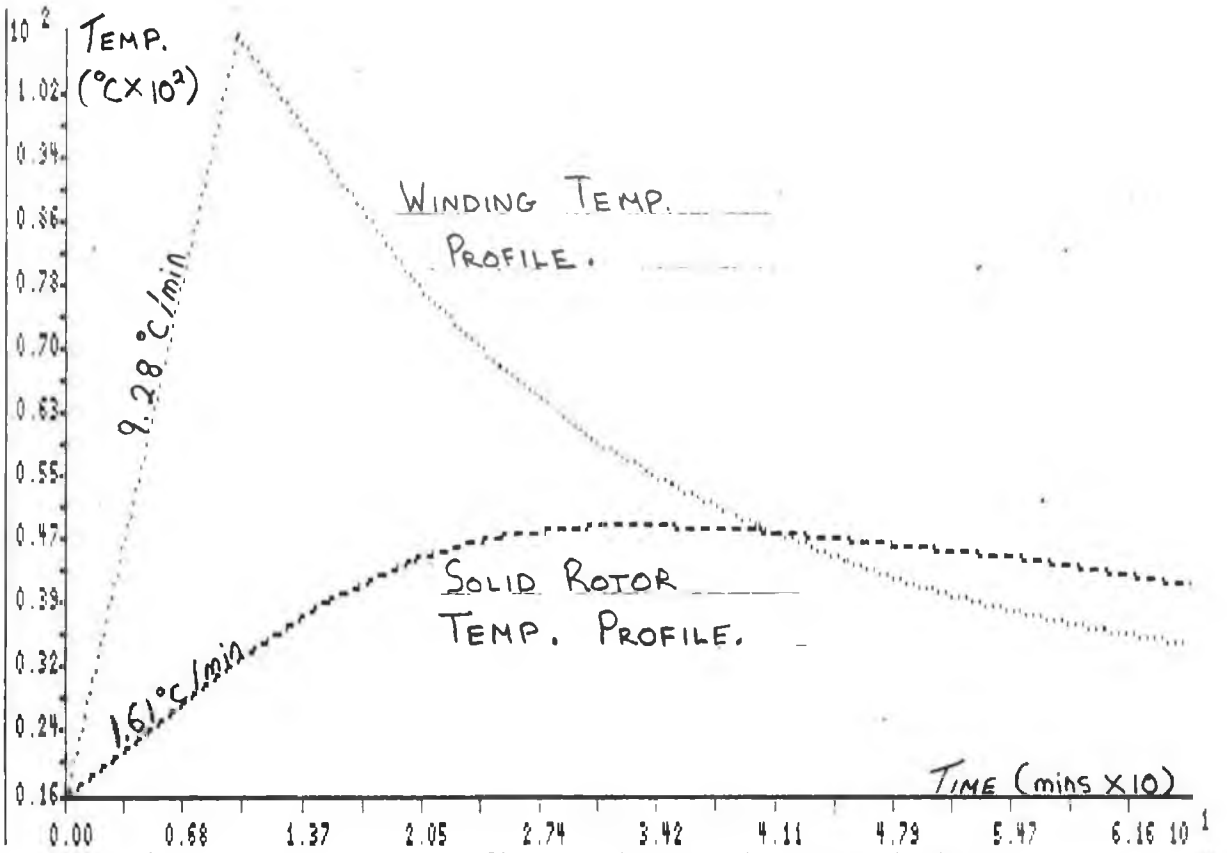

Plot (5.3) Temperature Profile of Stator winding & Solid Rotor subject to 250 Hz A.C. heating current.

Plot (5.4) Temperature Profile of Stator winding & Laminated Rotor subject to 250 Hz A.C. heating current.

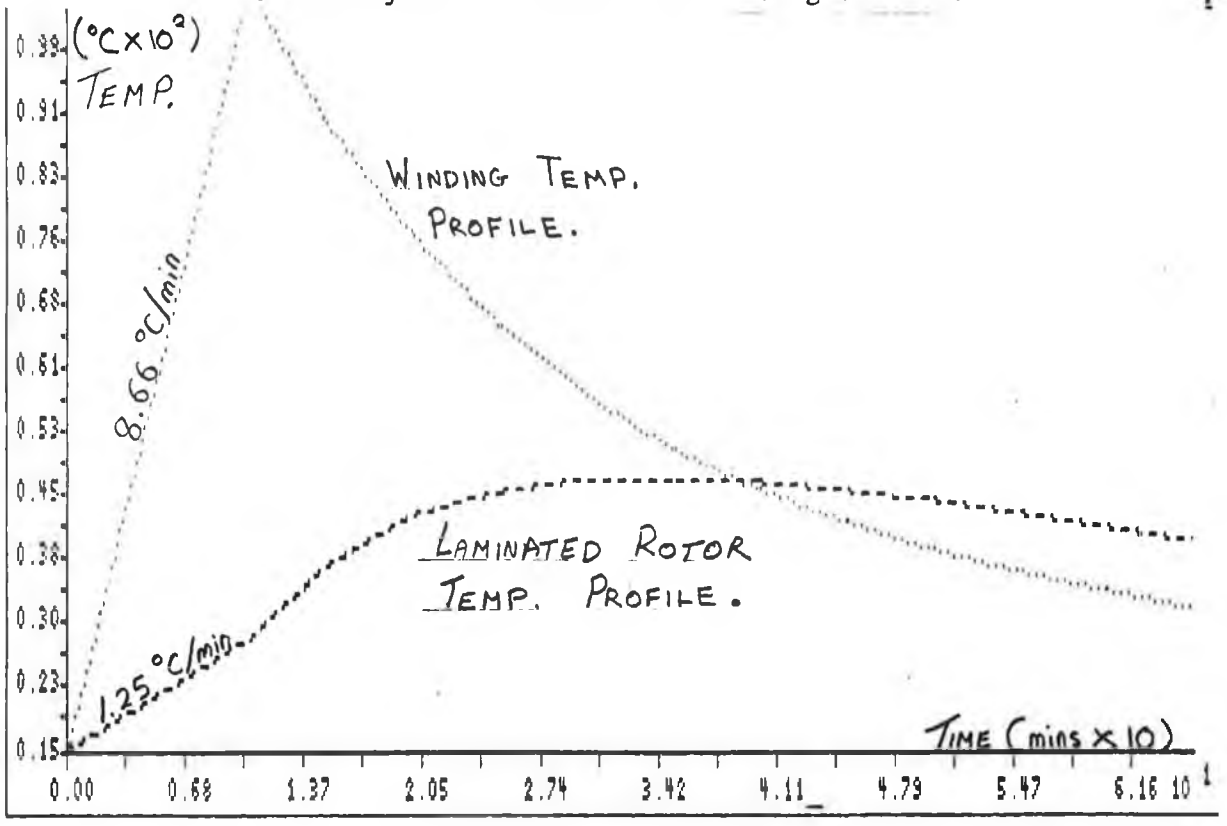

5.3.3 Effect of Frequency on Heating Rate.

Tests were performed using three different supply frequencies to see if the heating rate of the stator and rotor were dependent on this parameter. The solid rotor was used since its losses should be most affected by high frequency magnetic fields. The basic shape of the temperature profiles did not change, however, the heating rates of both stator and rotor did exhibit an increase with frequency Plots (5.3), (5.4) and (5.6). The heating rate of the stator increased by 5.3 % and 24 % while the rotor heating rate increased by 36 % and 105 % indicating that rotor losses are more frequency dependent. This is not to be unexpected since the small wire size reduces the skin effect in the windings thus making the I^2R losses less frequency dependent.

It should be noted that the current supply at 500 Hz took on a triangular waveform due to distortion which resulted in the large increase in heating rates. The calculated stator I^2R losses based on the fundamental stator current only do not take account of this effect.

	125 Hz	250 Hz	500 Hz
Phase r.m.s. Current (A).	7.9	8.0	7.9
Maximum Winding Temp. (°C)	107.5	109.3	124.0
Maximum Rotor Temp.	49.9	49.3	56.0
Rotor Temp after I → zero.	31.2	32.6	38.6
Average Stator Temp. rise (°C/min)	8.81	9.28	11.0
Average Rotor Temp. rise	1.18	1.61	2.43
Calculated Rotor Loss (watts)	5.0	6.9	10.4
Calculated Stator Loss (watts)	85.0	89.0	106.0
Average I^2R loss (watts)	80.0	82.0	80.0

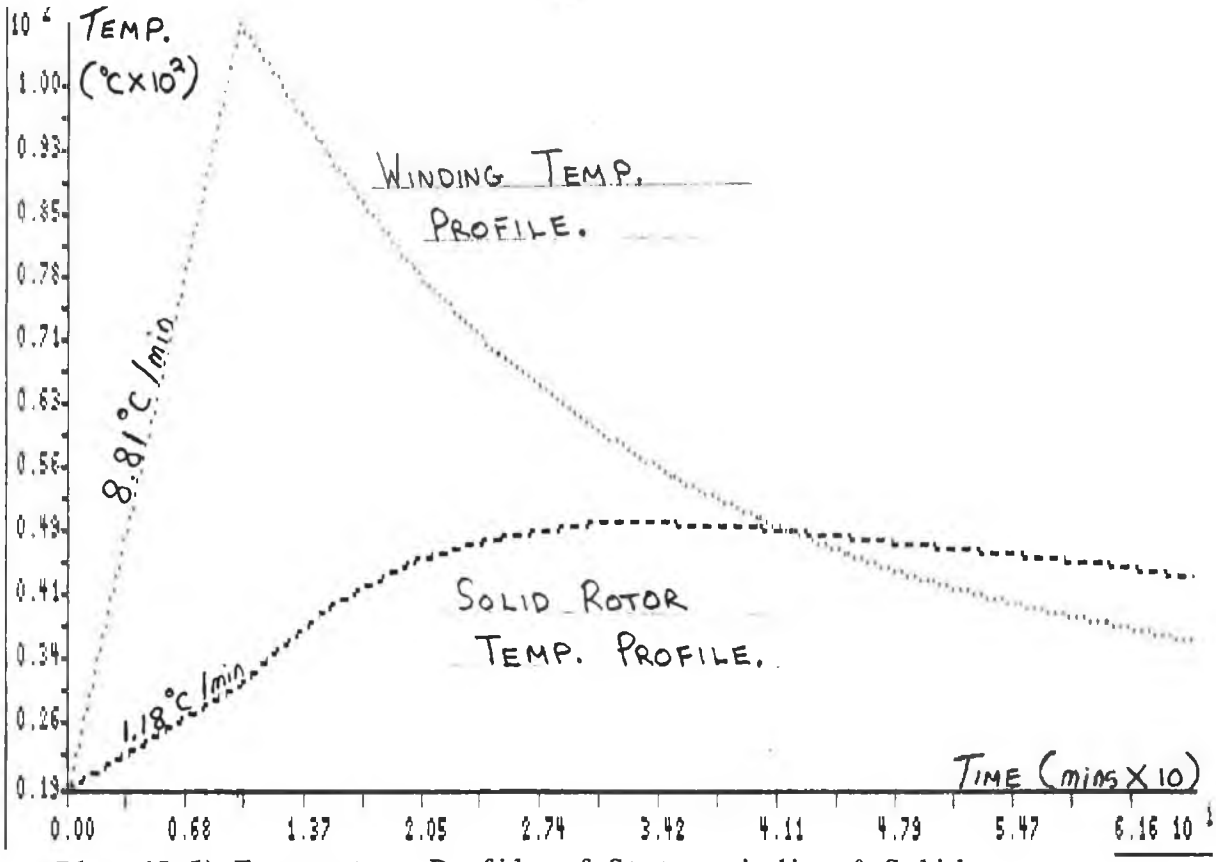

Plot (5.5) Temperature Profile of Stator winding & Solid Rotor subject 125 Hz A.C. heating current.

Plot (5.6) Temperature Profile of Stator winding & Solid Rotor subject 500 Hz A.C. heating current.

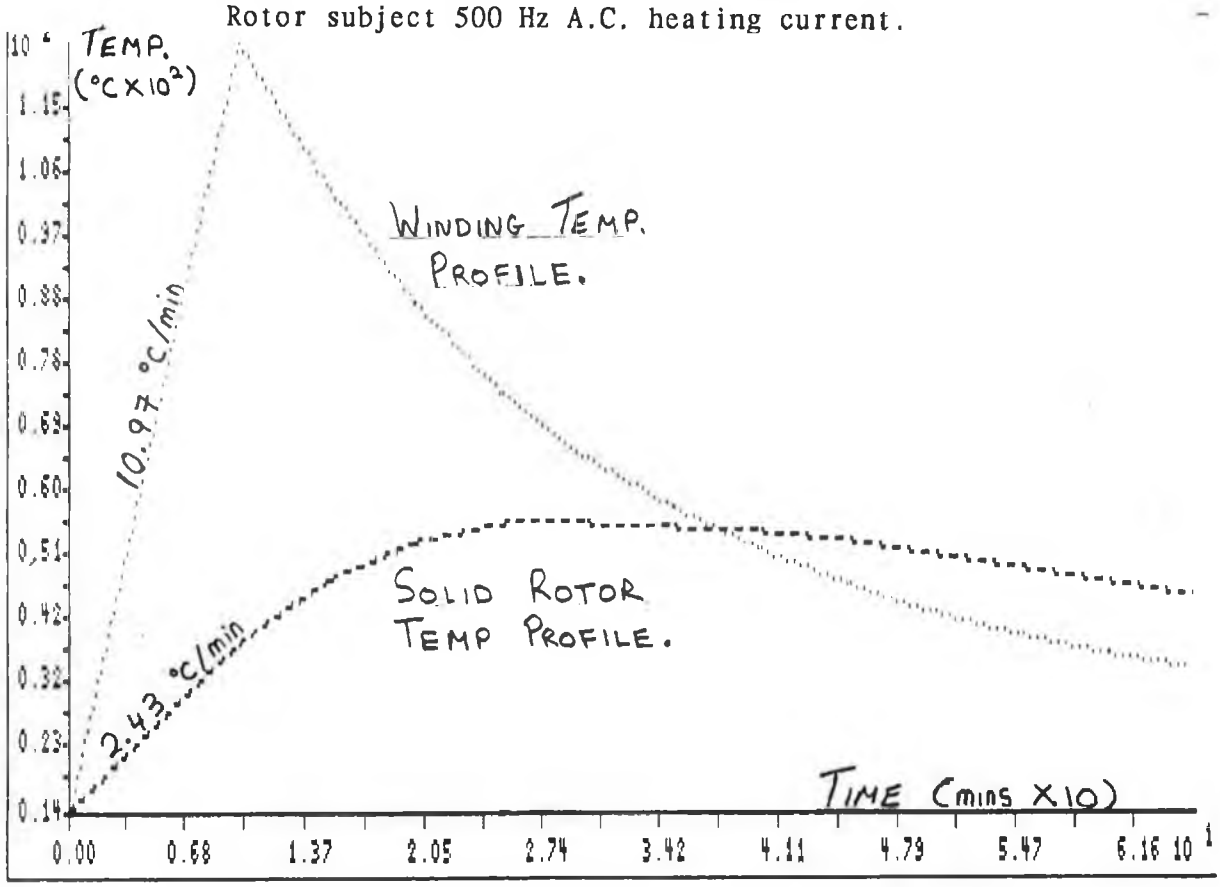

5.3.4 Steady State Heating Tests.

The stator was supplied with a 250 Hz current and brought up to a steady temperature of about 111 °C and maintained at this temperature for more than an hour. The temperature of the windings and rotor were monitored and Plot (5.7) presents this data against time. It is seen that the rotor temperature rises quickly over the first hour and more slowly over the second hour as the temperature difference between the stator and rotor decreases.

In some ways this test was the most significant in that the temperature difference between the stator and rotor reduced to approximately 12°C over a period of time. This helps to establish the maximum temperature that the rotor magnets could be subjected in a servo-motor application. The proposed motor specification includes a class F insulation rating and thus the maximum winding temperature would be 145°C based on the average winding temperature. The motor controller incorporates motor protection such that this maximum temperature is not exceeded, however, the possibility still exists for the winding temperature to remain at temperatures of this level indefinitely. In this event the rotor could be subjected to temperatures in the region of 135°C for prolonged periods which has important implications for the use of Nd-Fe-B magnets.

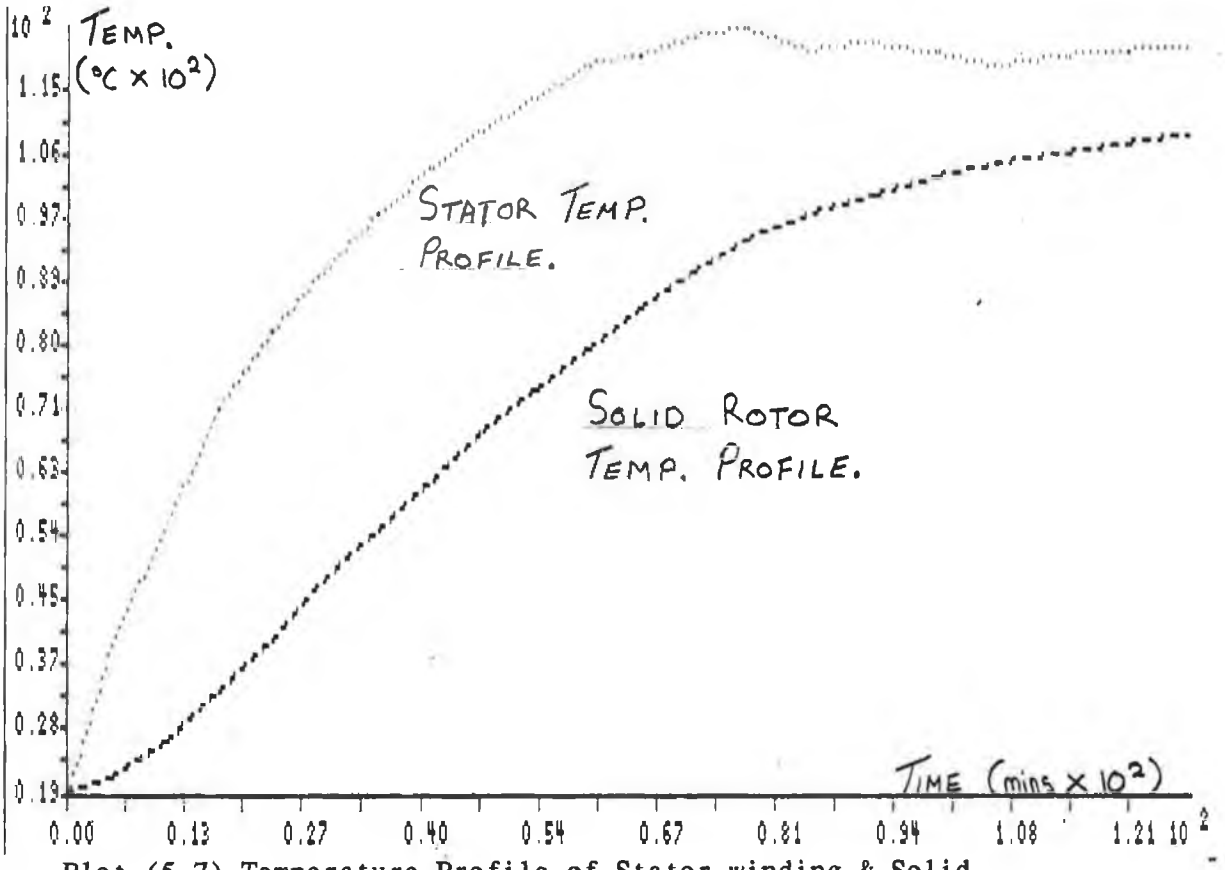

Plot (5.7) Temperature Profile of Stator winding & Solid Rotor for duty cycle heating tests.

Plot (5.8) Temperature Profile of Stator winding & Solid Rotor with the assembly forced cooled.

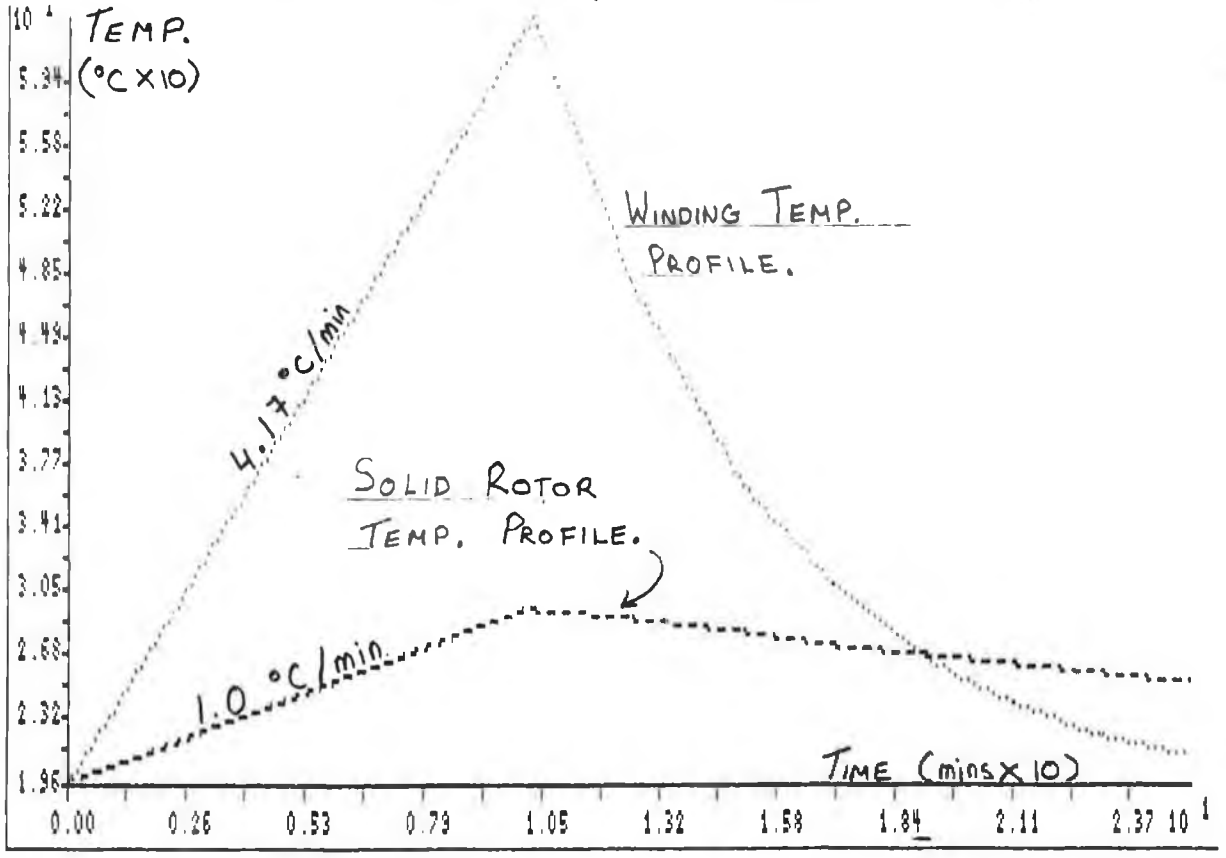

5.3.5. Forced cooling of stator.

In an effort to thermally isolate the rotor from the stator, cooling air was introduced in the air-gap and around the stator structure. The rotor was wrapped in a number of paper layers so as to reduce the cooling effect on it. Heating tests were again carried out on both the solid and laminated rotors and the temperature profiles are shown in Plots (5.8) and (5.9) and a summary of important data is given below.

	Solid Rotor	Laminated Rotor
Phase r.m.s. Current (A)	7.96	8.03
Maximum Winding Temp. (°C)	63.0	61.6
Maximum Rotor Temp.	29.8	28.6
Rotor Temp after I → zero.	29.8	28.6
Average Stator Temp. rise (°C/min)	4.17	4.28
Average Rotor Temp. rise	1.00	0.98

The maximum stator temperature has been reduced by approximately 50 % for the same energisation level. The maximum rotor temperature occurred just prior to the interruption of the stator heating current indicating that little or no heat transfer took place across the air-gap. The paper lagging around the rotor appears to have been quite effective when the cooling rates of the stator and rotor are compared. In this case the heating rate of the solid rotor is about 5 % greater than the laminated case which is not of major importance when selecting the rotor magnet material. In order to illustrate the significance of heat transfer across the air-gap the temperature profiles of the solid rotor in both the case of a cooled and an uncooled stator are shown in Plot (5.11).

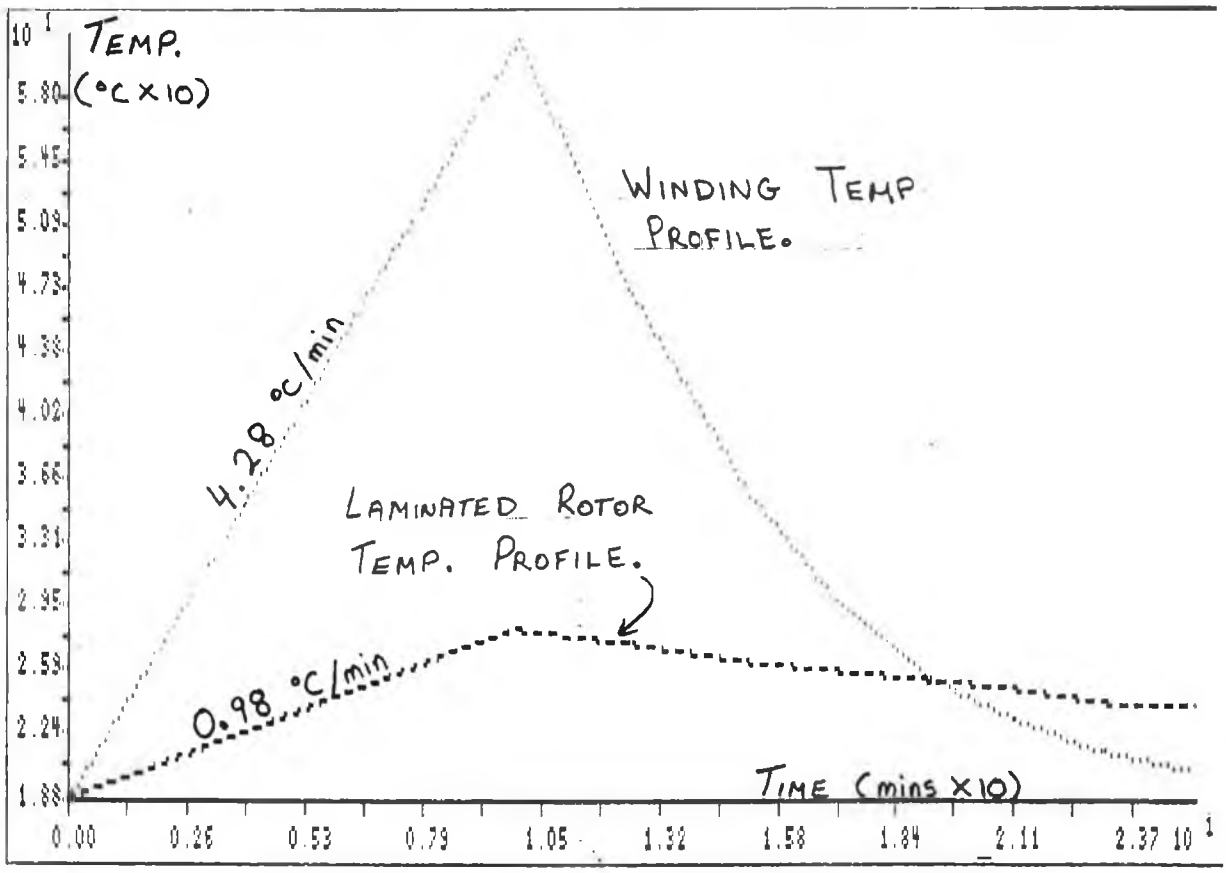

Plot (5.9) Temperature Profile of Stator winding & Laminated Rotor with the assembly forced cooled.

Plot (5.10) Temperature Profile of Stator winding & Solid Rotor with natural cooling only.

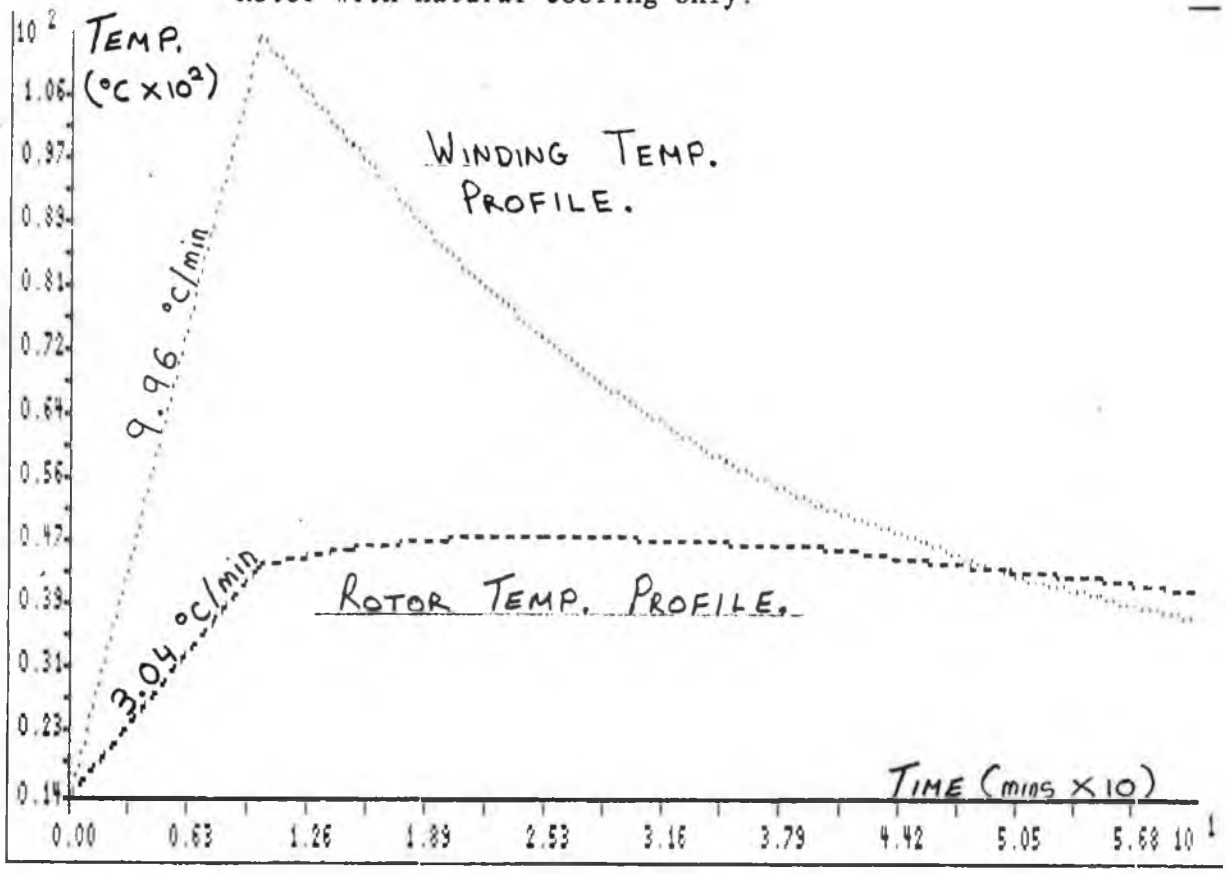

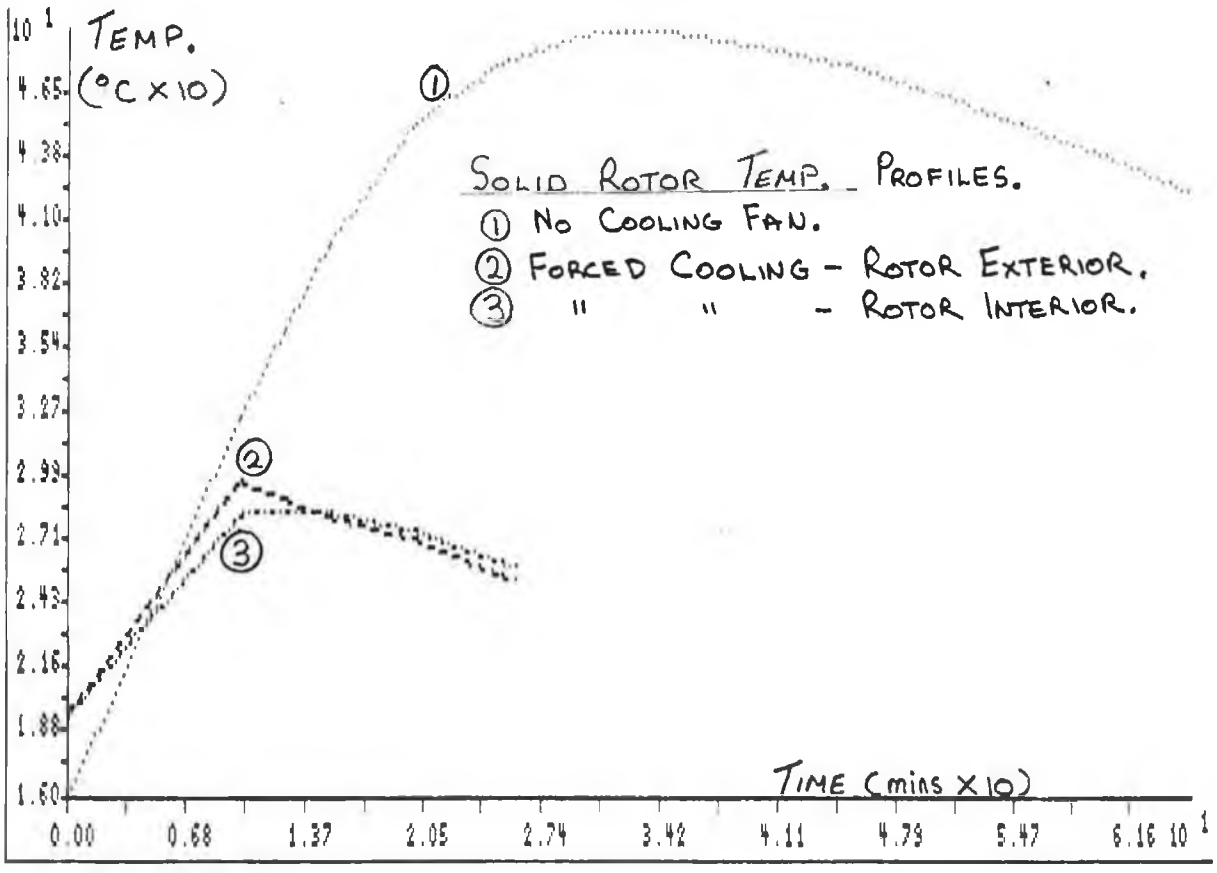

Plot (5.11) Temperature Profile of Stator winding & Solid Rotor under various conditions.

5.3.6. Stator and Rotor not lagged.

Finally a test was carried out with the rotor and stator unlagged and placed in a an uncooled box. In this case the rate of temp rise of the rotor was far greater than in the previous tests. Some increase in rotor temperature occurred after the current was interrupted apparently as a result of heat transfer across the air-gap. The temperature profiles of stator and rotor are shown in Plot (5.10), It is likely that heat transfer across the air-gap would be more significant in an actual motor under load conditions since the motor is completely enclosed and the effect of the rotating shaft would tend to cause turbulent air flow in the air-gap assisting heat transfer. In the testing arrangement described little or no air movement would have occurred other than convective currents and a boundary insulating layer on each surface was likely to have existed.

5.4. DISCUSSION.

These tests provide information regarding the loss and heating mechanisms in a servo-motor that is of use at an initial design stage. For instance it is seen that the heating rate in the stator is significantly greater than that of the rotor and that heat transfer across the air-gap occurs when a temperature differential is present. Furthermore the predominant cause of stator heating seems to be the I^2R winding losses. Obviously this is of importance when considering the application of Nd-Fe-B to servo-motors since the in–service rotor temperature is dependent on both stator and rotor losses. While the laminated rotor showed smaller heating effects than the solid rotor the difference in these effects would not affect the choice of rotor magnet material based on thermal considerations. If the stator were forced cooled utilisation of even highly temperature sensitive Nd-Fe-B material grades should be possible.

The manner in which these tests were conducted did not facilitate the exact duplication of the heating conditions to which the motor would be subjected in normal operation. The use of the inverter produced high frequency current harmonics in the stator winding along with their associated heating effects. A stationary pulsasting-in-time magnetic field was applied to the stator and rotor cores. Usually the fundamental field would be rotating in synchronism with the rotor and would not produce any losses in it while all other harmonics are moving relative to the rotor and will produce losses. Since the fundamental is much bigger in magnitude than the harmonics the overall rotor heating effect under actual motor conditions is likely to be smaller than measured in these tests. On the other hand the heating effects in the stator core may be greater due to the the relative motion

of the rotor field which is much larger than the field produced by the windings under continuous operating conditions.

Quite a number of papers have been written on the losses in induction motors and polyphase motors in general, subjected to non-sinusoidal voltage sources [Refs. 25 to 29]. The actual loss mechanisms in the two motor types are similar but because of the different rotor constructions would not be in the same proportion. In a Brushless servo motor the loss mechanisms can be divided into two main areas, stator I^2R copper losses and magnetic field losses and a brief discussion on each of these mechanisms will be given.

5.5 I^2R LOSSES.

When calculating the losses associated with the stator windings it is important to take the skin effect into account. This effect is of particular importance if the current in the windings contains high frequency harmonics and if the cross-sectional area of the conductors is large. In references [17] and [26] formulae are given which express the ratio of the A.C. to D.C. resistances as functions of the conductor cross-sectional area and the number of conductor layers in a slot. These formulae indicate that the heating effect due to a particular current harmonic is not solely dependent on the r.m.s. current value alone and that the effective resistance of the winding may be many times greater than it's D.C. value. In reference [25] the author compares the losses calculated for Square wave and PWM excitation and concludes that even though the distortion levels in the PWM excitation system are comparable or less than those in the Square wave system the slot copper losses may increase by up to 50 % due to the skin effect. It is therefore of the utmost importance to minimise the harmonic distortion of the stator current particularly at high frequencies. From tests taken on the Moog motor it appears that quite significant harmonic currents occur at multiples of the carrier frequency and these will undoubtably add to the motor losses.

5.6 IRON LOSSES.

The Iron losses in a motor arise as a result of alternating magnetic fields produced by a number of sources. These include the stator fundamental and harmonic current components, the rotor magnets and the winding distribution around the air-gap. Additional high frequency varying magnetic fields are produced by the reluctance effects of stator and rotor slots. Many studies on the estimation and separation of these losses have been carried out [Refs. 30 to 35]. However

saturation invalidates the use of the superposition principle and it is difficult to separate the individual effects of these phenomena. Nevertheless the main factors affecting Iron loss can be identified and ways of minimising this loss can then be found. An expression for the losses in Watts per kilogram mass of laminations is [Ref. 17],

$$P_{loss} = a.f.B^2 + b\ (h.f.B)^2$$

where f = frequency.
B = is the peak value of flux density.
h = thickness of the laminations.
a and b are constants dependent on the material properties.

This formula assumes that the magnetic field is uniformally distributed across the cross-section of the laminations. At high frequencies the skin effect causes the field to be concentrated on the surface of the laminations leading to increased losses. From the heating tests described earlier on it appears that these heating effects are not as large as the stator I^2R losses, however, from an efficiency point of view minimising them is desirable. Generally these losses can be minimised by,

(1) Reducing the magnitude of the harmonic voltages produced by the Inverter supply since each harmonic excites a loss producing magnetic field.

(2) Select a winding configuration that minimises the sub and super m.m.f. harmonics. The selection of a winding configuration is based on other considerations such as maximising motor torque and minimising torque ripple and in most applications the alternating field losses will be of secondary importance.

(3) Minimise the air-gap reluctance ripple by keeping slot openings to a minimum in the case of the stator and making the rotor surface as smooth as possible.

(4) Laminate both the stator and rotor assemblies in order to reduce the losses due to eddy currents.

These measures will lead to as small an Iron loss as possible for a given design.

Chapter 6.

REDESIGN OF A BRUSHLESS SERVO-MOTOR USING ND-FE-B MAGNET MATERIAL.

6.1 MOTOR DESIGN AND CHOICE OF MOTOR PARAMETERS.

6.1.1 Motor Design Program.

Previous chapters have served to develop the methods and formulae necessary to undertake the initial design of a Brushless servo-motor. This chapter combines these methods to produce possible motor designs utilising Nd-Fe-B magnet material. A Fortran computer program was written to predict the various performance parameters of a design calculated from design input data. Its corresponding flow diagram is shown in figure (6.1) and sample input and output data sets are contained in Appendix (F). Saturation effects produced by stator current armature reaction are neglected in the simulation. Lumped parameter values for the magnetic circuit reluctances are used. Because of these approximations predicted results may not be absolutely accurate. Nevertheless, the influence of various dimensional changes such as magnet length, magnet characteristics, number of winding turns, rotor diameter, etc, are reflected in the calculated performance parameters. The program is therefore useful in the preliminary design stage.

6.1.2 Design Objectives.

Two separate design studies were carried out the object of which were to equal or improve the performance of a servo-motor by substituting Sa-Co magnets with Nd-Fe-B magnets. These studies were subject to a number of constraints which arose out of the desire to be able to compare the performances of a Sa-Co motor and a Nd-Fe-B motor in back to back tests. These constaints were as follows,

(1) The maximum O.D. and Stack length of the Nd-Fe-B motor was not to exceed that of the Sa-Co motor.

(2) The Pole number of the two motors was to be the same in order to allow comparison of the designs on an equal basis.

(3) The two motors should have approximately the same operating speed range using identical controller and power supply units.

Taking these constraints into account the primary design variables for the stator were, the number of winding turns, the wire diameter, the number of stator slots, the stator slot dimensions, the tooth dimensions and the internal stator diameter. The corresponding rotor variables were, the magnet material, magnet dimensions, magnet pole arc ratio and rotor O.D.

6.1.3 Number of Stator Slots.

The winding analysis conducted in chapter three, in addition to the theory developed on harmonic torque production in chapter four, affected the choice of the number of slots for a twelve pole motor. It was seen that the m.m.f. produced by the stator currents in a 36 slot stator while containing no sub-harmonics, produced large higher order m.m.f harmonics as a result of the full pitch winding. These harmonics would interact with the rotor field to produce pulsating torques. In addition, it is likely that cogging torques would result due to the reluctance variation as the rotor turns relative to the stator slots, with each rotor pole experiencing reluctance variations that are in time phase. The m.m.f. produced by stator currents in a 45 slot stator contains both sub and higher order harmonics, similar in magnitude to a 39 slot stator. The winding factor of the 45 slot winding is quite a bit lower than that of the 39 slot winding. Since this is a factor in the torque produced by the motor a corresponding increase in stator current would be required. This increase in current would lead either to higher stator I^2R losses or necessitate increased copper content. The design studies therefore, did not consider the stator slot number as a design parameter.

FIG. (6.1) FLOW DIAGRAM FOR MOTOR DESIGN PROGRAM.

START PROGRAM.
READ INPUT FROM DATA FILE
AND CONVERT TO METRIC UNITS.

CALCULATE BASIC MOTOR DIMENSIONS,
AREA OF FLUX PATHS & EFFECTIVE AIR-GAP.

CALCULATE WINDING PARAMETERS,
NUMBER OF TURNS PER PHASE, LENGTH OF WIRE
PER TURN, RESISTANCE PER PHASE, WIRE AREA
IN SLOT, SLOT FILL FACTOR, ETC.

CALCULATE AVERAGE AIR-GAP FLUX DENSITY AND FLUX
DENSITY IN VARIOUS PARTS OF THE MAGNETIC CIRCUIT
AT DIFFERENT TEMPERATURES USING MAGNET DIMENSIONS
AND MAGNETIC MATERIAL PROPERTIES IGNORING ARMATURE
REACTION EFFECT.

CALCULATE MOTOR TORQUE CONSTANT, PEAK CURRENT
AND TORQUE LEVELS AS WELL AS WEIGHT OF LAMINATIONS
COPPER ETC. CALCULATE ROTOR INERTIA AND MOTOR INDUCTANCES
AS SHOWN IN THEORY.

CALCULATE PEAK POWER OUTPUT OF THE MOTOR AND
GENERATE OPERATING CURVE DATA AT DIFFERENT MOTOR
TEMPERATURES.

CALCULATE DEMAGNETISING M.M.F. ACTING ON THE
ROTOR MAGNETS.

SEND OUTPUT DATA TO OUTPUT FILE AND PRINT.
END.

6.1.4 Influence of Pole Number on Motor Performance.

Although the number of poles in the motor was fixed, it is informative to consider the effects of varying the pole number. By considering the torque equation derived in chapter 4, the torque output of the motor increases in proportion to the number of poles. For a given stator O.D. however, the flux per pole must decrease as a consequence of magnetic saturation effects. Additionally, the frequency of flux pulsations in the stator increases in proportion to the number of poles. This will result in increased iron losses in the stator. The armature reaction effect of the stator current is inversely proportional to the number of poles. This is significant when considering demagnetisation phenomena in the rotor magnets. Therefore reduction of the pole number particularly in the case of designs using Nd-Fe-B magnets would not be desirable. An increase in the number of poles in the motor would lead to an increase in the slot number of the stator. As a result, either the tooth thickness to slot opening ratio would be reduced or smaller conductor diameters would be required.

6.1.5 Effect of Pole Arc on Motor performance.

The influence of the pole arc on motor performance can be appreciated by referring to the motor torque equation. Neglecting harmonic torque effects, the motor torque varies in proportion to the fundamental flux wave produced by the rotor magnets. The relative magnitudes of the magnet m.m.f harmonics vary with pole arc and the computer program described in chapter three was used to investigate this dependence. Tables (6.1) and (6.2) illustrate how the m.m.f. harmonics vary as the pole arc is reduced from 180° to 60°. M.m.f harmonic variations up to order 13 are shown in Plots (6.1) to (6.6).

The variation of the fundamental magnet m.m.f with pole arc is shown in Table (6.3). The amount of magnet material required, expressed as a percentage of the 180° pole arc case, is also shown. Two additional columns are included in this table containing indices that show both the fundamental m.m.f. produced per unit magnet material and the % material reduction to % m.m.f. reduction ratio. These relationships are presented graphically in Plots (6.7) to (6.10).

The choice of an optimum pole arc is governed by a number of considerations;

(a) The torque output of the motor should be maximised to give the highest power to weight ratio possible.

(b) The fundamental m.m.f. produced by the magnet per unit magnet weight should be maximised.

(c) The undesirable effects of low frequency pulsating torques should be minimised.

An inspection of the data presented in the plots indicate that a compromise value of pole arc is necessary. The original Sa–Co motor had a pole arc of 123.7° which minimises the third m.m.f. harmonic and still obtains a relatively high output torque. Furthermore, the fundamental m.m.f produced per unit magnet volume is quite good. The minimal value of third harmonic m.m.f is desirable since it reduces the third harmonic torque ripple as calculated in chapter four. However, the fifth harmonic m.m.f is quite large and as previously calculated, gives rise to a torque ripple of approximately 3.4%.

Effect of Pole arc reduction.

If the pole arc was decreased the following would result,

(1) The torque output of the motor would decrease faster than the savings in magnetic material accrue.

(2) The cross-sectional area of the motor's magnetic circuits would not decrease accordingly since the maximum flux density in the teeth will not be reduced. This would have the adverse effect of reducing the power to weight ratio of the motor.

(3) The low frequency torque ripple of the motor would tend to increase in proportion to the magnet harmonic m.m.f.s.

It is apparent that a reduction of the pole arc is undesirable,having the effect of reducing the motor's performance while leading to a small reduction in motor cost.

Effect of pole arc increase.

An increase in the pole arc of the motor would give rise to the following,

(1) The increase in motor power output does not match the increase in the amount of magnet material required.

(2) The power to weight ratio should increase slightly for similar reasons to those given in (2) above.

(3) The third harmonic torque ripple of the motor would increase but the fifth harmonic torque ripple should decrease. If the pole arc was increased to 140° the fifth harmonic ripple would be of the order of 1% while the third harmonic torque ripple would be of the order of 0.5%.

(4) Because of the grinding of the rotor diameter the minimum magnet length is reduced and the magnet edge will encounter greater demagnetising m.m.f.s. This could pose a problem for Nd-Fe-B magnets at elevated temperatures.

An increase in the pole arc appears to offer some improvement in motor performance but this needs to be offset against the increased cost of the magnets. In addition the risk of magnet edge demagnetisation is increased. The variation of torque ripple with pole arc may not be as significant as it appears here since the effects of a non–sinusoidal voltage supply also produces pulsating torques.

TABLE (6.1)

Variation of magnet harmonic m.m.f.s with pole arc

	Pole arc angle				
	180	160	140	130	123.7
Harmonic Order	Magnitude %	Magnitude %	Magnitude %	Magnitude %	Magnitude %
1	100	100	100	100	100
3	27.5	24.1	13.8	6.2	0.8
5	16.2	10.4	4.3	12.4	16.8
7	11.5	3.7	10.8	14.4	14.1
9	9.0	0.3	10.6	7.7	3.2
11	7.3	2.9	6.5	1.0	6.2
13	6.2	4.4	1.1	6.4	8.0
15	5.4	5.1	3.3	6.4	3.1
17	4.7	5.0	5.3	2.4	3.0
19	4.2	4.5	4.7	2.3	5.5
21	3.8	3.5	2.2	4.6	3.1
23	3.5	2.4	0.8	3.5	1.4
25	3.2	1.1	2.9	0.3	4.0

TABLE (6.2)

Variation of magnet harmonic m.m.f.s with Pole arc.

	Pole arc angle				
	120	110	100	80	60
Harmonic Order	Magnitude %	Magnitude %	Magnitude %	Magnitude %	Magnitude %
1	100	100	100	100	100
3	2.61	12.5	23.2	45.6	66.9
5	19.1	23.1	23.1	9.6	20.5
7	13.0	6.5	3.5	21.3	13.7
9	0.3	9.2	13.8	0.3	21.9
11	8.5	9.4	1.8	13.5	9.1
13	7.0	0.9	9.0	4.1	7.5
15	0.1	7.4	4.0	8.7	13.1
17	5.5	3.8	5.6	5.8	5.8
19	4.8	3.5	5.0	5.1	5.1
21	0.0	5.3	3.0	6.2	9.4
23	4.0	0.4	5.0	2.2	4.3
25	3.7	4.2	0.9	5.9	3.9

TABLE (6.3)

Pole arc influence on various motor parameters.

Pole Arc Angle	Mag. Fundamental m.m.f.		Material Required	m.m.f per Mat'l	-% Mat per -% mmf
	% of max	% reduced	%		
180	127.0	—	100.0	1.27	—
160	125.0	1.6	88.9	1.41	6.94
140	119.5	5.8	77.7	1.54	3.84
130	115.4	9.1	72.7	1.59	3.00
123.7	112.0	11.8	68.7	1.63	2.65
120	110.0	13.4	66.7	1.65	2.49
110	104.0	18.1	61.1	1.70	2.15
100	97.5	23.2	55.6	1.75	1.91
80	82.0	35.4	44.4	1.85	1.57
60	64.0	49.6	33.3	1.95	1.34

Note: The data in column two is given as a percentage of the actual magnet m.m.f and is calculated using Fourier Series analysis. In this instance the magnet m.m.f. distribution was considered to be rectangular and the change in magnet m.m.f. distribution as a result of grinding the rotor diameter was ignored

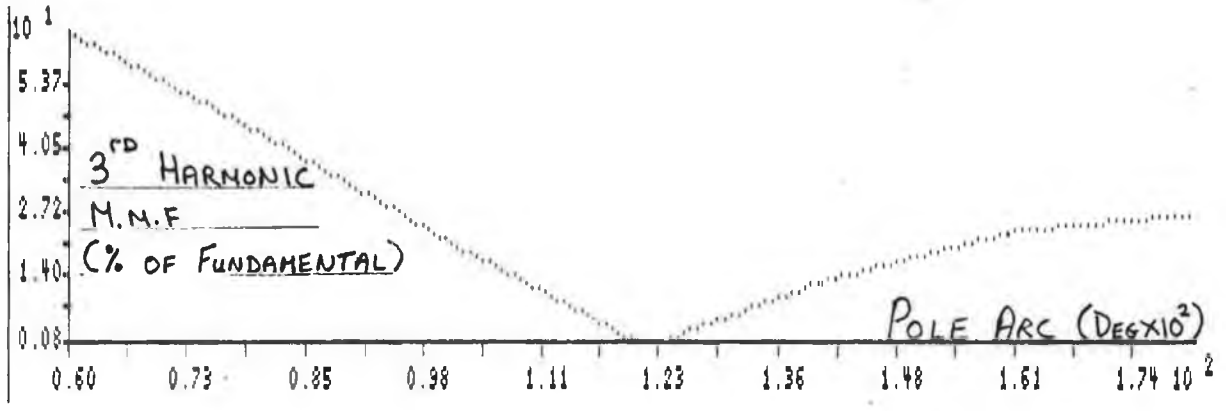

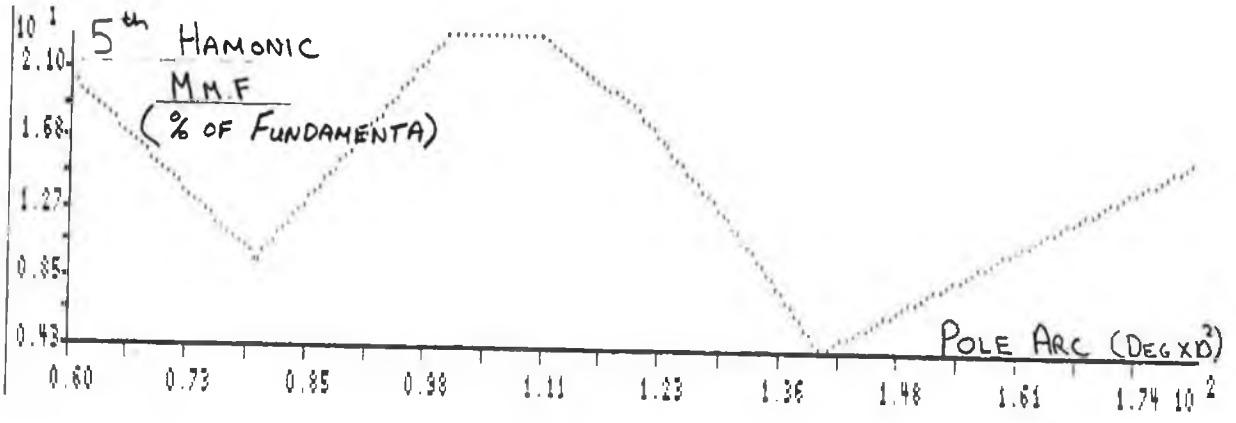

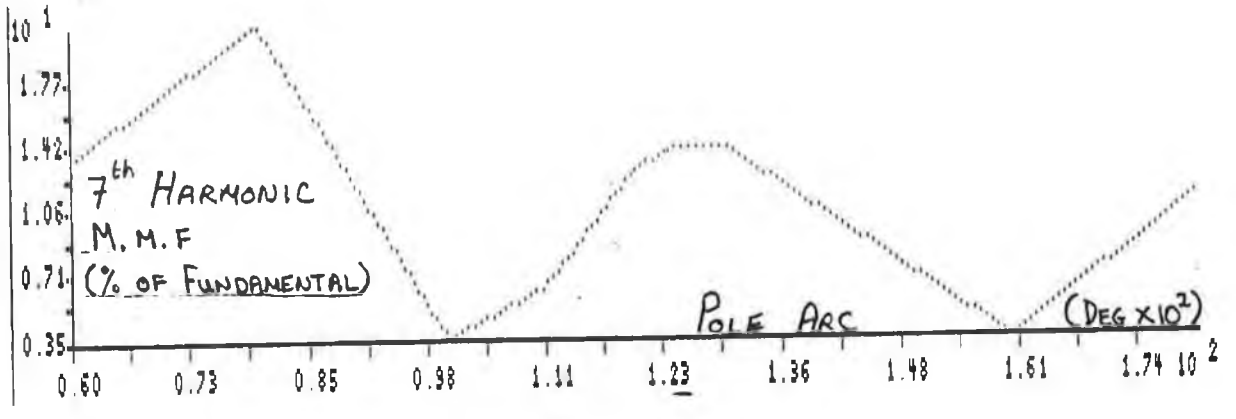

Plots (6.1) to (6.3) indicating the harmonic m.m.f variations as the pole arc changes from 180° to 60°.

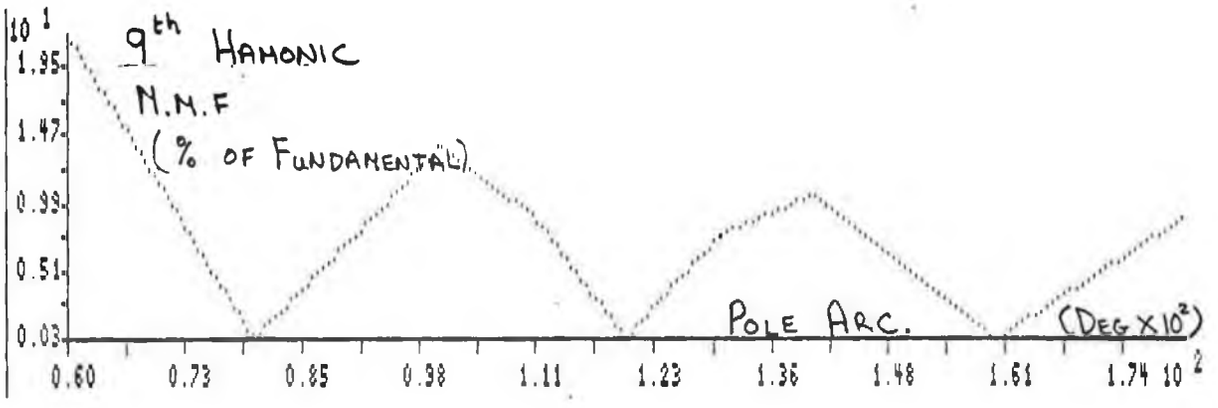

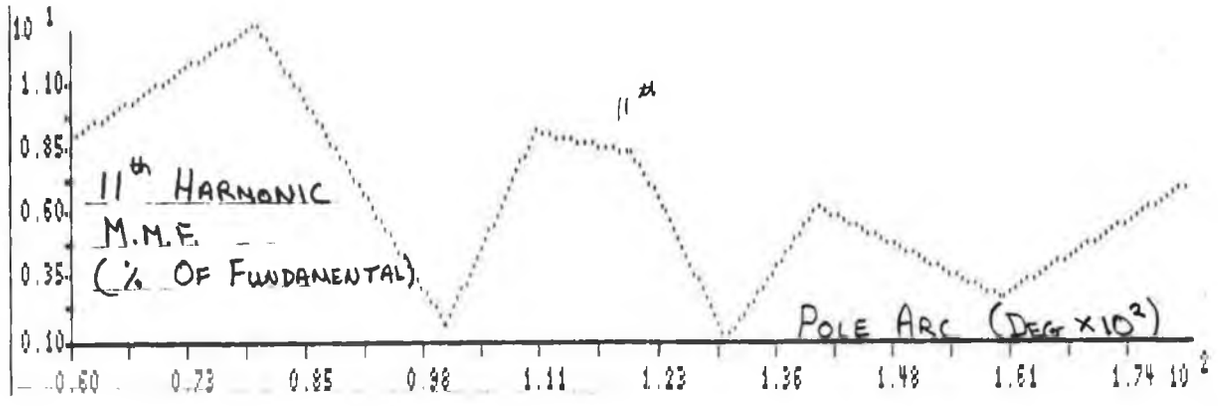

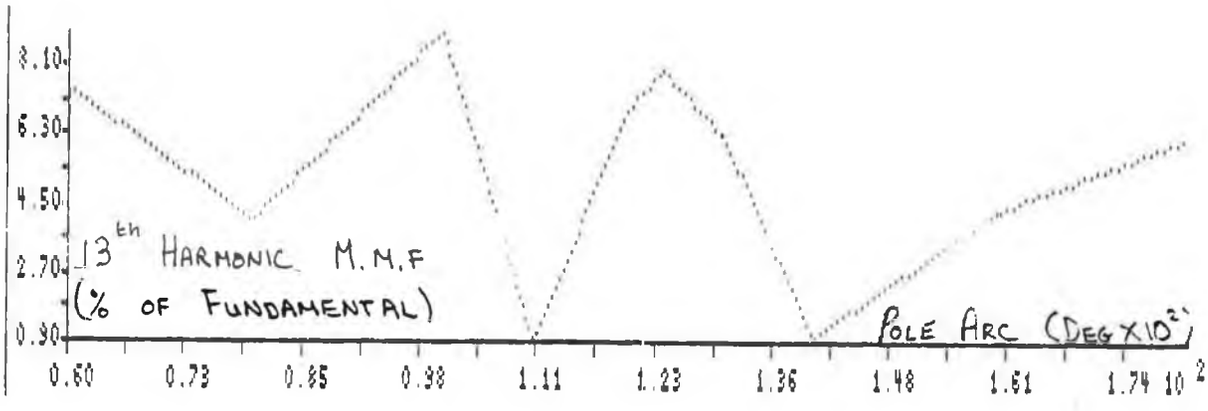

Plots (6.4) to (6.6) indicating the harmonic m.m.f variations as the pole arc changes from 180° to 60°.

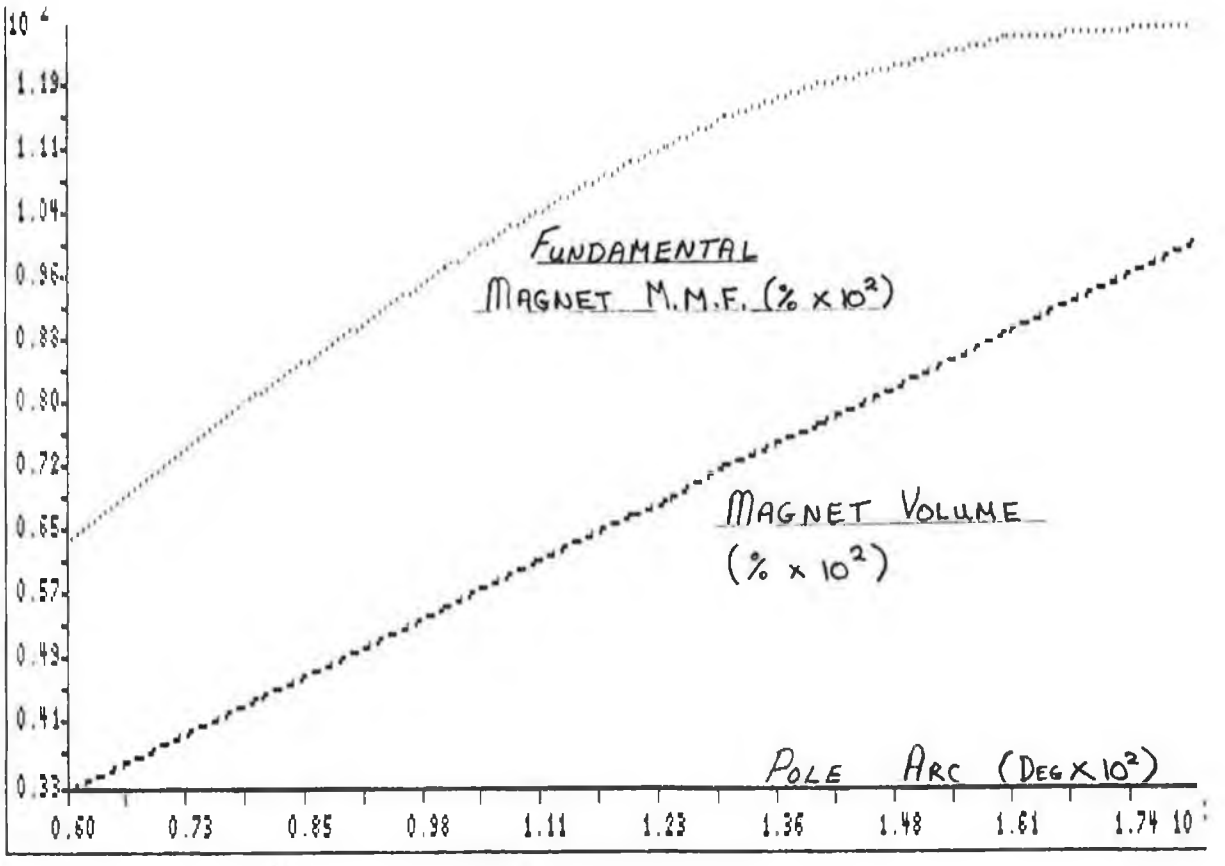

Plots (6.7) Fundamental Magnet m.m.f. and Magnet Volume variations with Pole Arc.

Plots (6.8) Reduction of Fundamental Magnet m.m.f. with Pole Arc.

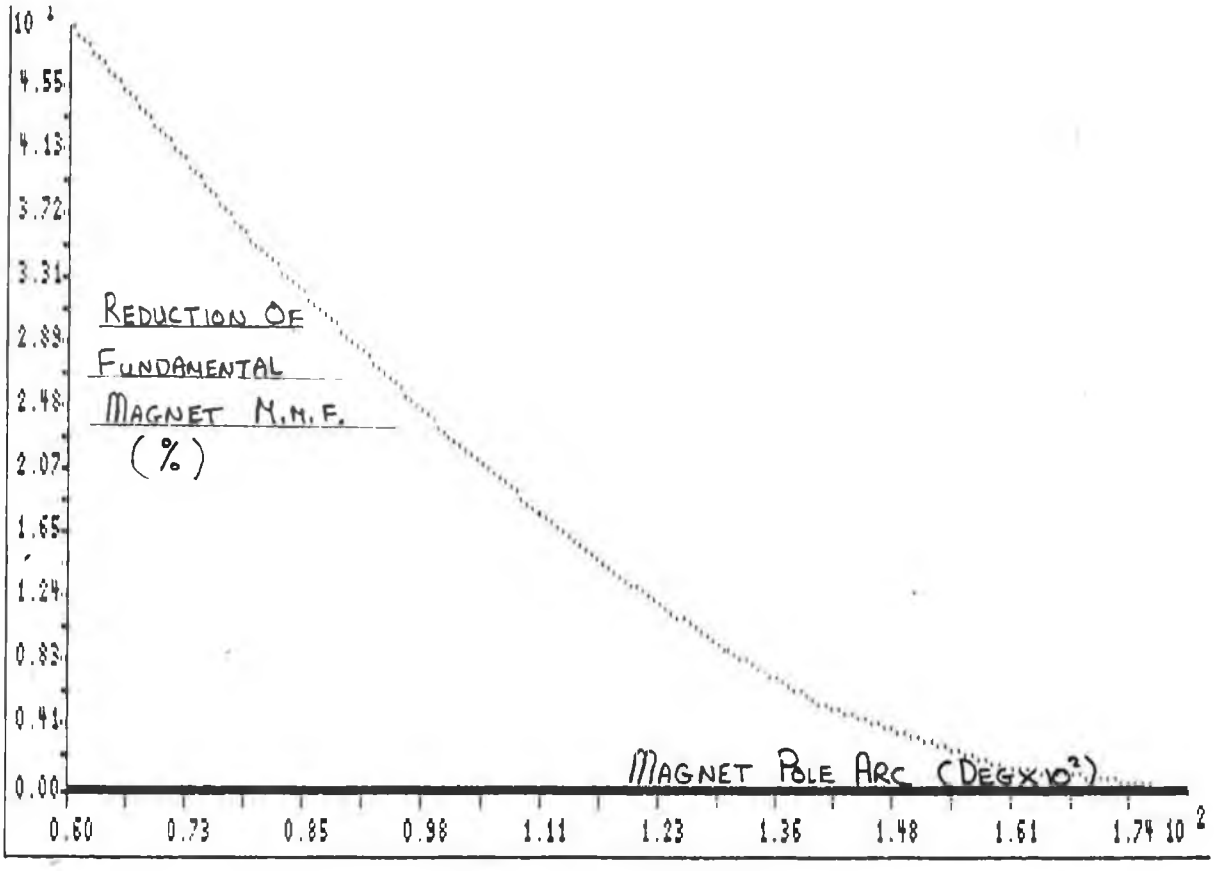

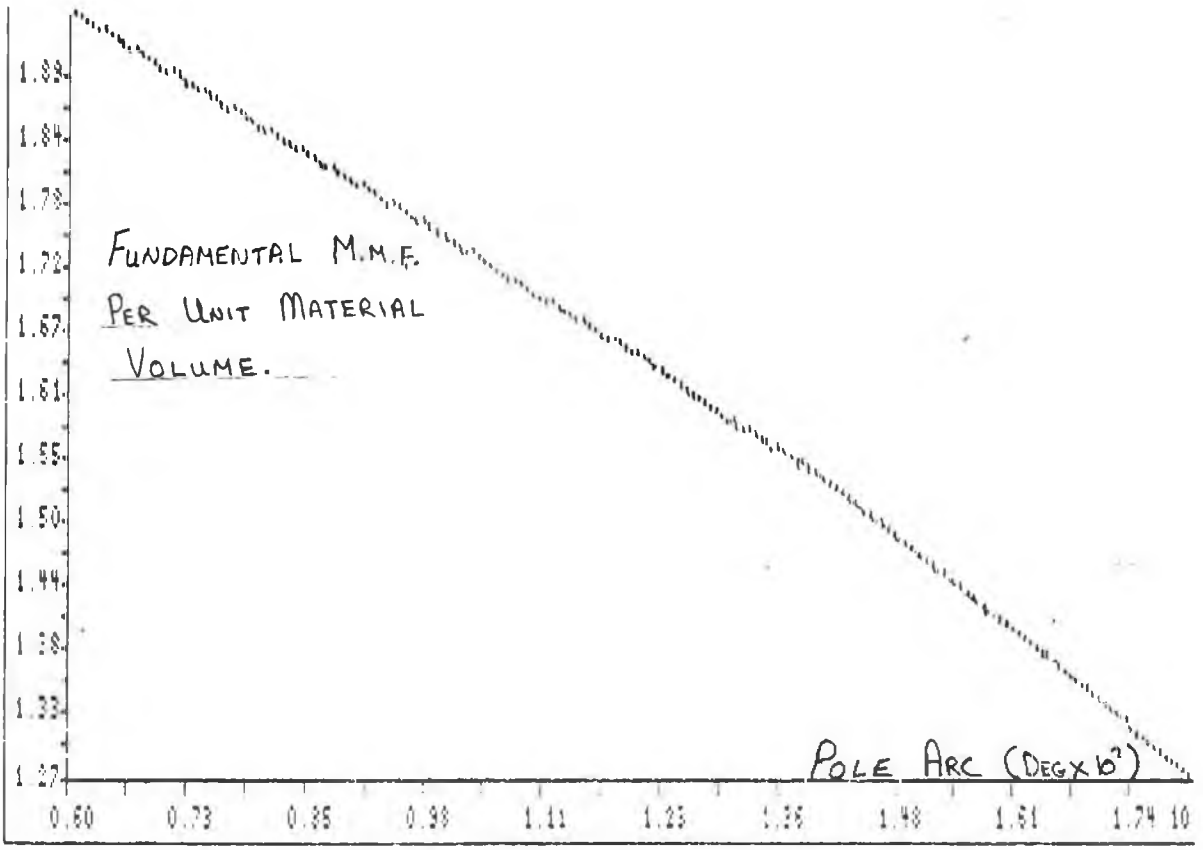

Plots (6.9) Fundamental Magnet m.m.f. per unit Magnet Volume versus Pole Arc.

Plots (6.10) Material Volume Reduction per Fundamental Magnet m.m.f. versus Pole Arc.

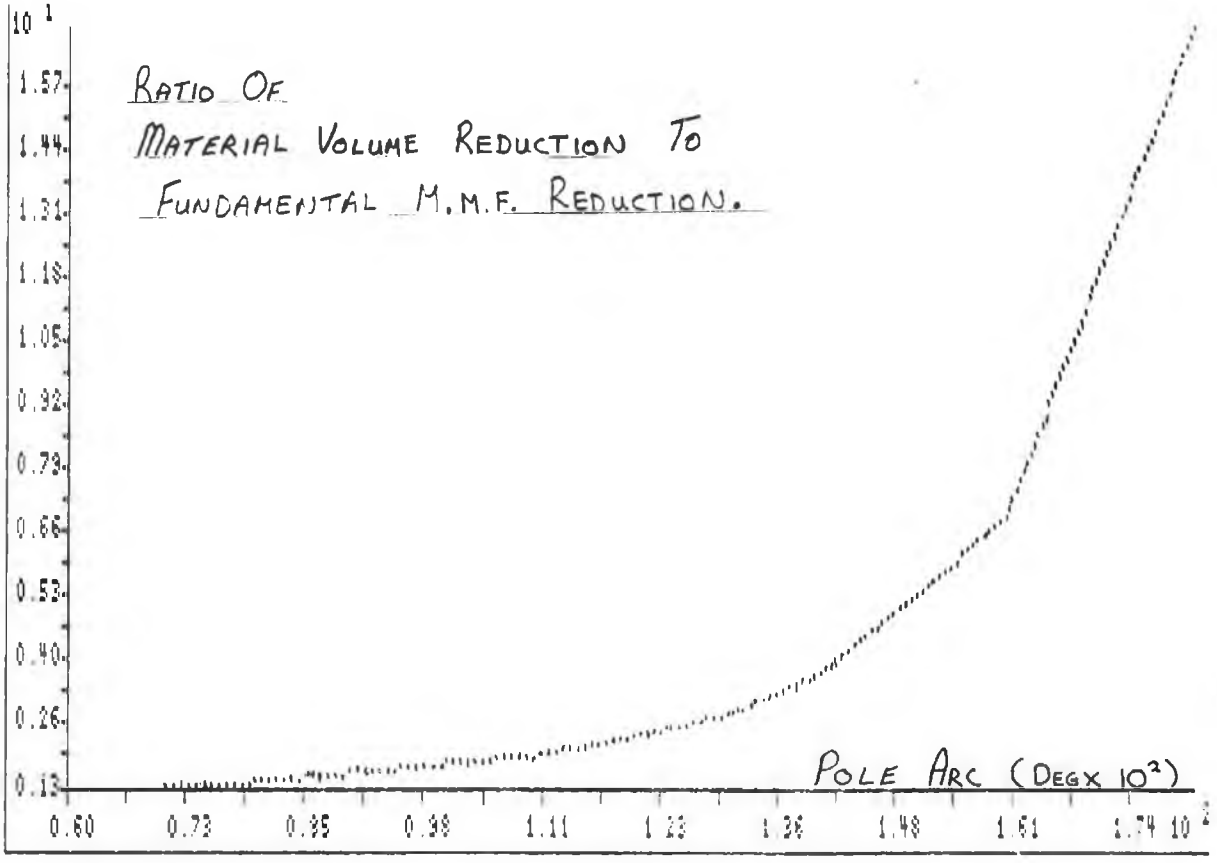

6.2 DESIGN STUDIES AND SUMMARY OF RESULTS.

6.2.1 Design Studies.

In these studies a number of Nd-Fe-B material grades were considered as replacement materials for Sa-Co. The demagnetisation curves and other technical data for these materials are contained in appendix (G). In order to make a quick comparison between these materials, Table (6.4) presents their most important magnetic properties at room temperature and at 125°C. This table illustrates quite clearly the different temperature characteristics of Nd-Fe-B and Sa-Co magnets.

TABLE (6.4)

Material	Energy Product (MGOe)		Residual Induction (Tesla)		Coercivity (kA/m)	
	25°C	125°C	25°C	125°C	25°C	125°C
Sa_2–CO_{17}	26.0	21.5	1.06	1.02	743.1	711.5
NEIGT 35H	35.5	25.0	1.23	1.08	919.4	490.0
NEIGT 30H	30.0	22.5	1.13	1.00	838.0	553.0
NEIGT 27H	27.0	21.0	1.04	0.95	751.0	679.9
CRUMAX 355	35.0	26.0	1.23	1.10	893.3	316.2
CRUMAX 322	32.0	22.0	1.16	1.01	853.8	632.5
CRUMAX 301	30.0	24.0	1.10	1.00	838.0	632.5
CRUMAX 261	26.0	21.5	1.03	0.94	790.6	648.3

6.2.2 Design Study (1).

A design study utilising different Nd-Fe-B grades was carried out and the results of this study are summarised in Table (6.5). The following considerations and restrictions apply to this performance data,

(1) The problem of magnet demagnetisation at high temperatures was ignored although the effect of temperature on the Induction of the material was included in the study. This study would then indicate the possible improvement in motor performance obtainable with Nd-Fe-B materials assuming the problem of low coercivity at high temperatures could be solved.

(2) Designs presented in Table (6.5) attempted to obtain the best performance possible using different magnet materials while maintaining the original rotor diameter.

(3) Each of the designs use approximately the same volume of magnets to allow fair comparison of the materials. Since the density of Nd-Fe-B is approximately 90% that of Sa-Co the actual weight of magnets used in the redesigns is less.

(4) The magnet temperature is shown at the top of the columns in Table (6.5).

(5) In the case of the original Sa-Co motor the magnetic properties as presented in the data curves were derated by approximately 5% to take account of property variations. This has not been done in the case of the Nd-Fe-B designs and the uprated Sa-Co design was included to allow comparison on an equivalent basis.

TABLE (6.5)

Summary of Calculated Motor Performance Parameters.
(Temperatures quoted apply to rotor magnets.)

Magnet Material	Rotor Diameter (cm)	Torque constant K_t 25°C	70°C	109°C	Max Pow. Rate 70°C	Max Acc. Theor. 70°C	Motor Con. 25°C
$Sa\text{-}Co_{17}$	5.18	0.559	0.551	0.543	2070.9	87949	0.4568
$Sa\text{-}Co_{17}$	5.18	+6.0%	+6.0%	+5.0%	+10%	+5.0%	+5.0%
		(Turns per coil = 13)					
Nd-Fe-B							
(27H)							
# 1A	5.18	+3.0	+0.0%	-3.0%	+4.0%	+3.5%	+3.0%
(30H)							
# 1B	5.18	+4.0%	+0.5%	–3.0%	+5.0%	+4.0%	+5.0%
		(Turns per coil reduced to 12.)					
(35H)							
# 2C	5.18	+6.5	+1.0%	-2.0%	+6.5%	+5.0%	+10%
		(Turns per coil reduced to 11.)					
(Crumax 301)							
# 1D	5.18	+4.0%	+2.0%	-0.2%	+8.0%	+6.0%	+4.0%

Discussion.

On inspecting Table (6.5) the following points are apparent,

(1) The Nd-Fe-B designs will perform better than the original Sa-Co motor at room temperature.

(2) As the temperature of the magnets increase the relative performance of the Nd-Fe-B designs disimprove. It is seen that for magnet temperatures in the region of 70 to 109 °C the torque output of all the Nd-Fe-B designs are less than the original Sa-Co motor.

(3) In the case of the Neodymium grades with high energy products the number of winding turns have been reduced to match the operating speed range of the motors at winding temperatures of 100 °C. This has the effect of lowering motor I^2R losses and improving the motor constant K_m.

(4) It is clear that the performance of the up-rated Sa-Co design is better than any of the Nd-Fe-B designs. However, improved power output could be obtained using Nd-Fe-B designs with a greater number of turns.

From the above observations it is clear that a motor design utilising Nd-Fe–B magnets cannot match the performance of a Sa-Co design exactly due to a greater change in magnetic induction with temperature. If the Neodymium design is to perform equally to the Sa-Co design on a continuous rating basis at temperatures in excess of 100 °C then by necessity it will have to have a larger K_t at room temperature.

6.2.3 Design Study (2).

This study was also subjected to similar restrictions and considerations as Design study (1) but the effects of rotor diameter variations were also investigated. A summary of the results of this study is presented in Table (6.6). The magnet temperatures applying to the second set of data for a design are given in brackets at the top of the appropriate columns.

TABLE (6.6)

Summary of Calculated Motor Performance Parameters.

(Temperatures quoted apply to rotor magnets.)

Magnet Material	Rotor Diameter (cm)	Torque constant K_t 25°C	70°C (87°C)	109°C (135°C)	Max Pow. Rate 70°C (87°)	Max Acc. Theor. 70°C	Motor Con. 25°C
$Sa\text{-}Co_{17}$	5.18	0.559	0.551	0.543	2070.9	87949	0.4568
$Sa\text{-}Co_{17}$	5.18	+6.0%	+6.0%	+5.0%	+10%	+5.0%	+5.0%
Nd-Fe-B (30H)		(30H designs have 12 turns per coil)					
# 1B	5.18	+4.0%	+0.5%	–3.0%	+5.0%	+4.0%	+5.0%
# 2B	5.18	+4.0%	+1.0%	-3.0%	-6.0%	-1.5%	+2.0%
		(#2B has reduced wire area)					
Nd-Fe-B (35H)		(35H designs have 11 turns per coil)					
# 1C	5.31	+7.5%	+3.0%	-0.5%	+0.0%	-3.0%	+12%
# 2C	5.18	+6.5%	+1.0%	-2.0%	+6.5%	+5.0%	+10%
# 3C	5.05	+4.0%	-0.5%	-4.0%	+14%	+14%	+8.5%
# 4C	4.93	+1.5%	-2.5%	-6.0%	+22%	+25%	+6.5%
		+1.5%	-4.0%	-9.0%	+17%	+22%	—
# 5C	4.80	-0.5%	-4.5%	-8.0%	+30%	+36%	+4.0%
# 6C	4.67	-2.5%	-6.5%	-10%	+39%	+48%	+2.0%
		-2.5%	-8.0%	-13%	+33%	+45%	—
# 7C	4.67	-3.5%	-7.5%	-11%	+35%	+46%	+0.5%
		(#7C has 5% less magnet volume)					
Nd-Fe-B (CRUMAX 301)							
# 1D	5.18	+4.0%	+2.0	-0.2%	+8.0%	+6.0%	+4.0%
	5.18	+4.0%	+1.0%	-2.0%	+6.0%	+5.0%	—
Nd-Fe-B (CRUMAX 322)		(322 Designs have 11 Turns per coil)					
# 2D 322	5.05	-2.5%	–6.5%	-10%	+9.0%	+12%	+1.5%
		-2.5%	-8.0%	-13%	-4.0%	+4.8%	—
Nd-Fe-B (CRUMAX 355)		(355 Designs have 11 turns per coil)					
# 3D	4.93	+2.5%	-0.5%	-4.5%	+24%	+26%	+6.5%
		+2.5%	-2.5%	-7.0%	+21%	+24%	—

Discussion.

The following are the main points to be drawn from this study,

(1) It is seen that the torque output of the motor is reduced as the rotor diameter decreases. This can be understood by considering that the torque output of the motor is proportional to the magnet flux per pole. As the rotor diameter decreases the area of each rotor pole is reduced assuming that the pole arc is unchanged. In order to maintain the flux per pole constant an increase in the magnet flux density is necessary, leading to increased air-gap and Iron flux path magnetic flux densities. Magnetic saturation prevents the designer from compensating fully for the reduction in magnet area with increased m.m.f. drops along the iron flux paths..

(2) Because of the reduction in the inertia of the rotor, the acceleration rates and maximum power rates of the Neodymium designs increase rapidly with decreasing rotor diameter. On the other hand the motor constant decreases due to the lower torque output of the motor. An increase in rotor diameter was not investigated since the rapidly increasing rotor inertia would lead to a decrease in the acceleration rate and maximum power rate of the motor. In addition the magnet length at the rotor pole edges would be decreased increasing the risk of demagnetisation.

6.2.4 Selection of Prototype design.

Having investigated these designs in detail it was decided to select one of them and build a prototype motor using Nd-Fe–B magnets. Initially it was decided to build a motor using the dimensions of # 4C because it offered the possibilty of reasonable torque output and high acceleration rates. However when an attempt was made to order the magnet material the lead time required to procure the magnets was approximately one year. In any event an investigation into the demagnetising effect of stator currents indicated that under peak current and temperature conditions demagnetisation at the magnet edges would occur.

Design # 3D was very similar to design # 4C and this material is manufactured by Crucible Magnets. When the specification for this material was examined it revealed that the Irreversible losses at 100 °C would be approximately 15%. Thus once the magnets had been subject to 100 °C for more than two hours in a motor application its residual magnetism would have decreased to 1.04 Tesla at room temperature. If the temperature of the magnet was increased to more than 100 °C then the reduction in magnetism would have been far greater. Obviously this ruled out the use of this material in class F servo-motors.

The percentage change in induction due to Irreversible losses for Nd-Fe-B magnet materials supplied by Crucible Materials Corporation are shown in Fig. (6.1). From this graph it is evident that the irreversible losses are not the same for all grades of the Crumax material being least for Crumax 261 and 301.

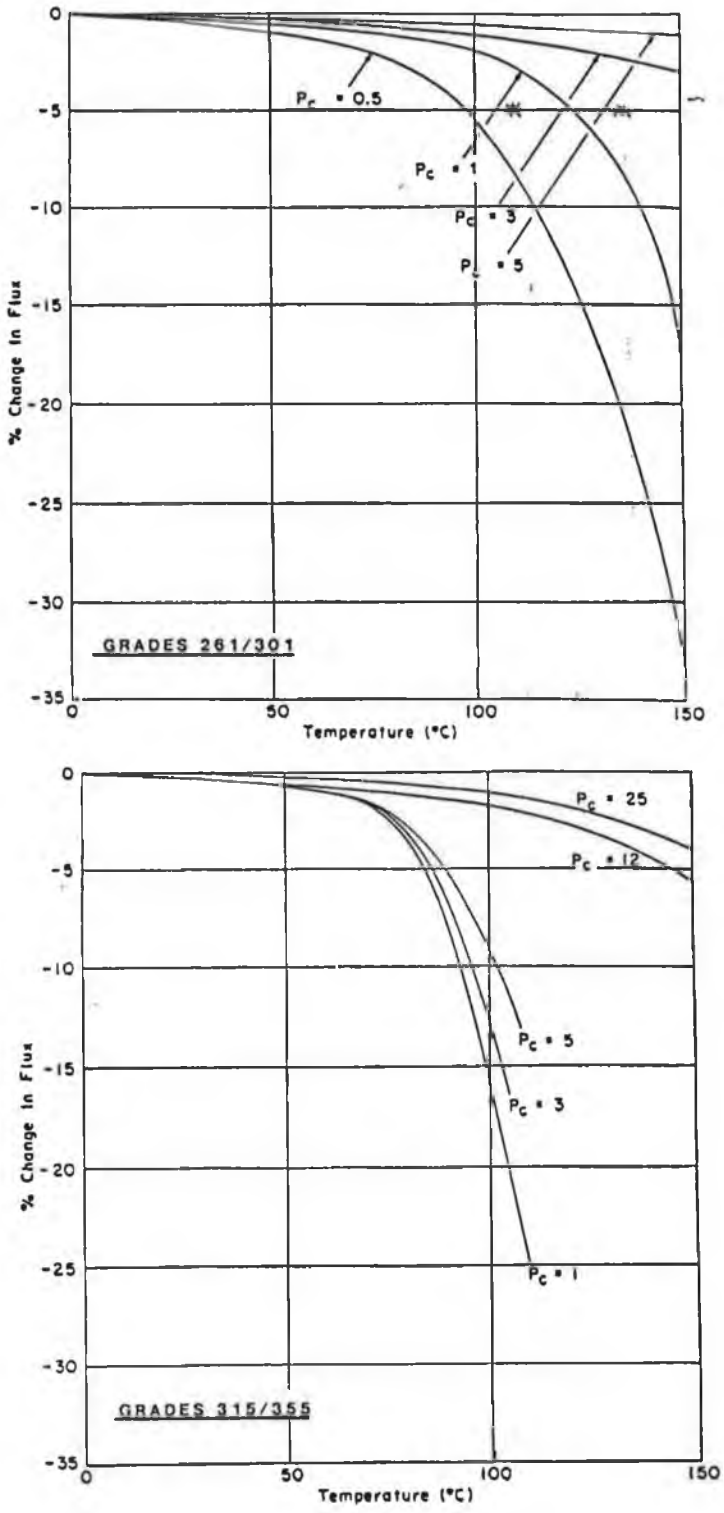

Fig (6.1) Variation of Irreversible losses for Crumax materials with magnet temperature and slope of circuit permeance coeficient, PC.

6.2.4 Discussion of Prototype Motor design.

A prototype Nd-Fe-B motor design using the standard Moog stator assembly was built. This approach was taken in order to reduce the time required to build the motor. It is unlikely that an optimum motor design results from this approach. Nevertheless important information could be gathered about the behaviour of the material in an actual motor application.

Design # 1D in Tables (6.5) and (6.6) uses the same stator and rotor dimensions as the original Sa-Co motor and uses Crumax 301 magnet material. This material was chosen because of it has relatively low Irreversible losses. The design incorporates a 5.0 % loss in Induction levels in the material to account for these losses. Taking this loss into account the performance of the motor is quite close to that of the original motor. The following are the main attributes of the Nd-Fe-B redesign,

(1) The volume of magnet material used in the redesign is approximately 2.0 % less than that used in the original motor. Taking the density of the material into account this leads to a decrease in magnet weight per motor of approximately 12.0 %.

(2) The air-gap of the motor was increased from 0.762 mm to 0.838 mm in an attempt to obtain similar high temperature performance in the two motors.

(3) The Irreversible losses of the design were calculated based on the material specifications, the expected maximum continuous magnet temperatures and the corresponding magnet operating point in the second quadrant. The maximum continuous magnet temperature was taken to be 135 °C based on the steady state heating test performed on the motor and on the maximum average winding temperature rise of a class F motor. The minimum operating point of the magnet occurs at the magnet edges due to the armature reaction of the stator currents. The peak of the Fundamental m.m.f. wave in ampere turns is 25.45 times I_{peak} for the 39 slot winding. This was determined from the winding analysis in chapter 3. This value can also be calculated using the following formula [Ref. 10],

$$\text{Peak m.m.f} = \frac{2.q.M.n.K_p.K_d.I_{pk}}{\pi}$$

where M is the ampere turns per coil.
q is the number of phase belts per pole.
n is the number of slots per phase belts.
K_p,K_d are the winding pitch and distribution factors.
I_{pk} is the peak current per phase.

Applying this to the Moog motor the peak m.m.f. as a result of the maximum continuous stator current is 252 ampere turns peak. Assuming that the magnet and stator fields are at right angles to yield maximum torque the fundamental m.m.f. acting across the air-gap at the magnet edge is 222 ampere turns. This is equivalent to the application of a demagnetising field of 66.97 x 10^3 ampere turns per metre of magnet length (0.84 kOe) ignoring the air-gap. Using the graphical methods to determine the effect of a demagnetising field as described in chapter 2. it is found that the operating flux density in the magnets at 135 °C is approximately 0.68 T. This is equivalent to having a circuit permeance slope of 2.5 and the resulting Irreversible loss should be less than 4.0 %.

The effects of stator slots on the circuit permeance were not accounted for since the manufacturer claims that a soaking period of one to two hours are necessary before Irreversible losses occur. The slots will have the effect of causing rapid fluctuations in the magnet operating point due to the variable air-gap permeance and it is possible that these could cause additional flux loss. To determine the operating point of the magnet accurately under these conditions would require the use of a flux plotting Program.

(4) Consideration was also given to standard Demagnetisation phenomena that occur as a result of the magnet operating beyond the "Knee" of the demagnetisation curve. It was calculated that under peak current conditions that a peak fundamental demagnetising field of 1100 ampere turns would act across the air-gap. This is equivalent to a demagnetising field of 291 x 10^3 ampere turns per metre length of magnet (3.63 kOe) neglecting the air-gap. On inspection of the second quadrant characteristic of Crumax 301, the magnet will be operating along the linear portion of the curve at 135 °C. Therefore no additional flux loss should occur under these conditions.

If tests indicated that the motor continuous torque was less than that of the Sa-Co motor an improvement of the order of 3% could be readily obtained if the air-gap of the Nd-Fe-B design was reduced. Continuous load tests at various temperatures should also indicate the extent of the Irreversible losses in the motor. These should help determine the maximum temperatures at which Crumax 301 material can be used in servo-motor applications.

6.3 TESTS ON THE NEODYMIUM MOTOR PROTOTYPE.

6.3.1 Measurement of motor back e.m.f constant.

This test consisted of driving the motor as a generator and measuring the open circuit terminal voltage. The measured voltage at 104.7 rads/s (1000 rpm) was 65.0 volts peak. Using the motor program the predicted voltage constant of the motor was 0.62 volts per rads/s at room temperature. Thus the calculated terminal voltage at 104.7 rads/sec was 64.9 volts peak. It was expected that the measured voltage would be a few percent higher since the program incorporated a 5% decrease in magnet induction levels. This was done to account for expected Irreversible magnet flux loss under motoring conditions. The accuracy of the program may have been responsible for this result.

6.3.2 Experimental verification of Residual Induction variation with Temperature.

This test consisted of heating up the motor assembly by applying a three phase supply to the stator windings. The motor assembly was lagged to prevent rapid temperature loss when the voltage supply was disconnected and to force the temperature of the rotor to rise. The temperature of the motor casing was measured with a fixed thermocouple and a thermocouple probe was used to measure the temperature of the rotor magnets and the stator end windings. The motor assembly was coupled to a standard D.C. drive motor and when it had reached the required temperature was driven as a generator. The generated voltage at different rotor temperatures was measured as was the percentage generated voltage change and these results are presented in Table (6.7). In addition to obtaining data regarding the change in Residual Induction, the motor assembly was allowed to return to room temperature after each test. This was done in an effort to evaluate if any Irreversible losses occurred as a result of the heating process.

TABLE (6.7)

Material	Temperature °C	Calculated Br % change Specs.	Program	Generated Voltage measured	% change
Sa-Co	23.1	—	—	62.17	—
	70.3	-1.4	-1.3	61.41	-1.2
Nd-Fe-B	19.5	—	—	64.56	—
	75.0	-4.8	-4.2	61.74	-4.4
	18.1	+0.1	—	64.49	-0.1
	110.0	-8.1	-7.1	59.83	-7.3
	17.5	+0.2	—	64.57	+0.0
	109.0	-8.0	-7.0	59.94	-7.2
	19.3	+0.0	—	64.34	-0.3

6.3.2 Discussion of test results

According to the manufacturer's data Irreversible losses occur as a function of the operating point of the magnet and it's temperature over an extended period of time. Using the motor design program to predict the operating point of the magnet and the manufacturer's curves to calculate the Irreversible losses, it appears that an Induction loss of 0.75% over a period of two hours could be expected. The actual measured loss in Induction is of the order of 0.3% but since the magnets were not exposed to the maximum temperatures for more than an hour, further loss of Induction could still occur. Additional heating tests were not carried out since the magnets were stationary during the heating process. Thus they were subject to a permeance wave that was fixed relative to the magnet edges which could lead to Irreversible losses that would not occur under normal operation as a motor. It is unclear in the manufacturer's literature if rapid permeance variations due to the stator slots would lead to Irreversible losses over an extended period of time e.g. two or more hours. Furthermore the exact operating point of the magnet would need to be determined, using perhaps a Finite Element analysis package, when it is opposite a stator tooth and when it is opposite a slot.

The calculated change in residual induction levels in the magnets based on the manufacturers specifications are also included in the table. The change in voltage which should be proportional to the Residual Induction of the magnets is seen to be somewhat less than that calculated from the material specifications. This may be explained by considering the fact that the magnetic circuit of the motor is slightly saturated at room temperature. As the Residual Induction of the magnets fall the saturation level in the magnetic circuit decreases and the overall circuit reluctance is reduced. Thus the actual drop in air-gap flux is less than that calculated from the magnet specifications alone. The design program calculates the voltage constant of the motor taking saturation into account and if the change in K_e with temperature is compared with the measured change in generated voltage they are found to correspond closely.

6.3.3 Motor Continuous Performance Tests.

Motor load tests were carried out to compare the performance of the Nd-Fe-B prototype motor with the standard Sa-Co motor design. These tests were carried out at Moog's test facility in Germany. This was done so that comparative data for the two designs was obtained on one test rig. In addition test facilities to accurately measure motor output torque were not available at the N.I.H.E, Dublin.

Figure (6.2) presents motor performance data for both the Nd-Fe-B and Sa-Co motors. These tests were obtained by loading the motor in such a way as to achieve a constant winding temperature. The curves in the figure apply to the Sa-Co motor for winding temperatures of 85°C, 125°C and 140°C. Comparative data for the Nd-Fe-B corresponding to winding temperatures of 85°C and 125°C are indicated by circles. On inspection of the 85°C data it is seen that the output torque of the Nd-Fe-B motor is slightly greater than that of the Sa-Co design. At a winding temperature of 125°C however the torque output of the two motors is almost identical. This is probably due to the greater change of magnet Induction levels in Nd-Fe–B material with temperature. As predicted in the design study the continuous performance of the two motors is very similar.

Predicted continuous performance data for both designs was also obtained from the motor program and in figure (6.3) the results are compared with test data on a Sa-Co motor. The program calculated the continuous performance by using a value for the temperature rise of the motor per unit watt loss and by calculating the winding I^2R and magnetic circuit losses. An inspection of figure (6.3) indicates

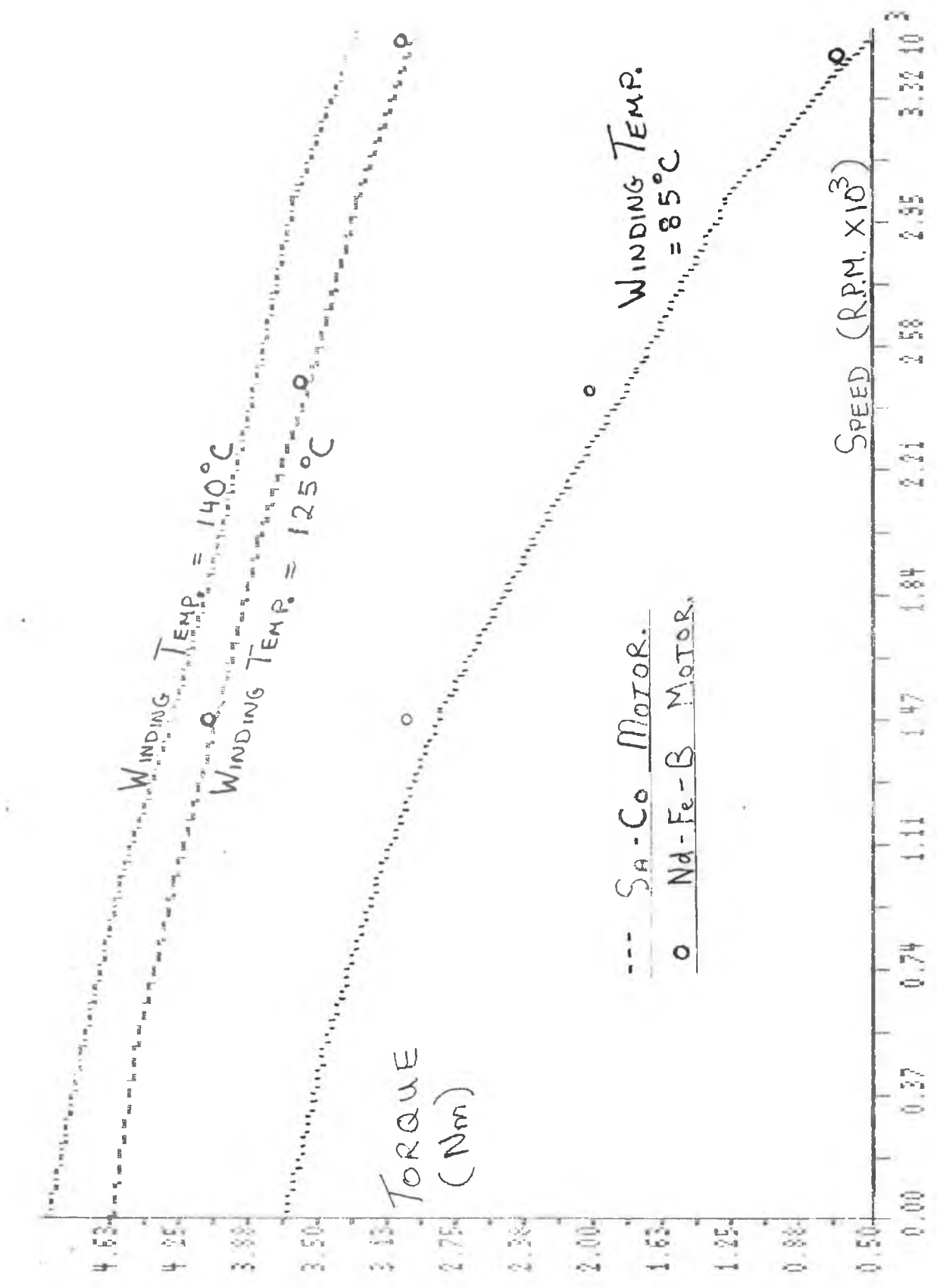

Figure (6.2) Continuous operating data for Sa-Co and Nd-Fe-B motors at various winding temperatures.

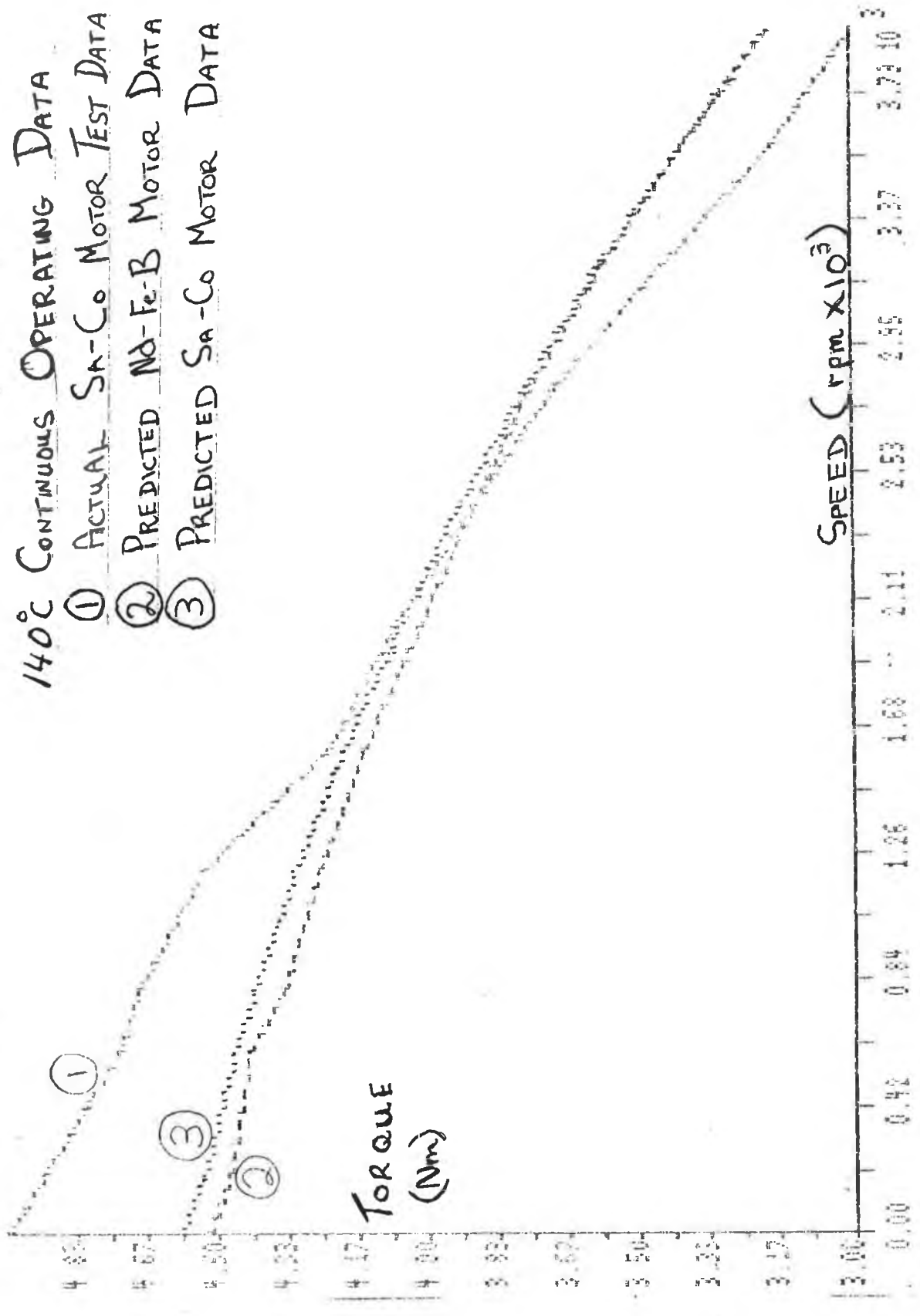

Figure (6.3) Measured and predicted performance data for Sa-Co and Nd-Fe–B motors with a continuous winding temperature of 140 °C.

that this thermal model of the motor is not very precise. There are a number of reasons for the inaccuracy of the model,

(1) No attempt is made to account for the I^2R heating effects of the harmonic current components.

(2) As the motor speed increases the frequency of all the current components except those at multiples of the carrier frequency increase. This will increase the winding losses as a result of skin effects [Refs. 17, 25].

(3) The increase in winding temperature leads to an increase in winding resistance and hence motor losses.

(4) The temperature rise of the motor per unit watt loss varies with changes in the temperature difference between the motor and it's surroundings.

The predicted continuous performance in figure (6.3) indicates that the performance of the Sa-Co design is better than the Nd-Fe–B prototype at winding temperatures of 140°C. This corresponds to magnet temperatures in the region of 120°C. Consideration of the different temperature coefficients of Induction of the two materials would explain this.

6.3.4 Irreversible Flux loss measurements.

The Nd-Fe-B prototype motor voltage constant at 25°C was measured after each of the continuous performance tests. No change in this constant was noted, indicating that no Irreversible flux losses had occurred. The motor was then operated continuously for more than two hours with a winding temperature of 167°C. The corresponding magnet temperature was 139°C. After the magnets had cooled down to room temperature the motor voltage constant was again measured. No change in the motor voltage constant was noted.

Discussion.

It was expected that a loss in induction would occur when the magnets were operated on a continuous basis at 135°C. However this did not appear to have occurred. Possible explanations for this are as follows,

(1) Some Irreversible losses may have already occured prior to motor testing. These could have been due to the handling of the magnets at the manufacturing stage or when the rotor diameter was being ground.

(2) The manufacturer's data with regard to Irreversible losses may have been conservative.

(3) The operating flux levels in the magnets predicted by the motor program may have been pessimistic. The use of a Finite Element Analysis program would yield more accurate information on the magnet operating flux levels.

Further investigation of the Flux losses are planned by Moog Ltd with the motor subject to the demagnetising effects at peak current levels. However since these current levels can be sustained for less than a minute Irreversible losses should not occur. Because of the time factor involved in obtaining this data no results are available.

Chapter 7.

CONCLUSION.

This research considered all the major aspects of A.C. Brushless servo-motor design using Neodymium Iron Boron magnets. The characteristics of Neodymium Iron Boron permanent magnet material were discussed vis a vis Samarium Cobalt material. The two most important characteristics from an applications point of view are the residual induction and the coercivity of the magnets. It is seen that these properties vary quite significantly with temperature and that care must be taken when using the material in applications where the magnet temperature exceeds 100°C. Not all grades of Neodymium Iron Boron material exhibit the same degree of property changes and careful judgement in selecting the optimum material grade is required. A magnetic circuit model of the motor was developed and used to predict the flux density levels in the air-gap of the motor. When predicted and measured motor voltage constants were compared the accuracy of the modelling was shown to be good.

A method of winding analysis was introduced which predicted the magnitudes of the fundamental and harmonic m.m.f.s based on the winding layout of the motor. A computer program was written to perform this analysis for any three phase winding. The validity of this analysis was proved experimentally by measuring the induced harmonic voltages when the motor was operating as a generator. Alternative winding configurations to that presently used by Moog Ltd were designed and investigated with the aid of the computer program.

An expression for the motor torque incorporating all the design parameters was derived. A method of predicting pulsating torques based on the winding m.m.f analysis previously mentioned and on the magnet m.m.f. harmonics was presented. An investigation into the effect of changing the slot number was performed. This investigation confirmed the superiority of a thirty-nine slot stator over either a thirty-six or a forty-five slot stator in the case of a twelve pole, three phase motor arrangement.

Expressions for the motor direct and quadrature axis reactances were developed and used to investigate the magnitude of the reluctance torque component in the Moog motor. The peak value of the reluctance torque was shown to be less than 5% that of the torque component due to the magnets. The contribution of this

component to motor torque at a torque angle of 90° was shown to be negligible. Formulae to calculate the stator leakage reactances were presented. These formulae were used to calculate the inductance of the stator. Experimental measurements indicated that calculated values for motor reactances are too low if the magnets are absent from the air-gap. With the magnets present in the air-gap however, the calculatedvalues for motor reactances are too high. These measurements emphasise the effect that magnetic saturation due to the rotor magnets has on the motor reactances. The use of a Finite Element Analysis package should improve the correlation between predicted and measured motor reactances.

The effects of a nonsinusoidal voltage supply on motor performance and losses were discussed. Motor heating tests were performed to establish the relative magnitudes of stator and rotor losses. Significant conduction of heat across the air-gap from stator to rotor was noted. This showed that rotor self heating effects are not an important consideration when choosing a permanent magnet material.

An investigation into the influence of pole arc as a design parameter proved informative. It was seen that careful selection of this parameter could help to minimise low frequency torque ripple. Use of a pole arc in excess of 140° was shown to yield little improvement in motor output power and lead to a reduction in the ratio, fundamental magnet m.m.f. to magnet volume. The effect of changing the pole number of the motor was also discussed. An interesting effect of increasing the pole number is that the stator armature reaction effect on the magnets is reduced.

A program was written that predicted motor performance based on design input data. This program was used to investigate different motor designs using a number of Neodymiuum Iron Boron magnet grades. One of these designs was selected and built to enable actual test data to be obtained. The Neodymium motor had 2% less magnet volume and 12% less magnet weight than the corresponding Samarium Cobalt motor. When the motor was tested it performed almost identically to the Samarium Cobalt motor for a winding temperature of 125°C. It was found to have slightly better performance at lower temperatures. Predicted data indicates that at temperatures above 125°C the Samarium Cobalt motor performance is relatively better than the Neodymium motor. This is to be expected as a result of the higher temperature coefficient of Induction of Neodymium Iron Boron material.

The motor voltage constant at room temperature was measured after each load test to determine if Irreversible losses occurred. No discernible Irreversible loss was noted even after the magnets had been subjected to temperatures of 139°C.

These tests verify the feasibility of using medium grade Neodymium Iron Boron material in high performance servo-motor applications with magnet temperatures up to 139°C. However care must be taken at a design stage to ensure that the operating flux levels in the magnets will not lead to Irreversible flux losses at elevated temperatures. Since the magnetic properties of this material are similar to those of Samarium Cobalt magnets, it is unlikely to find widespread use unless it is more attractive on a cost basis.

The use of the highest energy product Neodymium Iron Boron magnet grades in servo-motor applications does not seem practical at present. This is due to the large reduction in magnet coercivity and residual induction at elevated temperatures. Substantial improvements in servo-motor performance are unlikely without the development of less temperature sensitive grades of Neodymium Iron Boron magnets at these energy product levels. Until then, this material will find use in an increasing number of applications where its temperature limitations are acceptable and material costs are important.

Bibliography.

[1] " A new approach to Flux and Torque-Sensing
in Induction machines."
Thomas A. Lipo, Kwong C. Chang.
IEEE/Trans. I.App. Vol.1A-22, No 4 JUL/AUG '86

[2] " Electric Machines."
G.R. Slemon, A. Straughan.
Addison-Wesley Pub. Co. 1982

[3] " Electronically Commutated D.C. Drives for
Machine Tools."
P. Zimmermann.
Motorcon Proc. Sept 1982.

[4] " D.C. Motors, Speed Controls, Servo Systems."
An Engineering Handbook.
Electro-Craft Corporation.

[5] " Nd-Fe Permanent Magnets."
Comission Of The European Communities.
Elsevier Applied Science Publishers. (1985)

[6] " Application Technology Evaluation Criteria Of
D.C. Servo-Motors."
Klaus Bruchmann.
Motor-Con April 1985 Proc.

[7] " Permanent magnets and their applications."
Rollin J. Parker & Robert J. Studders.

[8] " Permanent magnet generators Part (1)."
AIEE/TRANS. Vol 76, Pt (3), pp 1098 - 1103, 1957
D.J. Hanrahan & D.S. Toffolo.

[9] " Modern permanent magnets (materials & applications)."
University of Dayton Short Summer Course, June 1984.
Course coordinator: Professor Karl J. Strnt.

[10] " The Nature of Polyphase Induction Machines."
Philip L. Alger.
John Wiley & Sons Ltd (1951)
Reprinted: Gordon and Breach. 1970

[11] " Theory and design of small induction motors."
Cyril G. Veinott.
University of Missouri - Rolla (reprint).

[12] " Matrix analysis of space harmonics of asymmetrical stator windings."
Prof. J. Stepina, Dr. Ing. D.Sc.
IEE/Proc. Vol. 134, Pt B, No 4, July '87.

[13] " Alternating Current Machines."
Michael Liwschitz - Garik & Clyde C. Whipple.
D. Van Nostrand Co. Inc. (1961).

[14] " Fundamental equations of the space vector analysis of electrical machines."
Prof. J. Stepina, Dr. Ing. D.Sc.
Acta. Tech. CSAV. 1968. 13, pp. 184 – 198.

[15] " A.C. Machine Design with Conventional and Converter Supplies."
University Of Wisconsin Extension Program.
July 1984.

[16] " Electric Motor and Generator Design."
P.H. Trickey.
Duke University. U.S.A.

[17] " Polyphase Motors (Direct approach to their Design)."
Enrico Levi.
John Wiley & Sons Inc. 1984.

[18] " Finite Element Analysis of Single-Phase and
Polyphase Induction Motors."
John R. Brauer.
IEEE/TRANS. IAS.23B, 1981.

[19] " Electrical Machine Design and Finite Elements."
E. Richter.
IEEE. TRANS. IAS.23A 1981.

[20] " Torque Pulsations in Induction Motors with
Inverter Drives."
Stuart D. T. Robertson, K. M. Hebbar.
IEEE/TRANS. IGA. vol. IGA-7, Mar/Apr. 1971.

[21] " Influence of Motor Design and Feed-Current
waveform on Torque Ripple in Brushless D.C. drives."
H. R. Bolton, R. A. Ashen.
IEE/PROC. Vol. 131 Pt. B, May 1984.

[22] " Torque, Voltage and Current Harmonics of
Synchronous Machines."
Edward D. Goodman.
IEEE/TRANS, IAS. ANN. MEET. 1982.

[23] " Harmonic effects in Pulse Width Modulated Inverter
Induction motor drives."
Gerald B. Kliman
IEEE/IAS 1972 Annual Meeting, pp. 783-790, 1972

[24] " Harmonic Distortion in PWM inverter output waveforms."
P.D. Evans & P.R. Close.
IEE/Proc. Vol.134. Pt.B, No 4, July 1987.

[25] " Losses and Parasitic Torques in Electric Motors
Subjected to PWM Waveforms."
Fernand G.G. De Buck.
IEEE/TRANS. I.A. Vol 1A-15, No. 1, JAN./FEB. 1979.

[26] " A simple but Reliable Loss Model for Inverter
Supplied Induction Motors."
Fernand G.G. De Buck et-al.
IEEE/TRANS. I.A. Vol 1A-20, No. 1, JAN./FEB. 1984.

[27] " Loss-optimal PWM waveforms for variable-speed
Induction motor drives."
Fernand G.G. De Buck et-al.
IEE/PROC. Vol 130, Pt. B, No. 5, SEPT. 1983.

[28] " On the Torques and Losses of Voltage and Current
Source Inverter Drives."
Egon C. Andresen, Kurt Bieniek.
IEEE/TRANS. I.A. Vol 1A-20, No. 2, MAR./APR. 1984.

[29] " Polyphase Induction Motor Performance and Losses
on Nonsinusoidal Voltage Sources".
E. A. Klingshirn, H. E. Jordan.
IEEE/TRANS. PAS. Vol. PAS-87, No. 3, MARCH 1968.

[30] " Separation of losses in Low-Alloy, nonoriented
electrical steels."
E. T. Stephenson
J. Appl. Phys. 57 (1), 15 April 1985.

[31] " Effects of thickness and resistivity on core loss
and permeability of nonoriented semiprocessed steels."
E. T. Stephenson
J. Appl. Phys. 55 (6), 15 March 1984.

[32] " Factors Affecting Localised Flux and Iron Loss distribution in Laminated Cores."
A. J. Moses.
Journal of Magnetism and Magnetic Materials, Vol. 41(1-3) Feb. 1984.

[33] " Analytic separation of the factors contributing to the eddy-current loss in magnetically nonlinear steel."
A. L. Bowden, Prof. E. J. Davies.
IEE/PROC, Vol. 130, Pt. B, Sept. 1983.

[34] " Numerical Analysis of Flux and Loss distribution in Electrical Machinery."
T. Nakata.
IEEE/TRANS. MAGS. Vol. Mag-20, No 5, Sept. 1984.

[35] " The Origin of Anomalous Loss in Grain-Oriented Silicon-Iron."
Mrs. S. Hill and K.J. Overshott.
Wolfson Centre for Magnetics Technology
University College, Cardiff, U.K.

APPENDIX (A)

Magnetic Units Conversion Table

	S.I. Unit	Equivalent Unit
Magnetic Flux	1 Weber.	10^8 Maxwells. 10^8 Lines.
Magnetic Flux Density.	1 Tesla.	10^4 Gauss. 64,516 Lines/ sq.in.
Magnetic Field Strength.	1 Ampere/metre	1.2566×10^{-2} Oerstead

APPENDIX (B)

PROGRAM WDGMMF.FOR 2/6/88

CALCULATION OF WINDING HARMONICS

THIS PROGRAM CALCULATES THE SPACE HARMONICS DUE TO THE SPACIAL DISTRIBUTION OF THE WINDINGS IN AN IRREGULAR THREE PHASE WINDING. THE METHOD USED IS BASED ON A PROCEDURE OUTLINED BY P.L. ALGER FOR WINDING ANALYSIS .

```
C                PROGRAM WDGMMF.FOR       2/6/88
C
C                CALCULATION OF WINDING HARMONICS
C
C        THIS PROGRAM CALCULATES THE SPACE HARMONICS DUE
C        TO THE SPACIAL DISTRIBUTION OF THE WINDINGS IN AN
C        IRREGULAR THREE PHASE WINDING.  THE METHOD USED
C        IS BASED ON A PROCEDURE OUTLINED BY P.L. ALGER FOR
C        WINDING ANALYSIS .
C
C
          DIMENSION X(490), Y(490), Z(490), AMOD(490),AANG(490),
     /    BMOD(490),BANG(490), CMOD(490), CANG(490), ANGA1(490),
     /    ANGB1(490), ANGC1(490), AREAL(490), AIMAG(490),
     /    BREAL(490), BIMAG(490),CREAL(490), CIMAG(490), RESR(490)
     /    ,RESI(490), PHMOD(490),PHANG(490), ANGA2(490),
     /    ANGB2(490), ANGC2(490), RESR2(490), RESI2(490),
     /    PHMOD1(490), PHANG1(490),A(490),B(490),C(490),FW1(490),
     /    FW2(490),FW3(490),FWDG(490),FWDG1(490)
C
C
C
          REAL PI,SLOTS,POLES,PHASES,M,TPC
C
          OPEN (UNIT = 11,FILE = 'WHAR.DAT',STATUS = 'OLD',
     /         ACCESS = 'SEQUENTIAL',FORM = 'FORMATTED' )
C
          REWIND (11)
C
          OPEN (UNIT = 10.FILE ='DHARM.DAT'.STATUS = 'OLD',
     /         ACCESS = 'SEQUENTIAL',FORM = 'FORMATTED' )
C
          REWIND (10)
C
          READ(10,20)DUMMY1,DUMMY2,DUMMY3,DUMMY4,
     /               DUMMY5
   20     FORMAT (40X,G12.4)
C
          READ (10,21) SSPEC,DUMMY1,DUMMY2,DUMMY3,
     /                 DUMMY4,DUMMY5
   21     FORMAT (40X,G12.4)
C
          READ (10,22) DUMMY1,DUMMY2
   22     FORMAT (65X,G12.4)
C
          DO 11,J = 1,SSPEC,2
                   READ(10,23) A(J),A(J+1)
   23              FORMAT (38X,G12.4,G12.4)
   11     CONTINUE
C
          READ (10,24) DUMMY1,DUMMY2,DUMMY3,DUMMY4
   24     FORMAT (65X,G12.4)
C
          DO 12,J = 1,SSPEC,2
                   READ (10,25) B(J),B(J+1)
   25              FORMAT (38X,G12.4,G12.4)
   12     CONTINUE
C
          READ (10,26) DUMMY1,DUMMY2,DUMMY3,DUMMY4
   26     FORMAT (65X,G12.4)
```

```
C
      DO 13,J = 1,SSPEC,2
              READ (10,27) C(J),C(J+1)
  27          FORMAT (38X,G12.4,G12.4)
  13  CONTINUE
C
      READ (10,28) SLOTS,POLES,PHASES,M,TPC,CSPP
  28  FORMAT (40X,G12.4)
C
C
      PI = 3.14159265
C
C     THE PROGRAM WILL CALCULATE THE MAGNITUDES OF THE
C     FIRST M HARMONICS.
C
C
      PRINT*,' '
      PRINT*,'                MOTOR WINDING ANALYSIS '
      PRINT*,'                ---------------------- '
      PRINT51,'NUMBER OF SLOTS ',' = ',SLOTS,
     /        'NUMBER OF POLES ',' = ',POLES,
     /        'NUMBER OF PHASES',' = ',PHASES,
     /        'HARMONIC NUMBER ',' = ',M,
     /        'TURNS PER COIL  ',' = ',TPC,
     /        'COIL SIDES/PHASE',' = ',CSPP
  51  FORMAT (A32,A5,G12.4)
      PRINT*,' '
C
C
      DO  1, J=1,M
              N = N+1
              DO  2,I=1,SSPEC,2
                      A2 = A(I)
                      A3 = A(I+1)
                      CALL ANGLES (PI,N,A2,A3,X(I),X(I+1))
   2          CONTINUE
              DO  3,I=1,SSPEC,2
                      B2 = B(I)
                      B3 = B(I+1)
                      CALL ANGLES (PI,N,B2,B3,Y(I),Y(I+1))
   3          CONTINUE
              DO  4,I=1,SSPEC,2
                      C2 = C(I)
                      C3 = C(I+1)
                      CALL ANGLES (PI,N,C2,C3,Z(I),Z(I+1))
   4          CONTINUE
C
C     ALL PHASORS HAVE BEEN CHANGED TO CARTESIAN COORDINATES
C     BY SUBROUTINE ANGLES.
C
C
                      XRTOT = 0.0
                      XITOT = 0.0
              DO  5,I=1,SSPEC,2
                      XRTOT = XRTOT + X(I)
                      XITOT = XITOT + X(I+1)
   5          CONTINUE
              AMOD(J) = (XRTOT**2 + XITOT**2 )**0.5
              FW1(J)  = AMOD(J)/CSPP
C
```

```
C
                IF ((XRTOT.EQ.0.0).AND.(XITOT.LT.0.0)) THEN
                        AANG(J) = -PI/2
                ELSE IF ((XRTOT.EQ.0.0).AND.(XITOT.GT.0.0))THEN
                        AANG(J) = PI/2
                ELSE
                        AANG(J) = ATAN ( XITOT/XRTOT )
                   IF ( XRTOT .LT. 0.0 )AANG(J) = AANG(J) - PI
                END IF
C
                        YRTOT = 0.0
                        YITOT = 0.0
                DO  6,I=1,SSPEC,2
                        YRTOT = YRTOT + Y(I)
                        YITOT = YITOT + Y(I+1)
    6           CONTINUE
                     BMOD(J) = ( YRTOT**2 + YITOT**2 )**0.5
                     FW2(J)  = BMOD(J)/CSPP
C
                IF ((YRTOT.EQ.0.0).AND.(YITOT.LT.0.0)) THEN
                        BANG(J) = -PI/2
                ELSE IF ((YRTOT.EQ.0.0).AND.(YITOT.GT.0.0)) THEN
                        BANG(J) = PI/2
                ELSE
                     BANG(J) = ATAN (YITOT/YRTOT )
                   IF ( YRTOT .LT. 0.0 ) BANG(J) = BANG(J) - PI
                END IF
C
                        ZRTOT = 0.0
                        ZITOT = 0.0
                DO  7,I=1,SSPEC,2
                        ZRTOT = ZRTOT + Z(I)
                        ZITOT = ZITOT + Z(I+1)
    7           CONTINUE
                     CMOD(J) = ( ZRTOT**2 + ZITOT**2 )**0.5
                     FW3(J)  = CMOD(J)/CSPP
                IF ((ZRTOT.EQ.0.0).AND.(ZITOT.LT.0.0)) THEN
                        CANG(J) = -PI/2
                ELSE IF ((ZRTOT.EQ.0.0).AND.(ZITOT.GT.0.0)) THEN
                        CANG(J) = PI/2
                ELSE
                        CANG(J) = ATAN(ZITOT/ZRTOT)
                       IF (ZRTOT.LT.0.0 ) CANG(J) = CANG(J) - PI
                END IF
C
C       WE NOW HAVE THE RESULTANT Jth HARMONIC PHASOR FOR EACH
C       OF THE THREE PHASES. TO OBTAIN THE FORWARD AND BACKWARD
C       ROTATING FIELDS ACCOUNT MUST BE TAKEN OF THE PHASE SHIFT
C       IN TIME BETWEEN EACH OF THE THREE PHASES.
C
C               TO OBTAIN THE FORWARD FIELD COMPONENTS.
C
C
                ANGA1(J) = AANG(J) - 0.0
                ANGB1(J) = BANG(J) - 2*PI/3
                ANGC1(J) = CANG(J) - 4*PI/3
C
C       CHANGE BACK TO CARTESIAN USING SUBROUTINE QUAD.
C
                CALL QUAD (AMOD(J),ANGA1(J),AREAL(J),AIMAG(J),PI)
```

```
                CALL QUAD (BMOD(J),ANGB1(J),BREAL(J),BIMAG(J),PI)
                CALL QUAD (CMOD(J),ANGC1(J),CREAL(J),CIMAG(J),PI)
C
C
C
C       GET RESULTANT FROM THREE PHASES
C
                RESR(J) = AREAL(J) + BREAL(J) + CREAL(J)
                RESI(J) = AIMAG(J) + BIMAG(J) + CIMAG(J)
C
C       CONVERT BACK TO POLAR FORM AND DIVIDE BY HARMONIC ORDER
C
                PHMOD(J) = (RESR(J)**2 + RESI(J)**2 )**0.5

                IF ((RESI(J).GE.0.0).AND.(RESR(J).LT.0.0)) THEN
                        RESR(J) = -RESR(J)
                        PHANG(J) = ATAN(RESI(J)/RESR(J))
                        PHANG(J) = -PHANG(J) + PI
                ELSE IF((RESI(J).LE.0.0).AND.(RESR(J).LT.0.0)) THEN
                        PHANG(J) = ATAN(RESI(J)/RESR(J))
                        PHANG(J) = PHANG(J) + PI
                ELSE IF ((RESR(J).EQ.0.0).AND.(RESI(J).LT.0.0)) THE
                        PHANG(J) = -PI/2
                ELSE IF((RESR(J).EQ.0.0).AND.(RESI(J).GT.0.0))THEN
                        PHANG(J) = PI/2
                ELSE IF((RESR(J).EQ.0.0).AND.(RESI(J).EQ.0.0))THEN
                        PHANG(J) = 0.0
                ELSE
                       .PHANG(J) = ATAN(RESI(J)/RESR(J))
                END IF
                PHMOD(J) = PHMOD(J)/(2*N)
                PHMOD(J) = PHMOD(J)/2*2*TPC/PI
C
C       TPC = TURNS PER COIL
C
C        FORWARD FIELD MAGNITUDE AND ANGLE OBTAINED
C
C
C----------------------------------------------------------------
C
C       TO OBTAIN THE BACKWARD FIELD COMPONENTS
C
                ANGA2(J) = AANG(J) + 0.0
                ANGB2(J) = BANG(J) + 2*PI/3
                ANGC2(J) = CANG(J) + 4*PI/3
C
C       CHANGE TO CARTESIAN USING SUBROUTINE QUAD.
C
        CALL QUAD (AMOD(J),ANGA2(J),AREAL(J),AIMAG(J),PI)
        CALL QUAD (BMOD(J),ANGB2(J),BREAL(J),BIMAG(J),PI)
        CALL QUAD (CMOD(J),ANGC2(J),CREAL(J),CIMAG(J),PI)
C
C
C
C       GET BACKWARD FIELD RESULTANT FOR THREE PHASORS
C
                RESR2(J) = AREAL(J) + BREAL(J) + CREAL(J)
                RESI2(J) = AIMAG(J) + BIMAG(J) + CIMAG(J)
C
C       CONVERT BACK TO POLAR FORM AND DIVIDE BY HARMONIC ORDER
```

```
C
                PHMOD1(J) = (RESR2(J)**2 + RESI2(J)**2 )**0.5
                IF ((RESR2(J).LT.0.0).AND.(RESI2(J).GE.0.0)) THEN
                        RESR2(J) = -RESR2(J)
                        PHANG1(J) = ATAN(RESI2(J)/RESR2(J))
                        PHANG1(J) = -PHANG1(J) + PI
                ELSE IF ((RESR2(J).LT.0.0).AND.(RESI2(J).LE.0.0)) THEN
                        PHANG1(J) = ATAN(RESI2(J)/RESR2(J))
                        PHANG1(J) = PHANG1(J) + PI
                ELSE IF((RESR2(J).EQ.0.0).AND.(RESI2(J).LT.0.0))THEN
                        PHANG1(J) = -PI/2
                ELSE IF((RESR2(J).EQ.0.0).AND.(RESI2(J).GT.0.0))THEN
                        PHANG1(J) = PI/1
                ELSE IF((RESR2(J).EQ.0.0).AND.(RESI2(J).EQ.0.0))THEN
                        PHANG1(J) = 0.0
                ELSE
                        PHANG1(J) = ATAN(RESI2(J)/RESR2(J))
                END IF
                PHMOD1(J) = PHMOD1(J)/(2*N)
                PHMOD1(J) = PHMOD1(J)/2*2*TPC/PI
C
C               BACKWARD FIELD MAGNITUDE AND ANGLE OBTAINED
C---------------------------------------------------------------------
C
C
                PRINT*,' '
                PRINT60,'HARMONIC',' PHASE ','WINDING',' FORWARD  FIELD
     /          ' BACKWARD  FIELD ',' ORDER  ','       ','FACTOR',
     /          '  MAG    ANGLE  ',' MAG     ANGLE  ',
     /          ' ------ ',' ---  ',' ----- ',' ---     ---    ',
     /          '  ---      ---   '
  60            FORMAT (A12,A9,A10,A21,A21)
                PRINT61,J,'A',FW1(J)
  61            FORMAT (I8,A10,G16.4)
                PRINT62,J,'B',FW2(J),PHMOD(J),PHANG(J),PHMOD1(J),PHANG1
  62            FORMAT (I8,A10,G16.4,G11.3,G11.3,G11.3,G11.3)
                PRINT61,J,'C',FW3(J)
                PRINT*,' '
C
                WRITE(11,111),J,PHMOD(J),J,PHMOD1(J)
  111           FORMAT(I8,G12.4)
C
C
   1    CONTINUE
C
        END
C
C
C
C
C                       SUBROUTINE TO CHANGE COORDINATE SYSTEM
C
                SUBROUTINE ANGLES (PI,N,AN1,AN2,XN1,XN2)
                        AN2 = AN2*PI*N/180
                        AN2 = MOD(AN2,PI*2)
                        IF ((AN2.GT.PI/2).AND.(AN2.LE.PI)) THEN
                                AN2 = PI - AN2
                                XN1 = AN1*COS(AN2)*(-1)
                                XN2 = AN1*SIN(AN2)
                        ELSE IF ((AN2.GT.PI).AND.(AN2.LE.3*PI/2)) THEN
```

```
                AN2 = AN2 - PI
                XN1 = -AN1*COS(AN2)
                XN2 = -AN1*SIN(AN2)
        ELSE IF ((AN2.GT.0).AND.(AN2.LE.PI/2)) THEN
                XN1 = AN1*COS(AN2)
                XN2 = AN1*SIN(AN2)
        ELSE IF ((AN2.LE.0.0).AND.(AN2.GT.-PI/2)) THEN
                AN2 = -AN2
                XN1 = AN1*COS(AN2)
                XN2 = -AN1*SIN(AN2)
        ELSE IF ((AN2.LE.-PI/2).AND.(AN2.GT.-PI)) THEN
                AN2 = PI + AN2
                XN1 = -AN1*COS(AN2)
                XN2 = -AN1*SIN(AN2)
        ELSE IF ((AN2.LE.-PI).AND.(AN2.GT.-3*PI/2)) THEN
                AN2 = AN2 +3*PI/2
                XN1 = -AN1*SIN(AN2)
                XN2 = AN1*COS(AN2)
        ELSE IF ((AN2.LE.-3*PI/2).AND.(AN2.GT.-2*PI)) THEN
                AN2 = AN4 + 2*PI
                XN1 = AN1*COS(AN2)
                XN2 = AN1*SIN(AN2)
        ELSE
                AN2 = 2*PI - AN2
                XN1 = AN1*COS(AN2)
                XN2 = AN1*SIN(AN2)*(-1.0)
        END IF
END

C
C
C
C
C

SUBROUTINE QUAD (AN3,AN4,XN3,XN4,PI)
        AN4 = MOD(AN4,PI*2)
IF ((AN4.GT.PI/2).AND.(AN4.LE.PI)) THEN
        AN4 = PI - AN4
        XN3 = -AN3*COS(AN4)
        XN4 = AN3*SIN(AN4)
ELSE IF ((AN4.GT.PI).AND.(AN4.LE.3*PI/2)) THEN
        AN4 = AN4 - PI
        XN3 = -AN3*COS(AN4)
        XN4 = -AN3*SIN(AN4)
ELSE IF ((AN4.GT.0.0).AND.(AN4.LE.PI/2)) THEN
        XN3 = AN3*COS(AN4)
        XN4 = AN3*SIN(AN4)
ELSE IF ((AN4.LE.0.0).AND.(AN4.GT.-PI/2)) THEN
        AN4 = -AN4
        XN3 = AN3*COS(AN4)
        XN4 = -AN3*SIN(AN4)
ELSE IF ((AN4.LE.-PI/2).AND.(AN4.GT.-PI)) THEN
        AN4 = PI + AN4
        XN3 = -AN3*COS(AN4)
        XN4 = -AN3*SIN(AN4)
ELSE IF ((AN4.LE.-PI).AND.(AN4.GT.-3*PI/2)) THEN
        AN4 = AN4 + 3*PI/2
        XN3 = -AN3*SIN(AN4)
        XN4 = AN3*COS(AN4)
ELSE IF ((AN4.LE.-3*PI/2).AND.(AN4.GT.-2*PI)) THEN
        AN4 = AN4 + 2*PI
```

```
            XN3 = AN3*COS(AN4)
            XN4 = AN3*SIN(AN4)
      ELSE
            AN4 = 2*PI - AN4
            XN3 = AN3*COS(AN4)
            XN4 = -AN3*SIN(AN4)
      END IF
C
      END
```

DATA FILE FOR HARMONIC ANALYSIS

SLOT SPECIFIER CONSTANT = 32.0

CURRENT PHASORS INPUT

PHASE A

MAGNITUDE	ANGLE
2.0	0.0000
1.0	9.2308
-1.0	27.6923
-2.0	36.9231
2.0	64.6154
-2.0	92.3077
1.0	120.0000
1.0	129.2308
-2.0	156.9231
2.0	184.6154
-2.0	212.3077
1.0	240.0000
1.0	249.2308
-2.0	276.9231
2.0	304.6154
-2.0	332.3077

PHASE B

MAGNITUDE	ANGLE
1.0	18.4615
1.0	27.6923
-2.0	55.3846
2.0	83.0769
-2.0	110.7692
-1.0	120.0000
1.0	138.4615
2.0	147.6923
-2.0	175.3846
2.0	203.0769
-1.0	230.7692
-1.0	240.0000
2.0	267.6923
-2.0	295.3846
2.0	323.0769
-2.0	350.7692

PHASE C

MAGNITUDE	ANGLE
-1.0	9.2308
-1.0	18.4615
2.0	46.1538
-2.0	73.8462
2.0	101.5385
-1.0	129.2308
-1.0	138.4615
2.0	166.1539
-2.0	193.8462
2.0	221.5385
1.0	230.7692
-1.0	249.2308
-2.0	258.4615
2.0	286.1539
-2.0	313.8462
2.0	341.5385

NUMBER OF SLOTS	39.0
NUMBER OF POLES	12.0
NUMBER OF PHASES	3.0
NUMBER OF HARMONICS	486.0
TURNS PER COIL	13.0
COIL SIDES PER PHASE	26.0

MOTOR WINDING ANALYSIS

NUMBER OF SLOTS	=	39.00
NUMBER OF POLES	=	12.00
NUMBER OF PHASES	=	3.000
HARMONIC NUMBER	=	486.0
TURNS PER COIL	=	13.00
COIL SIDES/PHASE	=	26.00

HARMONIC ORDER	PHASE	WINDING FACTOR	FORWARD FIELD MAG	FORWARD FIELD ANGLE	BACKWARD FIELD MAG	BACKWARD FIELD ANGLE
1	A	0.1841E-01				
1	B	0.1578E-01	1.13	-1.41	1.97	-0.362
1	C	0.1841E-01				

HARMONIC ORDER	PHASE	WINDING FACTOR	FORWARD FIELD MAG	FORWARD FIELD ANGLE	BACKWARD FIELD MAG	BACKWARD FIELD ANGLE
2	A	0.3575E-01				
2	B	0.4522E-01	1.90	3.99	0.682	-1.25
2	C	0.3575E-01				

HARMONIC ORDER	PHASE	WINDING FACTOR	FORWARD FIELD MAG	FORWARD FIELD ANGLE	BACKWARD FIELD MAG	BACKWARD FIELD ANGLE
3	A	0.8553E-01				
3	B	0.8197E-01	4.42	-0.403E-01	0.713	4.15
3	C	0.8553E-01				

APPENDIX (C)

Calculation of harmonic m.m.f.'s produced by magnets

In order to estimate the magnitudes of the generated e.m.f.'s produced by the Moog motor, it is first necessary to estimate the m.m.f. harmonics produced by the surface-mounted magnets of the rotor. Prior to assembly of the rotor, the magnets are produced as rectangular blocks and subjected to a magnetising process such that the direction of magnetisation is normal to one face of the blocks. After assembly, the magnets are subjected to a grinding process on one face so as to give a uniform air-gap when assembled inside the stator. The rectangular blocks now have one face curved as shown in Fig. (1) below.

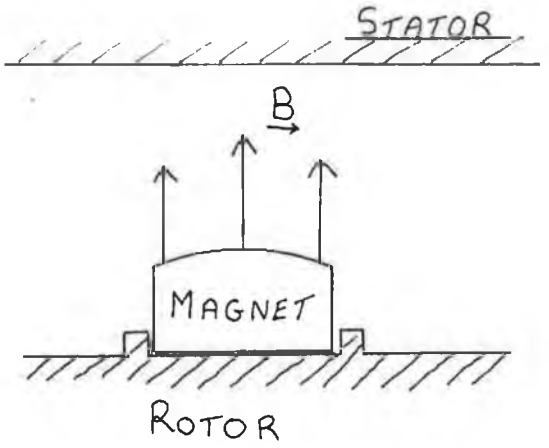

FIG. (1) Air-Gap of P.M. motor showing the curved surface of the magnet as a result of grinding Rotor Diameter.

Assuming that the grinding process does not alter the internal orientation of the magnetic induction B and that the m.m.f. of the magnet is proportional to magnet length, then the shape of the m.m.f. distribution is equivalent to the magnet shape as shown in Fig. (2). This figure represents two pole pitches of the motor assuming that the rotor diameter is infinite and the angles α_1 and α_2 depend on the magnet to pole width ratio. Since the m.m.f. distribution is an even function, the Fourier coefficients a_n are zero. Table (1) contains the b_n Fourier coefficients

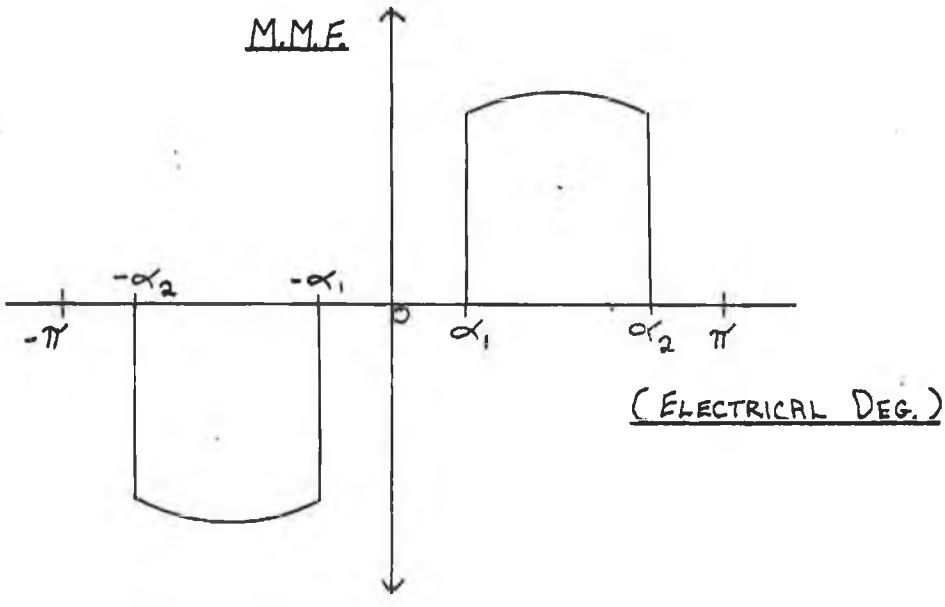

FIG. (2) Rotor magnet m.m.f distribution over two Pole pitches.

Table (1)

Harmonic Order	a_n Magnitude
1	100.0
2	-
3	0.786
4	-
5	-16.87
6	-
7	-14.13
8	-
9	-3.03
10	-
11	6.22
12	-
13	7.96
14	-
15	3.13
16	-
17	-3.02
18	-
19	-5.47
20	-
21	-3.06
22	-
23	1.42
24	-
25	4.01
26	-
27	2.92
28	-
29	-0.44
30	-

APPENDIX (D)

Star connected load supplied by three phase unbalanced supply

Figure (1) illustrates a balanced star-connected load fed from a three phase voltage supply. Using the principle of superposition it can be shown in general that,

$$E_1 = \frac{1}{3.R}\left[2.V_1\cos(wt) - V_2\cos(wt - \alpha_1) - V_3\cos(wt - \alpha_2) \right]$$

where E_1 is the voltage across R_1 as a result of the current I_1,

The measured voltage E_1 is only equal to $V_1\cos(wt)$ at every point in time if the applied voltages V_1, V_2 and V_3 are equal in magnitude and if the angles α_1 and α_2 are equal to 120 and 240 degrees respectively i.e. if the supply is balanced.

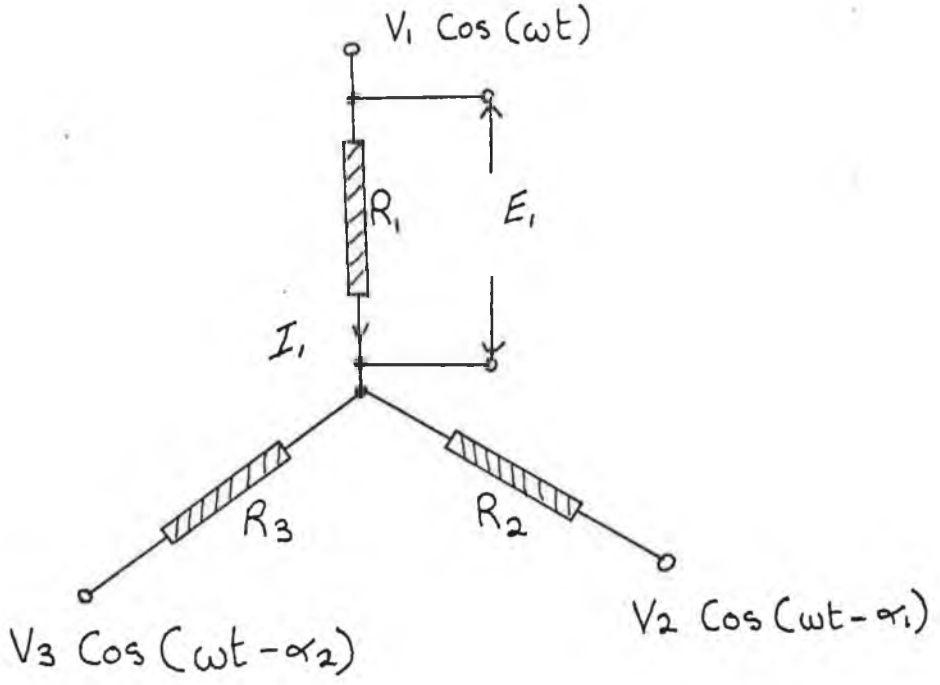

FIG. (1) Balanced Star-connected load fed by a three phase voltage supply.

APPENDIX (E)

Calculation of Permeance harmonics due to Stator and Rotor Slots.

Permeance variation due to rotor slotting.

Figure (1) is an approximation of the inverse of the air-gap variation due to slotting of the rotor taken over two pole pitches.

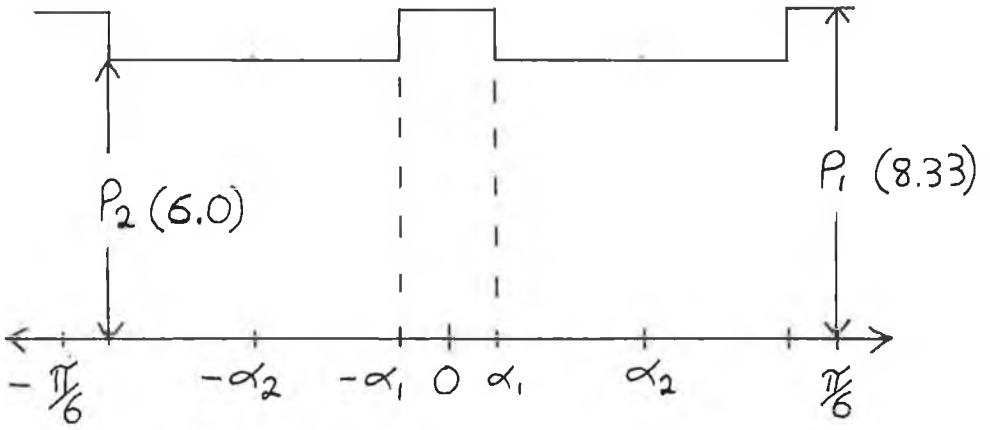

FIG. (1) Inverse of the Air-gap variation due to Rotor slotting versus mechanical degrees.

The permeance is assumed to vary between two values corresponding to the edges of the metal lugs of the rotor. These values of permeance are equal to the inverse of the air-gap length in inches. Since the magnets have a relative permeability of approximately 1.05 to 1.1 times that of air the air-gap over the magnets was reduced by 1.05 times magnet length for the purposes of the analysis. Similarly, as the permeability of the solid rotor lugs is not infinite, the air-gap over the lugs was increased by 0.1 times the magnet length. A computer program was written to calculate the Fourier series of the permeance function and the results are contained in Table (1). Because of the symmetry of the function, the coefficients $\Sigma\ b_n$ are zero.

TABLE (1)

Calculated magnitude of Rotor Permeance Harmonics due to Rotor slotting.

Harmonic Order	Magnitude a_n
0	100.0
1	11.60
2	8.60
3	4.54
4	0.75
5	- 1.84
6	- 2.76
7	- 2.20
8	- 0.74
9	0.72
10	1.55
11	1.49
12	0.71
13	-
14	- 1.00
15	- 1.14
16	- 0.69
17	-
18	0.67
19	0.90
20	0.66
21	-
22	-
23	- 0.73
24	- 0.62
25	-
26	-
27	0.59
28	0.58
29	-
30	-

Stator permeance harmonics

Figure (2) is an illustration of an approximation of the air-gap permeance variation $P(\theta)$ as a result of the stator slots. Since the motor has 39 slots of similar proportions only one slot pitch is shown here. The air-gap can be divided into three basic regions A, B and C as follows,

Region A

This corresponds to the main portion of a stator tooth which presents a relatively high permeance path to the air-gap m.m.f. The permeance value over this portion of the air-gap is proportional to the inverse of the air-gap length.

Region B

This corresponds to the edges of the teeth and is approximated by a linearly varying permeance function as shown. The permeance value varies between 100% and 90% the value in region A of the air-gap to account for saturation in the tooth tips.

Region C

This corresponds to the slot openings and the permeance is considered to vary linearly between 90% and 80% of the value in region A of the air-gap. Obviously the representation of the air-gap permeance given here is somewhat arbitrary and the application of finite element analysis would be required to accurately determine the air-gap variation. However some idea of the order of the permeance harmonics can be obtained even if the magnitudes are not accurate. A computer program was written to estimate the Fourier series representation of this function and the results of the analysis are presented in Table (1).

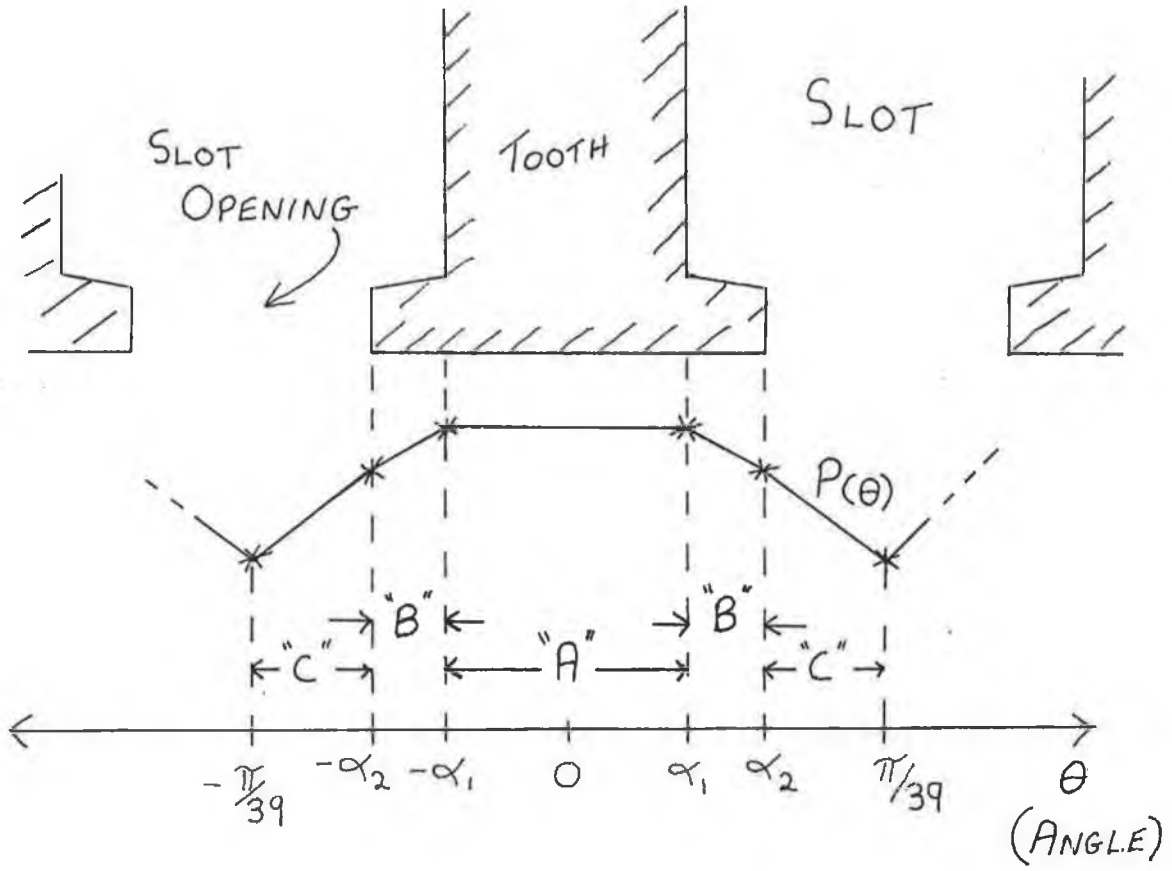

FIG. (2) Air-Gap Permeance variation due to Stator slots.

TABLE (2)

Calculated Permeance harmonics due to Stator slots.

Harmonic Order	Magnitude a_n
0	100
1	5.6
2	23.2
3	11.0
4	13.3
5	13.3
6	5.7
7	11.7
8	0.4
9	6.5

APPENDIX (F)

DEMAGNETISATION CURVES FOR VARIOUS PERMANENT MAGNET MATERIALS.

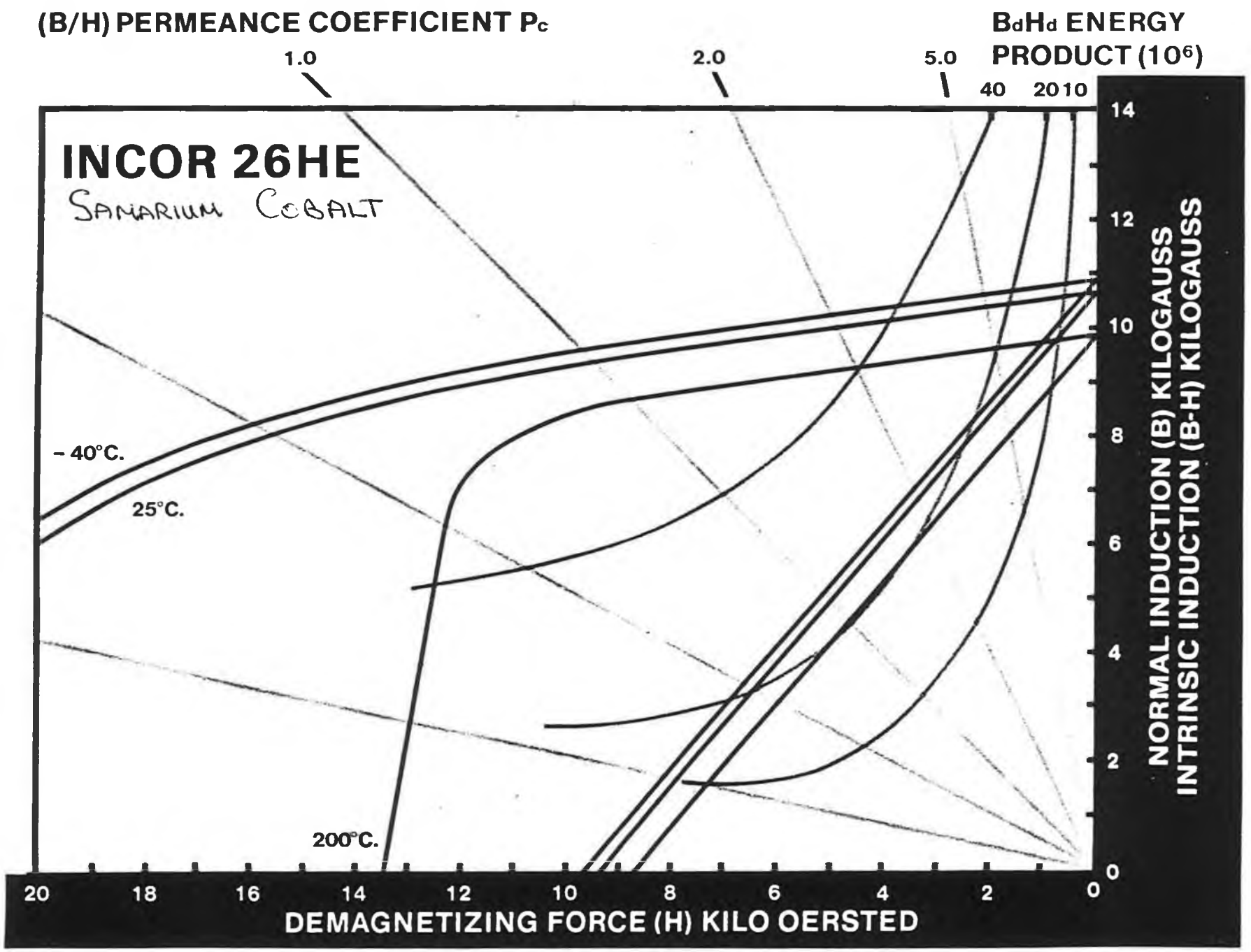

I G Technologies, Inc.

DEMAGNETIZATION CURVES

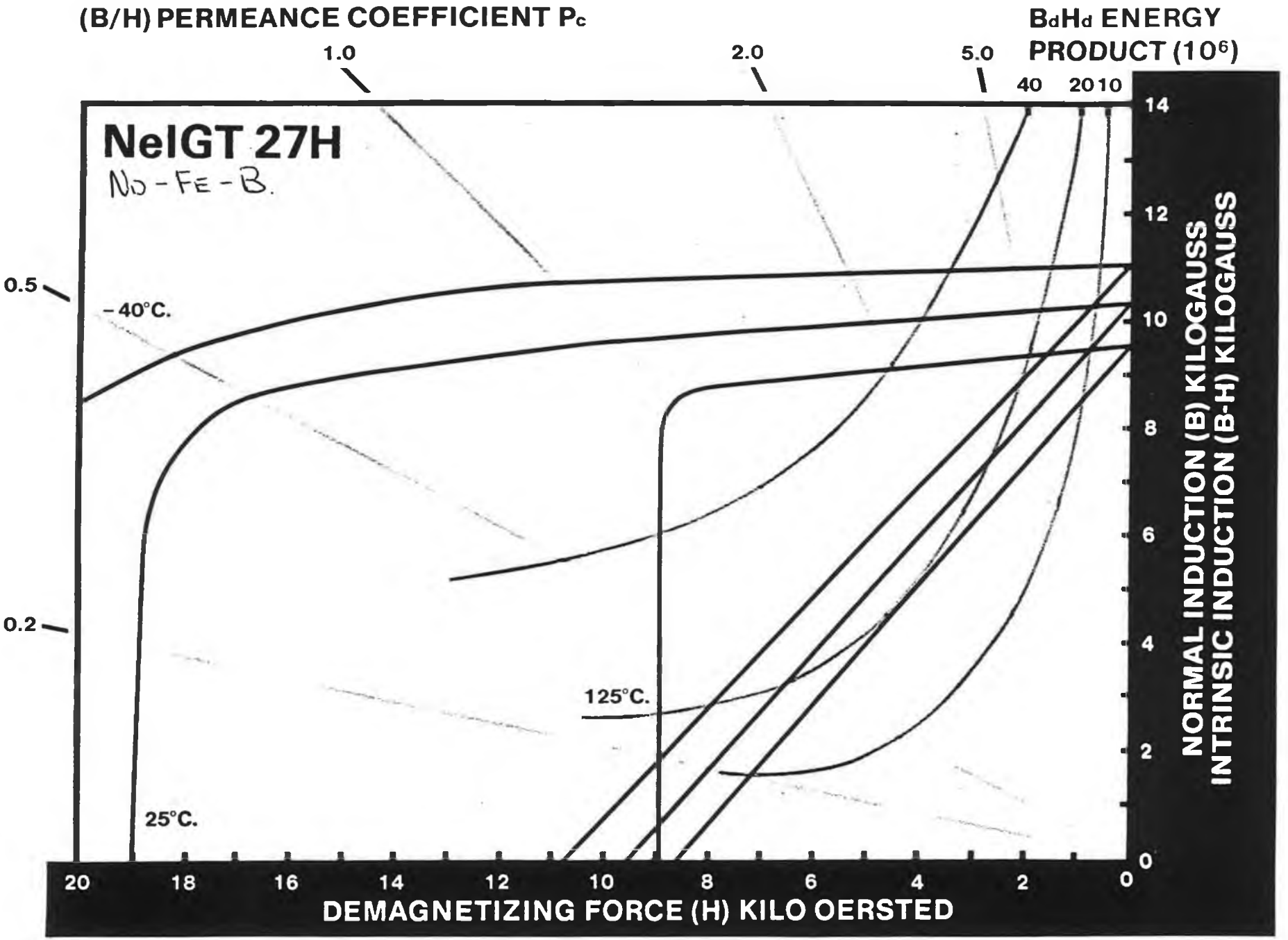

I G Technologies, Inc.

DEMAGNETIZATION CURVES

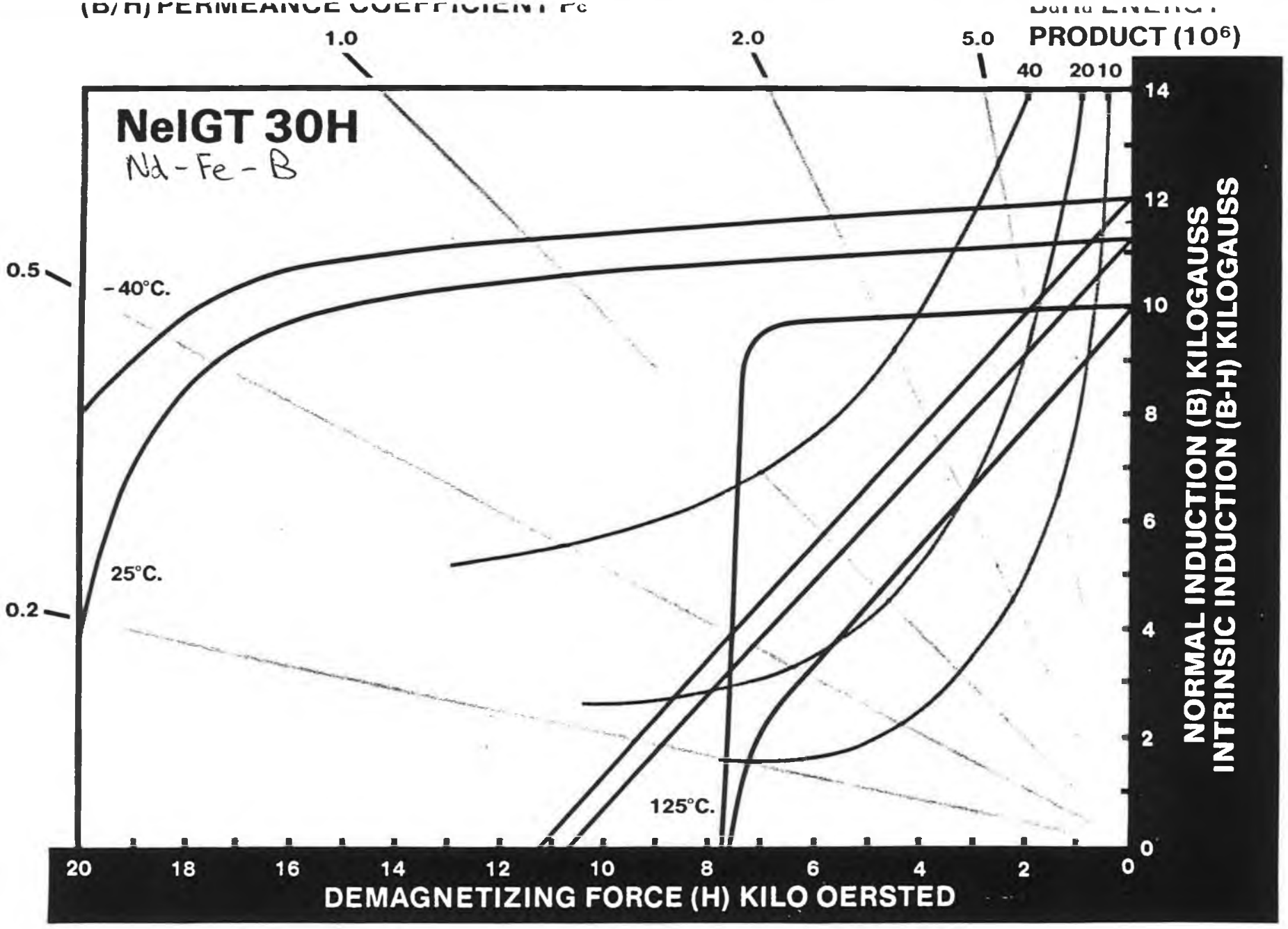

I G Technologies, Inc.
405 Elm Street
Valparaiso, Indiana 46383 U.S.A.

DEMAGNETIZATION CURVES

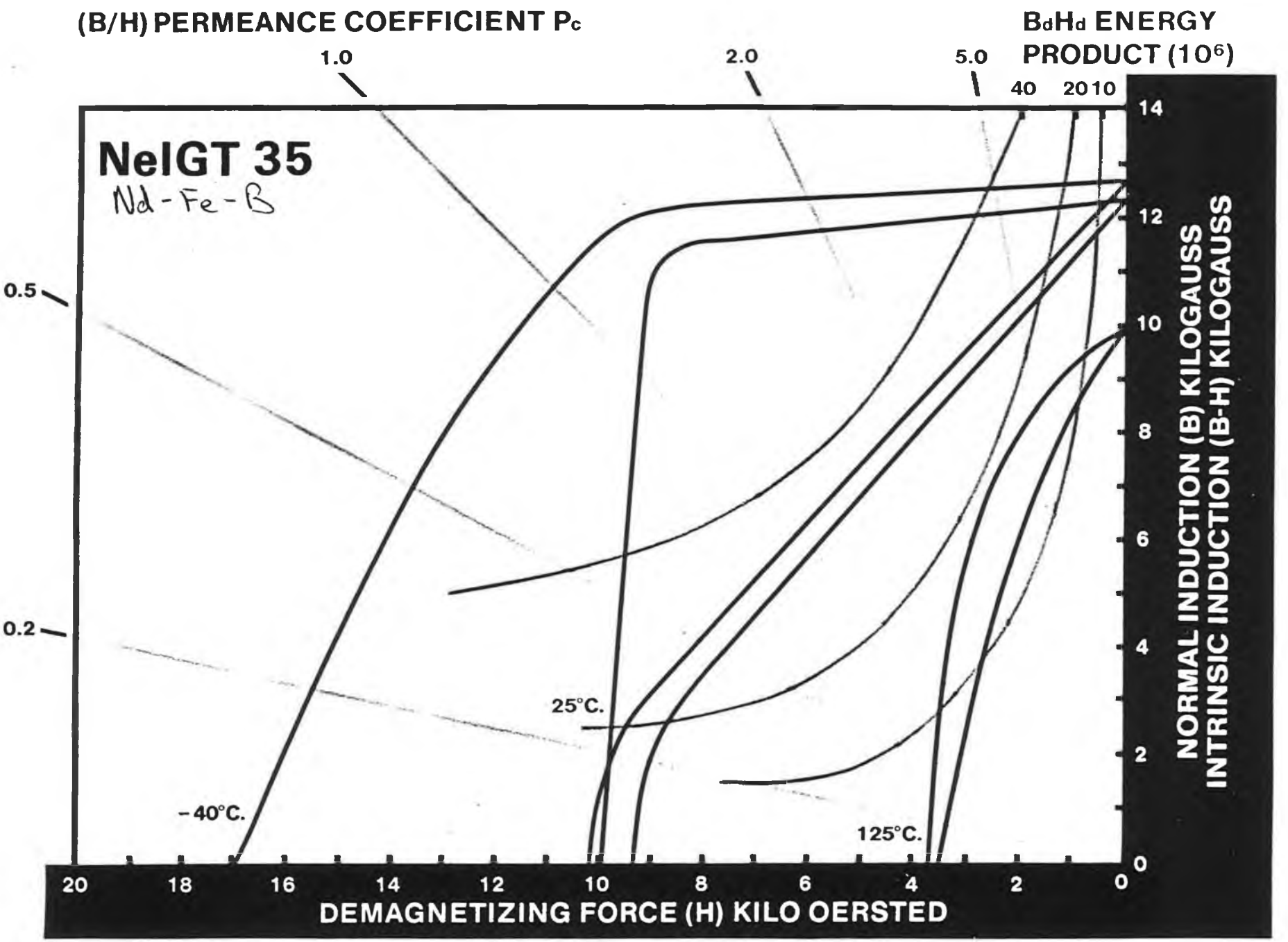

I G Technologies, Inc.

DEMAGNETIZATION CURVES

Crucible Magnetics

Demagnetization Curve and Energy Product Values

CRUMAX 282	10.8	10.1	17	28
CRUMAX 301	11.0	10.6	20	30
CRUMAX 315	11.5	10.9	14	31
CRUMAX 322	11.6	10.8	17	32
CRUMAX 355	12.3	11.3	14	35

A Division of Crucible Materials Corporation
101 Magnet Drive
Elizabethtown, Kentucky 42701
502/769-1333

Crucible Magnetics

Crumax® 282
Demagnetization Curve and Energy Product Values

COMPARISON DATA

	Br(kG)	Hc(kOe)	Hci(kOe)	BH max(mega-G-Oe)
CRUMAX 261	10.4	10.0	20	26
CRUMAX 282	10.8	10.1	17	28
CRUMAX 301	11.0	10.6	20	30
CRUMAX 315	11.5	10.9	14	31
CRUMAX 322	11.6	10.8	17	32
CRUMAX 355	12.3	11.3	14	35

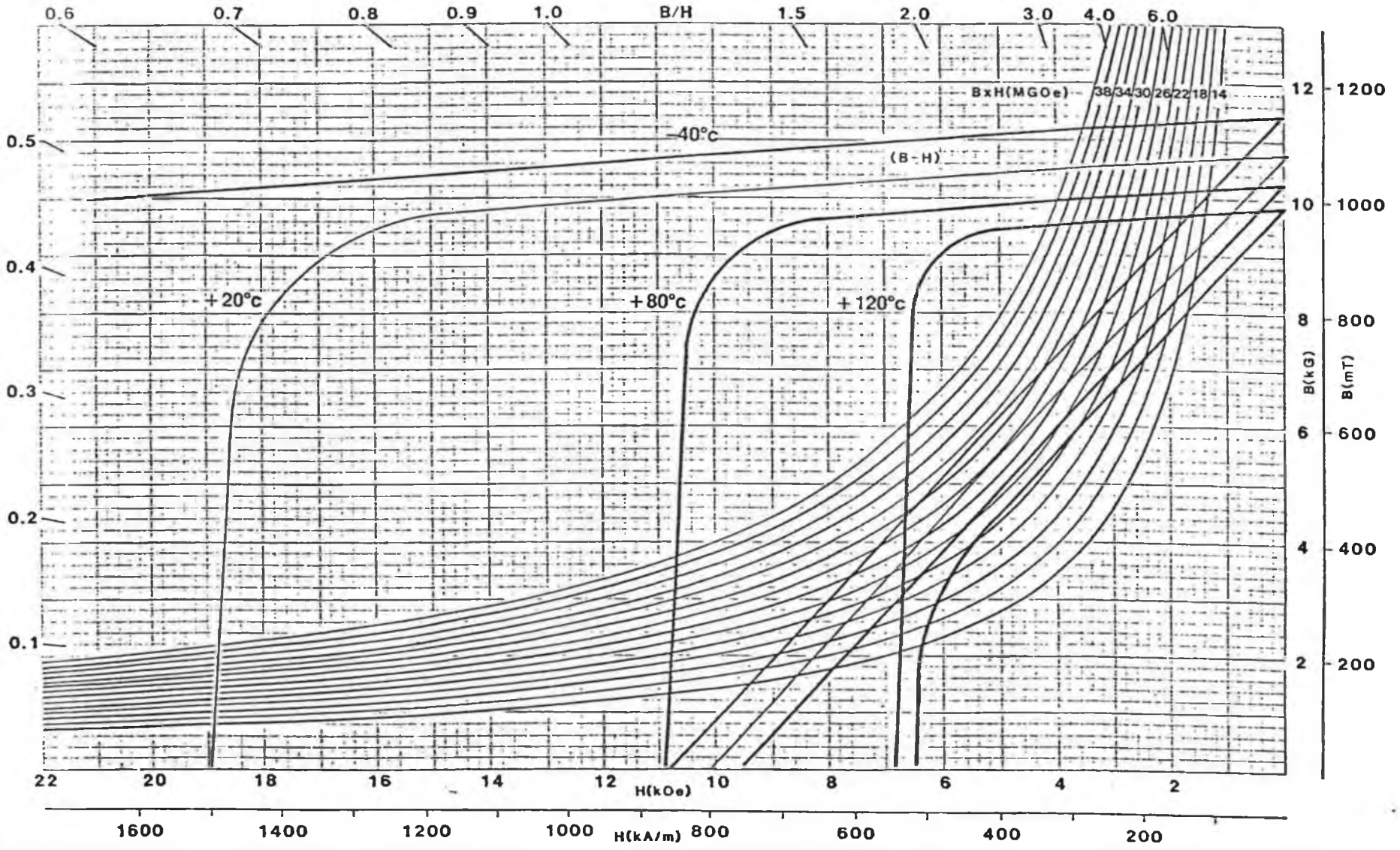

A Division of Crucible Materials Corpora
101 Magnet Drive
Elizabethtown, Kentucky 42701
502/769-1333

Crucible Magnetics

Crumax® 301

Demagnetization Curve and Energy Product Values

	Br(kG)	Hc(kOe)	Hci(kOe)	BH max(mega·G·Oe)
CRUMAX 261	10.4	10.0	20	26
CRUMAX 282	10.8	10.1	17	28
CRUMAX 301	11.0	10.6	20	30
CRUMAX 315	11.5	10.9	14	31
CRUMAX 322	11.6	10.8	17	32
CRUMAX 355	12.3	11.3	14	35

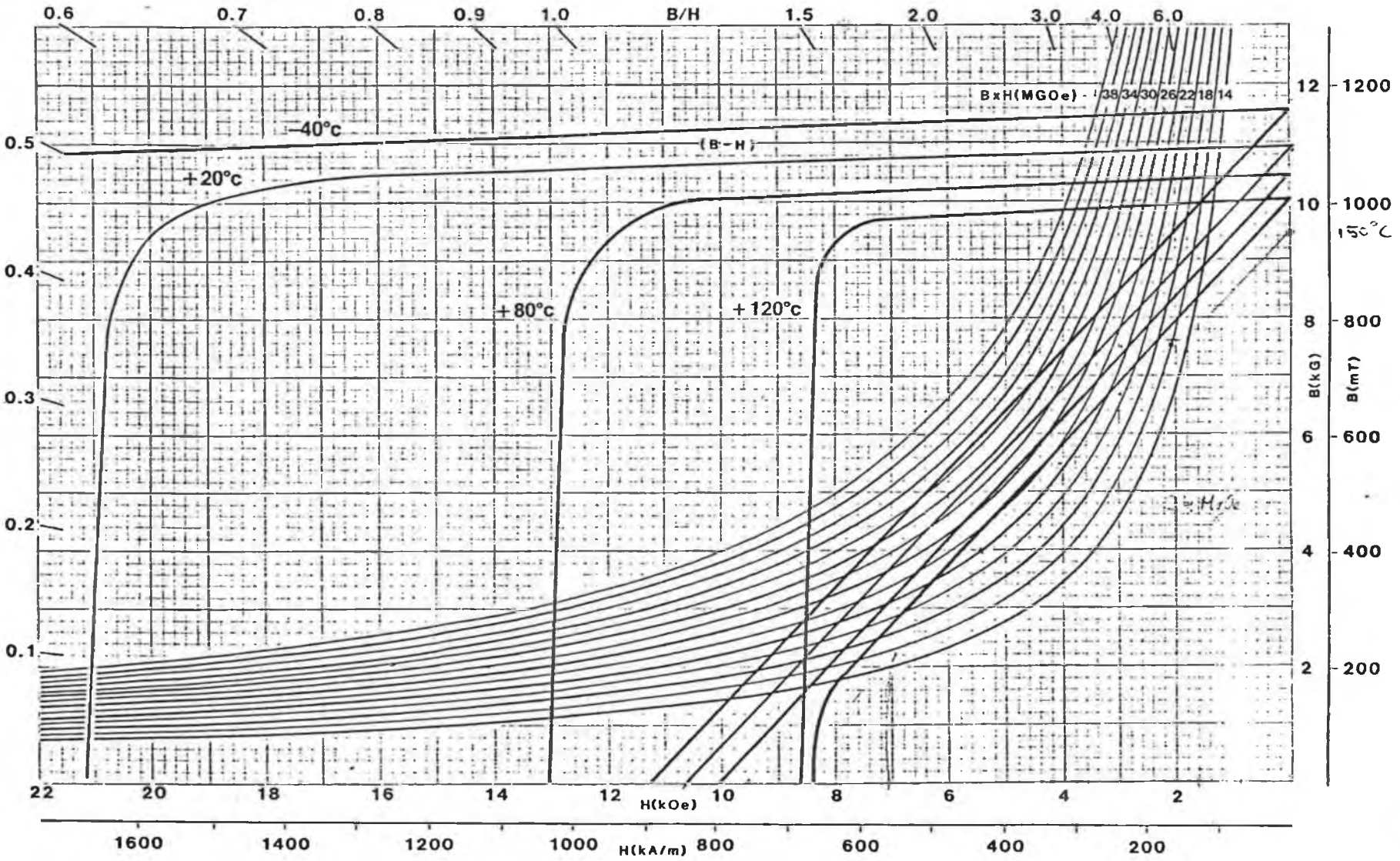

A Division of Crucible Materials Corporation
101 Magnet Drive
Elizabethtown, Kentucky 42701
502/769-1333

Crumax® 322

Demagnetization Curve and Energy Product Values

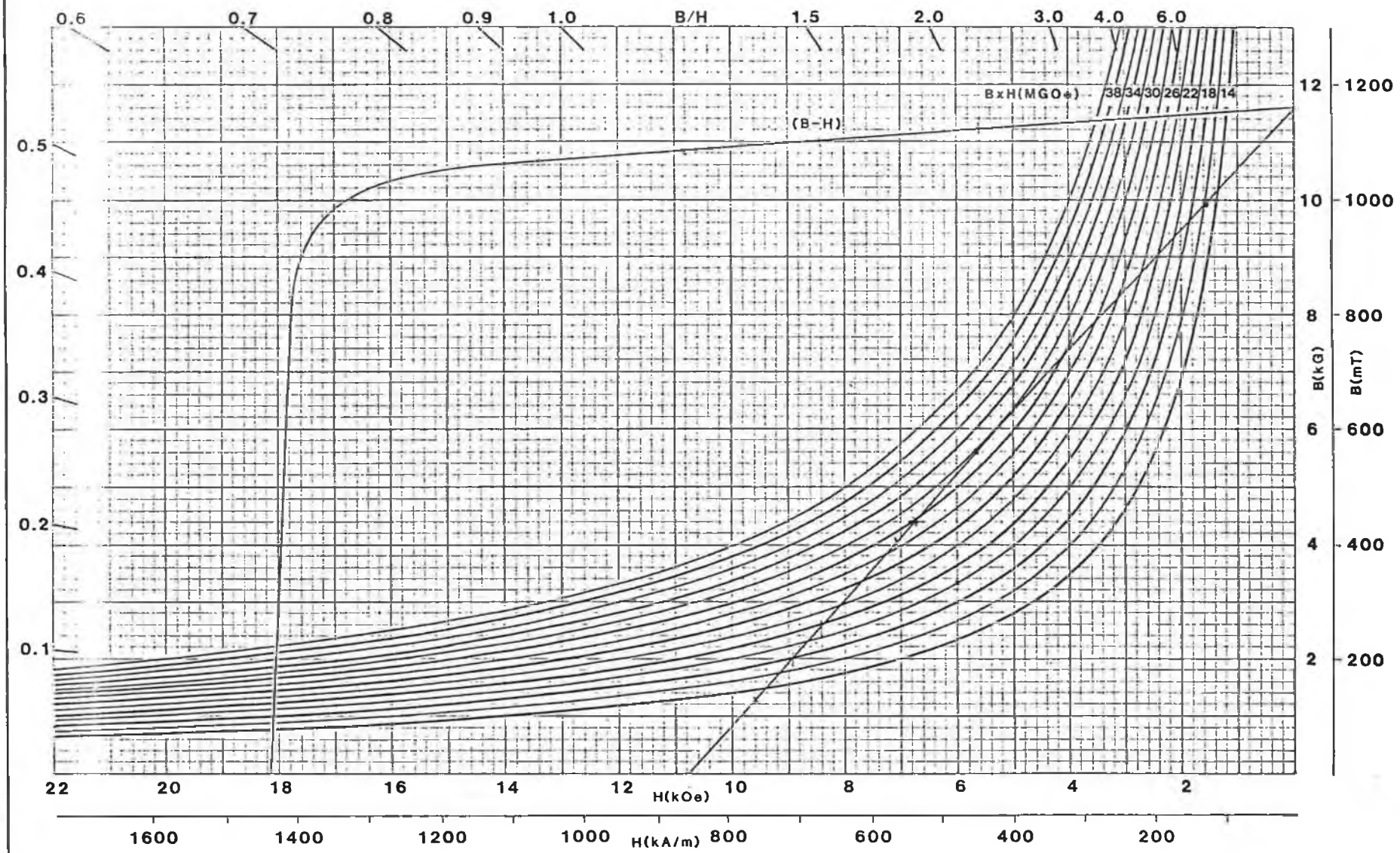

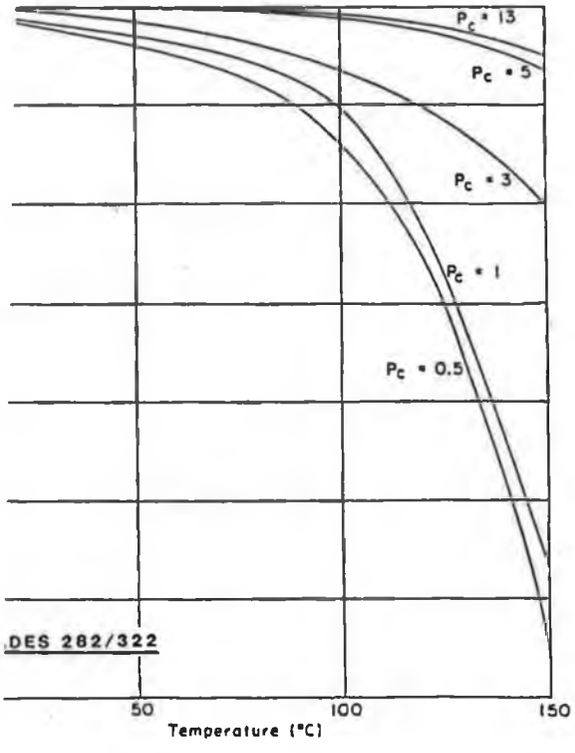

Irreversible Loss

FIGURE 2

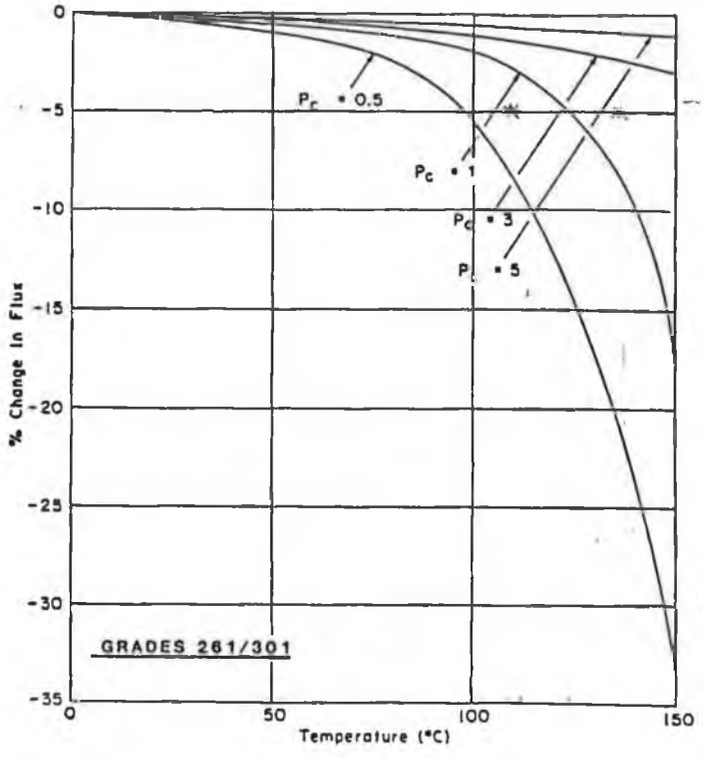

-135°C

Irreversible Loss

FIGURE 3

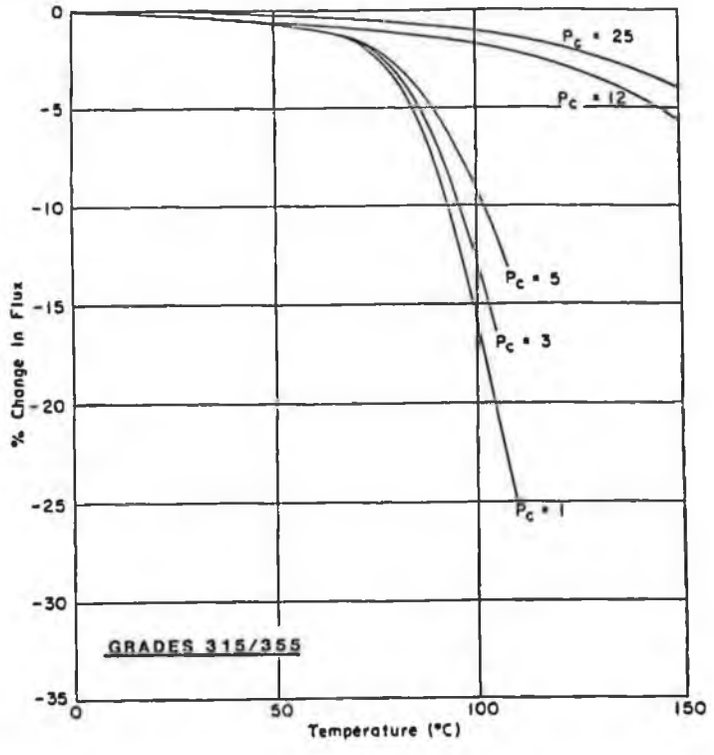

Irreversible Loss

FIGURE 4

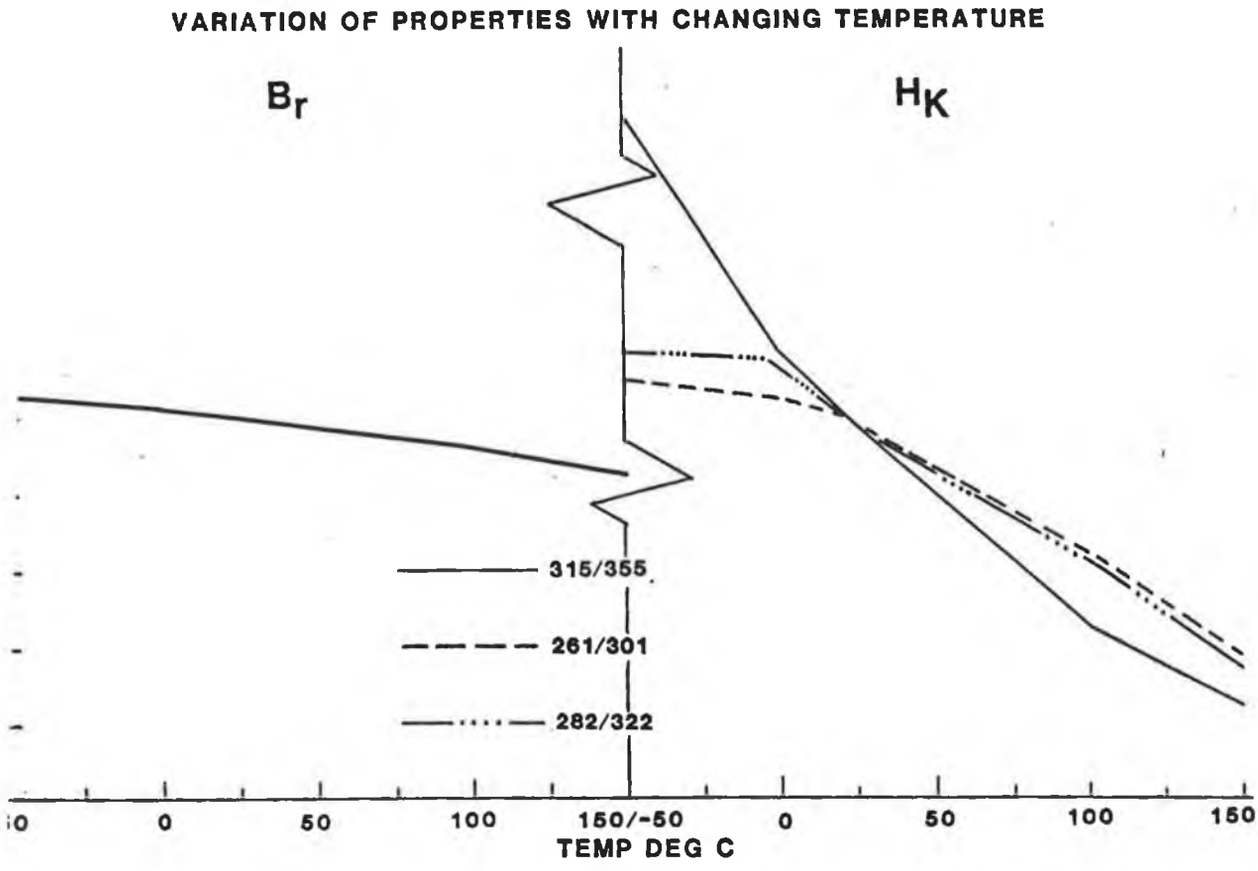

Figure 6

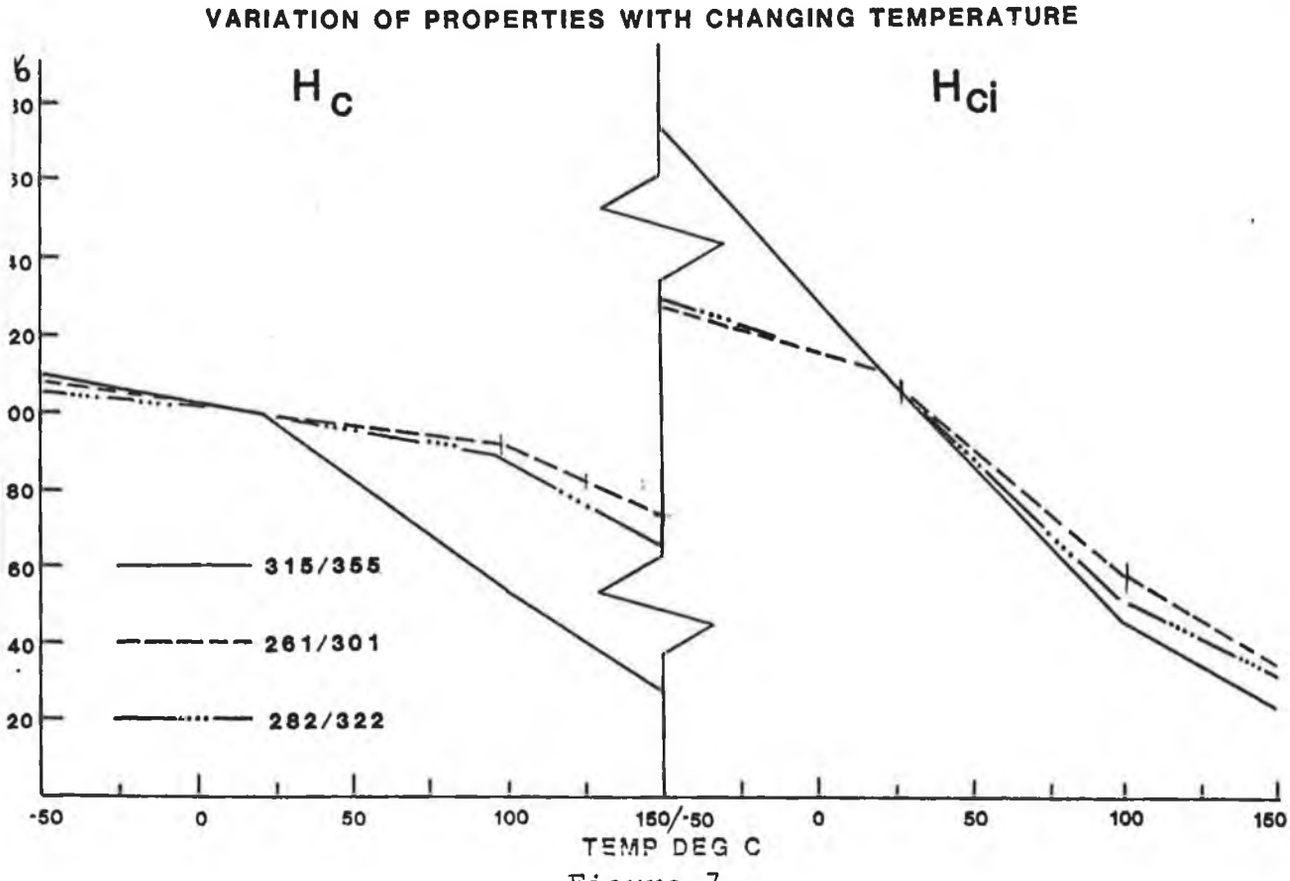

Figure 7

APPENDIX (G)

SAMPLE INPUT AND OUTPUT DATA SETS FOR THE MOTOR PROGRAM.

MOTOR INPUT PARAMETERS

BASIC MACHINE GEOMETRY (INCHES)

STATOR O.D.	3.550
STATOR I.D.	2.100
STATOR STACK LENGTH	2.025
LAMINATION THICKNESS	0.025
NUMBER OF SLOTS	39.00
DIAMETER TO SLOT BOTTOM	3.300
SLOT WIDTH @ TOOTH TIP	0.095
SLOT WIDTH @ TOOTH BOTTOM	0.185
SLOT DEPTH	0.561
DEPTH OF TOOTH TIP	0.010
SLOT OPENING	0.060
NUMBER OF POLES	12.00
DIAMETER OVER ROTOR MAGNETS	2.034
AXIAL LENGTH OF MAGNETS	2.000
CIRCUMFERENTIAL MAGNET WIDTH	0.365
MAGNET LENGTH @ CENTRE	0.147
ROTOR I.D.	0.000
ROTOR STACK LENGTH	2.060

WINDING DATA

TURNS PER COIL	13.00
AMERICAN WIRE GAUGE	19.00
COIL THROW	3.00
DISTRIBUTION FACTOR	0.9531
WINDING FACTOR	0.9462
COIL ENDTURN LENGTH	0.600
SLOT INSULATION THICKNESS	0.010
NO FULL SLOTS (INDUCT CALC)	23.00
NO HALF SLOTS (INDUCT CALC)	6.00

MAGNET CHARACTERISTICS

RESIDUAL INDUCTION (T)	1.0400
COERCIVITY (AT/M)	8.356E5
COERCIVITY @100 DEG C (AT/M)	7.321E5
REV TEMP COEFF INDUCTION	0.868E-3
REV TEMP COEFF COERCIVITY	0.943E-3
PERMANENT MAGNET DENSITY	7.4E3
ROTOR HEAT TRANSFER COEFF	0.700

MISCELLANEOUS INPUT

FLUX LEAKAGE FACTOR	1.10
ACTIVE TOOTH FACTOR	0.70
TERMINAL VOLTAGE	300.00
MAX WINDING TEMP (DEG C)	155.00
PEAK TEMP (DEG C)	100.00
AMBIENT TEMPERATURE (DEG C)	40.00
THERMAL RES COEFF (DEG C/W)	0.72
RATED CONTINOUS CURRENT	9.90

BRUSHLESS D.C. MOTOR DESIGN

BASIC INPUT DATA (METRIC)

STATOR O.D.	=	0.9017E-01	
STATOR I.D.	=	0.5334E-01	
STACK HEIGHT	=	0.5144E-01	
LAMINATION THICKNESS	=	0.6350E-03	
NO OF SLOTS	=	39.00	
DIAMETER TO SLOT BOTTOM	=	0.8382E-01	
SLOT WIDTH AT TOOTH TIP	=	0.2413E-02	
SLOT WIDTH AT TOOTH BOTTOM	=	0.4699E-02	
SLOT DEPTH	=	0.1425E-01	
TOOTH TIP DEPTH	=	0.2540E-03	
SLOT OPENING	=	0.1524E-02	
NO OF POLES	=	12.00	
DIAMETER OVER ROTOR	=	0.5166E-01	
MAGNET AXIAL LENGTH	=	0.5080E-01	
CIRCUMFERENTIAL MAGNET WIDTH	=	0.9271E-02	
MAX MAGNET LENGTH	=	0.3734E-02	
ROTOR I.D.	=	0.0000E+00	
ROTOR YOKE STACK	=	0.5232E-01	

WINDING INFORMATION

TURNS PER COIL	=	13.00	
WIRE GAUGE	=	19.00	
COIL THROW	=	3.000	
DISTRIBUTION FACTOR	=	0.9531	
WINDING FACTOR	=	0.9462	
COIL END TURN LENGTH	=	0.1524E-01	
SLOT INSULATION THICKNESS	=	0.2540E-03	
FULL SLOTS (INDUCTANCE)	=	23.00	
HALF SLOTS (INDUCTANCE)	=	6.000	

MAGNET CHARACTERISTICS

RESIDUAL INDUCTION (T)	=	1.040	
COERCIVITY (AT/M)	=	0.8356E+06	
COERCIVITY @100 DEG C (AT/M)	=	0.7321E+06	AN ESTIMATE
REV TEMP COEFF OF INDUCTION	=	0.8680E-03	
REV TEMP COEFF OF COERCIVITY	=	0.9430E-03	
PERMANENT MAGNET DENSITY	=	7400.	
ROTOR HEAT TRANSFER COEFF	=	0.7000	

MATERIAL = NE-FE-B (NEIGT 35H)

FLUX LEAKAGE FACTOR	=	1.100	
ACTIVE TOOTH FACTOR	=	0.7000	
RATED CURRENT CTNS (A)	=	9.900	

BASIC GEOMETRICAL OUTPUT DATA

MAGDIA	=	0.4516E-01
XSECRY	=	0.1181E-02
FSTACK	=	0.9500
XSECSY	=	0.1551E-03
TIPTIK	=	0.2043E-02
TOOTIK	=	0.2053E-02
AVGTIK	=	0.2048E-02
ATPP	=	0.3253E-03
RPOLE	=	0.6892
LGAP	=	0.8382E-03
AMAGPP	=	0.4812E-03
LGEFF	=	0.9531E-03
AMAG	=	0.4710E-03
LMAGAV	=	0.3524E-02
LSY	=	0.1139E-01
LRYPM	=	0.1929E-01
TOOVOL	=	0.5562E-04
CORVOL	=	0.4240E-04
LCON	=	0.8349E-01
CONPP	=	338.0
SLOTWA	=	0.4188E-04
ENDWA	=	0.2135E-03
WIRE GAUGE	=	19.00
WIRDIA	=	0.9794E-03
SLOTFF	=	59.55
RESLTL	=	1.498

MAX WINDING TEMP (DEG C)	=	155.0
PEAK TEMP (DEG C)	=	100.0

RUNNING MAGNETIC ROUTINE @ MAX WINDING TEMP

B RESIDUAL @MAX WTEMP	=	0.9646
H COERCIVITY @ MAX W TEMP	=	0.7698E+06
INTPHI	=	0.4130E-03

MAGNETIC DATA

PHIAVG (WEBERS)	=	0.3313E-03
STAPHI "	=	0.3312E-03
BGAP (TESLA)	=	0.7578
BTOOTH "	=	1.602
BSYOKE "	=	1.175
BRYOKE "	=	0.1698
SATURATION FACTOR	=	1.030

ALL FLUX DENSITIES MULTIPLIED BY KPHI

MOTOR PARAMETERS

FLUX DENSITY IN MAGNET (TESLA)	=	0.7735
COS(THETA)	=	0.8832
KTTY (Nm/A)	=	0.5504
KTTY (lb-in/A)	=	4.871
KMOTOR (Nm/WATT**0.5)	=	0.4497
VELOCITY AT 240 Hz	=	2400.
CORELOSS STATOR YOKE (2400RPM)	=	6.723
CORELOSS STATOR TEETH (2400RPM)	=	22.74

```
TOTAL CORELOSS @ 1000RPM (WATTS)     =   7.923
CORELOSS FACTOR @ MAX WINDING TEMP   =   7.923
TORQUE CONSTANT @ MAX WINDING TEMP   =  0.5504

  RUNNING MAGNETIC ROUTINE @ PEAK TEMP
  ------------------------------------
B RESIDUAL @ PEAK TEMP               =  0.9994
H COERCIVITY @ PEAK TEMP             =  0.8001E+06
INTPHI                               =  0.4278E-03

     MAGNETIC DATA
     -------------
  PHIAVG (WEBERS)      =  0.3428E-03
  STAPHI      "        =  0.3425E-03
  BGAP    (TESLA)      =  0.7842
  BTOOTH      "        =   1.657
  BSYOKE      "        =   1.216
  BRYOKE      "        =  0.1757
  SATURATION FACTOR    =   1.043
ALL FLUX DENSITIES MULTIPLIED BY KPHI

   MOTOR PARAMETERS
   ----------------
FLUX DENSITY IN MAGNET (TESLA)       =  0.7998
COS(THETA)                           =  0.8832
KTTY (Nm/A)                          =  0.5696
KTTY (lb-in/A)                       =   5.041
KMOTOR (Nm/WATT**0.5)                =  0.4653
VELOCITY AT 240 Hz                   =   2400.
CORELOSS STATOR YOKE (2400RPM)       =   7.466
CORELOSS STATOR TEETH (2400RPM)      =   25.25
TOTAL CORELOSS @ 1000RPM (WATTS)     =   8.800
CORELOSS FACTOR @ PEAK WINDING TEMP  =   8.800
TORQUE CONSTANT @PEAK WINDING TEMP   =  0.5696

  RUNNING MAGNETIC ROUTINE @ 25 DEG C
  -----------------------------------
INTPHI                               =  0.4452E-03

     MAGNETIC DATA
     -------------
  PHIAVG (WEBERS)      =  0.3556E-03
  STAPHI      "        =  0.3553E-03
  BGAP    (TESLA)      =  0.8134
  BTOOTH      "        =   1.719
  BSYOKE      "        =   1.261
  BRYOKE      "        =  0.1822
  SATURATION FACTOR    =   1.063
ALL FLUX DENSITIES MULTIPLIED BY KPHI

   MOTOR PARAMETERS
   ----------------
FLUX DENSITY IN MAGNET (TESLA)       =  0.8298
COS(THETA)                           =  0.8832
KTTY (Nm/A)                          =  0.5908
KTTY (lb-in/A)                       =   5.229
KMOTOR (Nm/WATT**0.5)                =  0.4827
VELOCITY AT 240 Hz                   =   2400.
CORELOSS STATOR YOKE (2400RPM)       =   8.349
CORELOSS STATOR TEETH (2400RPM)      =   28.24
```

CONTINUOUS OPERATING DATA

MAX CONTINUOUS WDG TEMP (DEG C)	=	155.0
AMBIENT TEMP (DEG C)	=	40.00
TERMINAL VOLTAGE	=	300.0
THERMAL RES COEFF (DEG C/WATT)	=	0.7200
MOTOR TEMP PEAK CURVE (DEG C)	=	100.0
CTNS CLOSS DAMP FAC (Nm/SQRTrpm)	=	0.2870E-02
MAX TEMP RISE (DEG C)	=	115.0
RES LTL @ MAX TEMP (OHMS)	=	2.249

SPEED(RPM)	TORQUE (Nm)	CURRENT	VSPARE	POWER (W)
0.0000000E+00	4.638494	8.427614	281.0478	0.0000000E+00
200.0000	4.585546	8.405158	269.0765	96.03968
400.0000	4.546050	8.363942	256.2386	190.4249
600.0000	4.503607	8.310266	242.7065	282.9706
800.0000	4.457498	8.246251	228.6825	373.4314
1000.000	4.407619	8.173034	214.3398	461.5658
1200.000	4.353973	8.091304	199.8091	547.1376
1400.000	4.296578	8.001498	185.1846	629.9128
1600.000	4.235441	7.903889	170.5346	709.6566
1800.000	4.170543	7.798630	155.9096	786.1307
2000.000	4.101845	7.685779	141.3485	859.0905
2200.000	4.029281	7.565320	126.8828	928.2817
2400.000	3.952759	7.437165	112.5390	993.4390
2600.000	3.872161	7.301157	98.34038	1054.281
2800.000	3.787334	7.157074	84.30875	1110.507
3000.000	3.698096	7.004623	70.46492	1161.794
3200.000	3.604222	6.843431	56.82965	1207.789
3400.000	3.505443	6.673039	43.42422	1248.106
3600.000	3.401438	6.492887	30.27115	1282.315
3800.000	3.291817	6.302292	17.39471	1309.932
4000.000	3.176112	6.100421	4.821777	1330.410
4200.000	3.053754	5.886254	-7.417450	1343.114